UNIVERSITY OF COPENHAGEN
FACULTY OF SCIENCE

PhD Thesis

Gonzalo Prieto-Lyon

The emergent properties of the first ionizers

Lyman-Alpha and ionizing photon production at the edge of reionization

Advisor: Charlotte Mason

Submitted: January 10, 2025

This thesis has been submitted to the PhD School of The Faculty of Science, University of Copenhagen

THE EMERGENT PROPERTIES OF THE FIRST IONIZERS:

Lyman-Alpha and ionizing photon production at the edge of Reionization

DISSERTATION SUBMITTED FOR THE DEGREE OF

PHILOSOPHIÆ DOCTOR

TO THE PHD SCHOOL OF THE FACULTY OF SCIENCE,
KØBENHAVNS UNIVERSITET

Gonzalo Prieto-Lyon

Assessment Committee:
Prof. Anne Verhamme
Prof. Hakim Atek
Prof. Johan Fynbo

Advised by:
Charlotte Mason

JANUARY 2025

ABSTRACT

The Epoch of Reionization was the last major phase change of the Universe. The newly formed galaxies emitted heavy ionizing radiation causing a shift from a neutral to an ionized intergalactic medium. Even though the community has reached some consensus on the endpoint of the Epoch of Reionization (EoR), the early stages and main contributing galaxies remain a mystery. One of the best tools to investigate the state of the EoR, is the Lyman-Alpha emission, its hydrogen resonant properties give it the advantage of being absorbed by neutral hydrogen, making it a great tracer for the state of the IGM. Nonetheless, if we want to use Lyman-Alpha to infer the timeline of reionization we first need to understand its emergent properties, that is the typical strength and profile of the line as it leaves the interstellar and circumgalactic mediums. The launch of JWST has given us a new opportunity to face these challenges, with its infrared capabilities we can now observe the rest-frame optical lines. Hα is particularly interesting allowing measurements of: The non-escaping ionizing photon production; the velocity shift of Lyman-Alpha due to resonant scattering; the fraction of Lyman-Alpha photons that escape into the IGM. In this thesis I present a study on galaxies at the end of the EoR ($z \sim 3-7$). These galaxies are not strongly affected by the neutral hydrogen of the IGM as those at higher redshift, making them useful for understanding the emergent properties of the Lyman-Alpha line profile and their ionizing photon production through Hα.

In the first project (Prieto-Lyon et al., 2023a), we present for the first time in history demographics study of the ionizing photon production of UV-faint galaxies. We study a sample of 370 galaxies (with 102 Lyman-Alpha galaxies) at $z \sim 3-7$, reaching as low as $M_{\rm UV} \sim -15.5$. With multiband photometry from JWST/NIRCam imaging we inferred Hα flux measurements and the non escaping ionizing fraction. We found that these analogs of the galaxies in the EoR tend to have a big diversity of ionizing photon production, with an intrinsic scatter of half an order of magnitude. We explore trends with other observables and find a preference

for strong ionizers to be UV-faint; young, dust-free galaxies; have assumed low metallicities; as well as having Lyman-Alpha emission. We conclude that the first ionizers, similar to our UV-faint galaxies, may have a rich distribution of ionizing photon production that needs to be considered when assessing the drivers of reionization.

In the second part (Prieto-Lyon et al., 2023b), we present new, never seen, Lyman-Alpha velocity offsets of UV-faint galaxies at $z \sim 3-6$, down to $\mathrm{M_{UV}} \sim -16$. Due to the degeneracy between the effect of neutral hydrogen from the nearby IGM and ISM/CGM being degenerate with each other, it is necessary to observe the Lyman-Alpha profile at the end of EoR to have a baseline idea of the typical emergent emission. We find through VLT/MUSE and JWST/NIRSpec observations that UV-faint galaxies typically have a median Lyman-Alpha velocity offset lower than their brighter counterparts outside EoR, but also lower than most galaxies found deep in this epoch. We find that the typical UV-faint galaxy needs at least 1pMpc of ionized hydrogen in the line-of-sight to transmit 30% of its original Lyman-Alpha emission, from which follows that detection of low velocity offsets at EoR suggest the presence of large ionized bubbles.

In the third and final part (Prieto-Lyon in progress), we obtained restframe UV spectra of 236 galaxies, including 65 Lyman-Alpha detections. We added ancilliary data from JWST / FRESCO, which allowed us to obtain systemic redshifts and H_α fluxes for 51 sources. We present new results on Lyman-Alpha shape and strength, including the first high-resolution results of the Lyman-Alpha FWHM distribution at z$\sim$ $5-6$, new Lyman-Alpha velocity offset results, and a new empirical model for Lyman-Alpha equivalent width and escape fraction. Our results show that Lyman-Alpha is narrower and more offset than what can be inferred from lower redshift samples, leading to a boosted Lyman-Alpha transmission of up to 5 times. This suggests that the IGM might be more neutral at z>6 than previously predicted. Our line strength models $45-62\%$ of $\mathrm{M_{UV}} = -19.5$ galaxies have a Lyman-Alpha equivalent width > 25 Å and escape fraction > 0.2, respectively.

Past z$\sim$8, Lyman-Alpha will be our best tool to constraint the timeline of reionization, this and similar works that measure emergent Lyman-Alpha properties will be key to break the

ISM/CGM and IGM degeneracy. The growing samples of Lyman-Alpha deep into the EoR will need of such models to be able to accurately infer the neutral gas fraction at the earlier stages of the EoR.

ABSTRACT PÅ DANSK

Epoken for reionisering var den sidste store faseændring i Universet. De nydannede galakser udsendte kraftig ioniserende stråling, hvilket forårsagede et skift fra et neutralt til et ioniseret intergalaktisk medium. Selvom forskersamfundet er enige om slutpunktet for reioniseringsepoken (EoR), forbliver de tidlige stadier og de vigtigste bidragende galakser et mysterium. Et af de bedste værktøjer til at undersøge EoRs tilstand er Lyman-Alpha-emission. Dens resonante egenskaber gør den i stand til at blive absorberet af neutralt brint, hvilket gør den til en fremragende indikator for intergalaktisk mediums tilstand. Hvis vi ønsker at bruge Lyman-Alpha til at udlede reioniseringens tidslinje, skal vi dog først forstå dens fremkommende egenskaber, herunder dens styrke og profil, når den forlader det interstellare og circumgalaktiske medium. Lanceringen af JWST har givet os en ny mulighed for at tage disse udfordringer op. Med sine infrarøde kapabiliteter kan vi nu observere restframe-optiske linjer. Hα er særligt interessant, da den muliggør målinger af: produktionen af ikke-undslippende ioniserende fotoner; Lyman-Alphas hastighedsforskydning forårsaget af resonant spredning; og fraktionen af Lyman-Alpha-fotoner, der undslipper til det intergalaktiske medium. I denne afhandling præsenterer jeg en undersøgelse af galakser i slutningen af EoR ($z \sim$ 3-7). Disse galakser påvirkes ikke stærkt af det neutrale brint i IGM, som dem ved højere rødforskydning, hvilket gør dem nyttige til at forstå de iboende egenskaber ved Lyman-Alpha-linjens profil. De ligger også i det rødforskydningsinterval, hvor vi kan bruge JWST til at detektere deres ioniserende fotonproduktion gennem Hα.

I det første projekt præsenterer vi for første gang en demografisk undersøgelse af ioniserende fotonproduktion i UV-svage galakser. Vi studerer et udvalg på 370 galakser (herunder 102 Lyman-Alpha-galakser) ved $z \sim$ 3-7 og når så langt ned som $M_{UV} \sim$ -15,5. Med multibånds-fotometri fra JWST/NIRCam-billeder udledte vi Hα-fluxmålinger og den ikke-undslippende ioniseringsfraktion. Vi fandt, at disse analoger til galakser i EoR har stor diversitet i ioniserende fotonproduktion, med en indre spredning på en halv størrelsesorden. Vi undersøger tendenser med andre observabler og finder en præference for, at stærke ionisatorer er UV-svage; unge, støvfrie galakser; med lav antaget metalindhold; og med Lyman-Alpha-emission. Vi konkluderer, at de første ionisatorer, som minder om vores UV-svage galakser, kan have en rig fordeling af ioniserende fotonproduktion, som skal tages i betragtning ved vurderingen af reioniseringens drivkræfter.

I den anden del præsenterer vi nye, hidtil usete Lyman-Alpha-hastighedsforskydninger af UV-svage galakser ved $z \sim$ 3-6, ned til $M_{\text{UV}} \sim$ -16. På grund af degenereringen mellem effekten af neutralt brint i det nærliggende IGM og ISM/CGM er det nødvendigt at observere Lyman-Alpha-profilen i slutningen af EoR for at få en baseline for typisk fremkommende emission. Vi finder gennem VLT/MUSE- og JWST/NIRSpec-observationer, at UV-svage galakser typisk har en median Lyman-Alpha-hastighedsforskydning, der er lavere end deres lysere modparter uden for EoR, men også lavere end de fleste galakser, der findes dybt i denne epoke. Vi konkluderer, at typiske UV-svage galakser kræver mindst 1pMpc ioniseret brint i sigtelinjen for at transmittere 30% af deres oprindelige Lyman-Alpha-emission. Dette antyder, at detektion af lave hastighedsforskydninger i EoR indikerer tilstedeværelsen af store ioniserede bobler.

I den tredje og sidste del opnåede vi restframe UV-spektre af 236 galakser, herunder 65 Lyman-Alpha-detektioner. Vi tilføjede supplerende data fra JWST/FRESCO, hvilket gjorde det muligt for os at opnå systemiske rødforskydninger og Hα-fluxmålinger for 51 kilder. Vi præsenterer nye resultater om Lyman-Alpha-form og -styrke, herunder de første højopløsningsresultater for fordelingen af Lyman-Alpha FWHM ved z$\sim$5-6, nye resultater om Lyman-Alpha-hastighedsforskydninger og en ny empirisk model for Lyman-Alpha-ekvivalent bredde og escape-fraktion. Vores resultater viser, at Lyman-Alpha er smallere og mere forskudt end hvad der kan udledes fra lavere rødforskydningsprøver, hvilket fører til en forstærket Lyman-Alpha-transmission på op til 10 gange. Dette antyder, at IGM kan være mere neutral ved z>6, end tidligere forudsagt. Vores linjestyrkemodeller indikerer, at 45-65% af galakser med MUV $= -19,5$ har en Lyman-Alpha-ekvivalent bredde > 25 og en escape-fraktion >0,2.

Efter z$\sim$8 vil Lyman-Alpha være vores bedste værktøj til at begrænse reioniseringens tidslinje. Dette og lignende arbejder, der måler fremkommende Lyman-Alpha-egenskaber, vil være nøglen til at bryde ISM/CGM- og IGM-degenereringen. De voksende prøver af Lyman-Alpha dybt i EoR vil kræve sådanne modeller for præcist at kunne udlede brintens neutralitetsgrad i de tidligste stadier af EoR.

ACKNOWLEDGMENTS

I have met many important people in this long journey, and so I wanted to write this short letter to everyone that helped in my adventure. I would like to start by thanking the members of the committee Anne Verhamme, Hakim Atek and Johan Fynbo for taking the time to read this thesis and joining me on the day of my defense.

First I want to thank Charlotte for being a great supervisor, it has been great working with you on all these projects, you taught me a lot during the past 3 years and I will always cherish these memories. I always knew that no matter how lost I got in a project, I could rely on you to find my way back into the right track. It makes me happy to know that whoever you have as a student in the future, will be able to find such a great teacher and role model in you as I did. Thank you to all the people that we've had on the group Anne, Kimi, Koki, Ting-Yi and Viola for always being open to answer my questions, and bring me inspiration with all your amazing work. And an extra thanks to Victoria for receiving me with open arms when I first arrived at Copenhagen. Many thanks to Pascal and Gabe for all the help with JWST reduction wizardry.

A big thanks to the DAWN group, everyone has been extremely welcoming and I could never have wished for a better work environment. The opportunity of traveling from Chile to work here has been life changing in many aspects, and I could not be more happy that I got to work at the leading-edge of astronomy. Thanks to all the PhD students for being such good company. In no particular order, Thank you John for your awesome stories and for your great drinks. Thank you Rashmi for hearing me rant about my project while I kept interrupting yours. To Iris than you for being my Geneva trip advisor and for the time at DTU. Thank you to Natalie and Kate for the great company and introducing me to so many people. Thank you to Conor and Kimi for always being so funny and cheering me up. And thanks to the Astronomy on Tap team: Marko, Reggie, Marie and Aswyn we did some great events together.

Finally I wanted to thank my family and friends. It has been hard being so far away from home and I miss all of you. Gracias papá por creer en mi y siempre motivarme a seguir mis sueños; y a ti mamá por tanto cariño y hacer mi estadia en Europa tan entretenida. Thank you to my best friend Sebastian for all the great time we have shared in Copenhagen and for many more to come. Thank you Emil for all the bread, nice food and for stopping me from starving while I worked. Thank you to all my friends from the art and DnD community for inspiring me so much.

To everyone, my biggest thanks! These have been the best 3 years of my life.

CONTENTS

LISTING OF FIGURES

1

INTRODUCTION

The Epoch of Reionization (EoR) was the last great phase transition of the Universe. As the Universe expanded and the baryonic matter cooled downed, the first galaxies were formed. These new structures and the extreme ionizing radiation emitted by their newborn stars lead to the majority of the neutral hydrogen in the intergalactic medium (IGM) to completely ionize. The evolution of the neutral gas fraction (xHI) across cosmic time, named the reionization timeline, and brings us to our first key question: When did reionization occur?

The large amount of neutral hydrogen present in the early Universe produces a very weak HI 21cm signal, which at the moment has not been detected with state of the art radio telescopes (Greig et al., 2021; HERA Collaboration et al., 2023). We may then shift our search from direct detection of the IGM, to the effects of the IGM on the first galaxies and quasars. The intergalactic neutral hydrogen in close proximity to a galaxy will absorb photons with wavelengths below Lyman Alpha (Lyα). As the density of HI increases, the extreme density of absorption lines of the hydrogen transitions will lead to a *Gunn-Peterson trough*, in its spectra (Gunn & Peterson, 1965). Depending on the strength of this absorption damping wing, redder and redder wavelengths will be absorbed as the neutral hydrogen fraction of the Universe increases at earlier epochs (Laursen et al., 2011). Different methods take advantage of these galactic features, and have independently inferred the later stages of the reionization timeline. Examples of such are: Quasar Lyman Alpha forest (e.g. Becker et al., 2015; Yang et al., 2020; Bosman et al., 2022), quasar damping wings (e.g. Davies et al., 2018; Wang et al., 2020). These works have shown that reionization is near its conclusion at $z \sim 5.5$. But as new research moves into the earlier stages of the EoR, the number of quasars becomes increasingly rare past $z > 7$ (Euclid Collaboration et al., 2019).

The scarcity of quasars in the early Universe increases the need to use observations of the first galaxies to infer the timeline of reionization. This has been done by multiple groups through: Lyα luminosity functions (e.g. Morales et al., 2021), and Lyα equivalent width (EW) distributions in Lyman break galaxies (LBG) (e.g. Mason et al., 2018a; Jung et al., 2020; Whitler et al., 2020). As mentioned in the previous paragraph, as the damping wing of the

IGM gets stronger, it will start scattering wavelengths redwards of Lyα . This reduction in the relative strength of Lyα to the UV continuum, named equivalent width (EW$_{\mathrm{Ly}\alpha}$), then can be used to infer *xHI*. But this is not a simple problem since Lyα suffers from resonant scattering: As young stellar populations emit ionizing radiation and strip the surrounding HI of their electrons, these will later recombine around the edges of the strömgren sphere. One of the most common transitions that atoms take when they fall back to their gound-state is from n= $2 \rightarrow 1$, which emits a Lyα photon. Resonant scattering occurs as Lyα will be absorbed again by neighboring hydrogen, and re-emitted and so on until it shifts enough out of resonance to escape the HI region (Dijkstra, 2014). Depending on how strong the resonant scattering is, Lyα will emerge from the galaxy with a differently shaped profile, that may facilitate its transmission through the IGM. Therefore, we need to improve our understanding of the emergent properties of Lyα prior to considering the impact of the neutral hydrogen in the IGM.

In this work we focus on studying the properties of Lyman Alpha emission as it emerges from galaxies, focusing on: Lyman-Alpha equivalent width (EW$_{\mathrm{Ly}\alpha}$), Lyman-Alpha escape fraction ($f_{\mathrm{esc}}^{\mathrm{Ly}\alpha}$) and the Lyman-Alpha velocity offset ($\Delta v_{\mathrm{Ly}\alpha}$). For this purpose we observed galaxies that are near the end of the EoR (z$\sim 5-6.5$)(e.g. Fan et al., 2006; Gaikwad et al., 2023; Qin et al., 2021; Bosman et al., 2022) so that their Lyα will not be strongly absorbed by the HI at the EoR. The redshift range also promises that they will have physical properties as similar as possible to galaxies at z $\sim 7-10$.

A second key question about the EoR is: Which galaxies drove the reionization process? There currently are two disputed scenarios: Was it a few UV-bright galaxies or numerous UV-faint galaxies? The answer to which one dominates is highly degenerate without further studying the *xHI* at the early stages of the EoR. At the same time, studying the drivers of reionization is complicated since Lyman Continuum (LyC) is absorbed by the smallest traces of neutral hydrogen in the ionized Universe. Nonetheless, thanks to the new Near-Infrared capabilities of the James Webb Telescope, we have been able for the first time to observe the Hα emission of galaxies up to redshift 7 in a large number of galaxies. This gives us a partial window into the production rate of ionizing photons (ξ_{ion}) through the ionizing photons that do not escape to the IGM, but are reprocessed into Hα .

For my thesis I have used multi-wavelength observations from ground and space telescopes of high redshift galaxies with a focus on Lyα emission. I have made measurements of the emergent properties of high-redshift galaxies through analogs outside of the EoR, including $\xi_{\rm ion}$, $\Delta v_{\rm Ly\alpha}$, EW$_{\rm Ly\alpha}$ and $f_{\rm esc}^{\rm Ly\alpha}$. I have used the latter two to create empirical Bayesian models based on easily observable UV properties, with the goal of having better constrained models that can be used next to large datasets of future JWST z$>$ 9 Lyα observations to infer the timeline of reionization at earlier epochs, hopefully answering the question of the evolution of the neutral hydrogen fraction and the drivers of reionization. In the following sections I will briefly introduce the importance of these measurements as tools to understand the EoR.

1.1 A Great Change in the IGM: First ionizers and the morphology of the EoR

Legacy data and new JWST surveys of the early Universe (Eisenstein et al., 2023a; Treu et al., 2022; Oesch et al., 2023; Bezanson et al., 2022, e.g.) have shown a great variety of ionizing sources, from rare massively bright sources such as GNz-11 (Oesch et al., 2016; Bunker et al., 2023) to numerous galaxies at the faint-end of the UV luminosity functions (Prieto-Lyon et al., 2023a,b; Simmonds et al., 2024a,b). This leads to the question: Which sources dominated reionization? Depending on the answer, this will lead to very different morphologies (Lu et al., 2024) and reionization timelines (Naidu et al., 2020; Ishigaki et al., 2018; Finkelstein et al., 2019) of the early IGM.

This problem is non-trivial since the scenarios are degenerate as the EoR reaches its end (z$\sim 5.5-7$). The effect of numerous low mass galaxies with low ionizing emissivity (i.e. 5% ionizing photon escape fraction,$f_{\rm esc}$), will be similar to that of a few massive galaxies with high emissivity (e.g. Greig & Mesinger, 2017; Finkelstein et al., 2019; Naidu et al., 2020; Lu et al., 2024). Understanding the ionizing photon production and the escape fraction of these photons is crucial. Nonetheless, as of now detecting the Lyman Continuum directly has proven to be impossible past z$>$ 4 (Vanzella et al., 2018a) due to the IGM absorption, but a substantial part of the ionizing photons never escape the galaxies, exciting the hydrogen in the ISM and producing Hα (Osterbrock & Ferland, 2006).

Before the first JWST data release, observations of Hα at high-redshift had only been possible for non-stacked data of UV-bright galaxies ($M_{UV} < -20$) (Bouwens et al., 2016a; Harikane et al., 2018; Lam et al., 2019a; Maseda et al., 2020). In Prieto-Lyon et al. (2023a) (Chapter 2) we were able for the first time to measure Hα in individual UV-faint galaxies. Through the power of JWST/NIRCam, we revealed a large distribution of non-escaping $\xi_{\rm ion}$ which must be considered when assessing the primary drivers of reionization.

Depending on the primary drivers of reionization, xHI evolution will behave differently. Currently the community is evaluating (Ishigaki et al., 2018; Finkelstein et al., 2019; Naidu et al., 2020; Nakane et al., 2024, e.g.) between a rapid-late scenario: Where massive galaxies that take time to assemble dominate the reionization process; and a gradual-early scenario: Where low mass galaxies that are predominant since the earliest epochs, slowly ionize the IGM. At the same time, the morphology of the ionized bubbles formed will also change depending on the scenario (e.g. Hutter et al., 2023; Lu et al., 2024). Reionization dominated by low mass galaxies will start very early with numerous small ionized bubbles (Finkelstein et al., 2019), while in the rapid-late scenario we won't see any early significant ionized bubbles until enough mass has assembled into galaxies, at which point ($z \sim 7-8$) bubbles with a greater volume start to form, completely ionizing the medium in ~ 400 Myr(Naidu et al., 2020). But, separating both scenarios can be done by understanding ionized bubble sizes and the neutral gas fraction at given cosmic times.

A crucial problem is that both scenarios are not very different as reionization approaches its end, but the degeneracy fades as redshift increases and the scenarios become substantially different. Some of the most accurate measurements of reionization history are based on Lyman Forest of luminous sources such as quasars (e.g., Fan et al., 2006; Eilers et al., 2019; Bosman et al., 2022), but these are expected to be increasingly rare past $z > 7$ even with the upcoming Euclid data (Euclid Collaboration et al., 2019) which might not be enough to give a universal view of reionization. One method that we expect to work past this redshift is the use of

Lyman Alpha emission, with current observations finding Lyα up to $z = 13$ (Witstok et al., 2024b). The observability of Lyα highly depends on the neutral state of the Universe and the size of the ionizing bubbles present, with it being far more likely to be observed in large ionized regions with lines of sight devoid of neutral hydrogen. Lyα has been used numerous times as a tool to infer the state of reionization (e.g. Mason et al., 2018a; Jung et al., 2020; Whitler et al., 2020), but before the launch of JWST, we have also been limited to probing the late stages of reionization. As of now, the community has been pushing the observations of Lyα to higher redshifts, and we expect future large scale surveys to provide enough Lyα detections and non detections for inferring xHI in the early stages of reionization.

1.2 Lyman Alpha, a lighthouse in the early Universe

The ionizing radiation emitted by young stars in the first galaxies was not the only byproduct of star formation. Type O and B stars will ionize and excite the neutral hydrogen in the surrounding star forming regions, which will cascade in various emission lines, with one of the most luminous and important for the EoR being Lyα . The resonant nature of Lyα , leads to it being absorbed by neutral hydrogen in the IGM (Laursen et al., 2011). This relation between Lyα and the neutral IGM, can also be observed as the fraction of galaxies detected with strong Lyα emission (EW$>$ 25 Å) drop considerably once we set into the EoR ($z > 6$), implying an increasing fraction of neutral gas in the IGM (e.g. Stark et al., 2010; Pentericci et al., 2014; De Barros et al., 2017; Fuller et al., 2020; Tang et al., 2024a). But as Lyman Alpha interacts with the neutral gas in the IGM, it also interacts with the gas in the ISM and CGM. Making this a complex problem, where we need to understand the emergence of Lyα from the galaxies to learn how much it is scattered by the IGM's damping wing.

The resonant nature of Lyα leads to it being absorbed and re-emitted numerous time before it escapes HI regions. This will dictate its line profile shape and wavelength. Then, depending on how Lyα emerges from a galaxy, it will facilitate or difficult its transmission through the neutral IGM. This leaves important open questions to answer: What is the typical velocity offset ($\Delta v_{\mathrm{Ly}\alpha}$) at which Lyα escapes from these galaxies? How strong is the emission that emerges from the galaxy at the EoR ($\mathrm{EW}_{\mathrm{Ly}\alpha}$)? What are the typical Lyα escape fractions ($f_{\mathrm{esc}}^{\mathrm{Ly}\alpha}$)? And how broad is the Lyα emission before the damping wing eats at its emission? Among others.

One of the most interesting and important properties of Lyα when talking about its transmission through the IGM, is its velocity offset ($\Delta v_{\mathrm{Ly}\alpha}$). The shift of Lyα from resonance, due to multiple scattering events, will lead to an easier transmission of the line through the damping wing of the IGM. Models have shown that an increase in the neutral hydrogen column density in a galaxy will lead to a profile with a higher offset (Verhamme et al., 2015), with the second most important factor being the outflow velocity of the gas, we expect overall for massive galaxies to have a larger hydrogen column density due to their sizes.

In Prieto-Lyon et al. (2023b) (Chapter 3), we were able for the first time to measure $\Delta v_{\mathrm{Ly}\alpha}$ in UV-faint galaxies at z>3 up to $\mathrm{M}_{\mathrm{UV}} \sim -15.5$. Our results and other similar observations (e.g. Tang et al., 2024a) show UV-faint galaxies tend to have lower velocity offsets than UV-bright galaxies, with M_{UV} being correlated to both galaxy size and mass (Shibuya et al., 2015). From this we can conclude that overall UV-bright galaxies will have an easier time transmitting their Lyα emission in smaller bubbles due to its higher offset from the systemic wavelength, while UV-faint galaxies usually suffer a stronger absorption through the damping wing. Therefore the detection of Lyα from a UV-faint galaxy deep into the EoR is a strong indication of the presence of a large ionized bubble ($\gtrsim$ 1pMpc).

The strength of Lyα is a key factor for its observability after transmission through the IGM. Nonetheless, Lyα at the EoR remains rare. The presence of ionized bubbles leads to a bias towards observing Lyα in over dense regions (Leonova et al., 2022; Tacchella et al., 2023), specially in UV-bright galaxies that have an easier time transmitting Lyα through higher $\Delta v_{\mathrm{Ly}\alpha}$. Then again, we can shift our search towards galaxies at the edge of the EoR, where we can have a clearer view of the emergent $\mathrm{EW}_{\mathrm{Ly}\alpha}$ distribution, while it is only minimally affected by HI in the IGM. Several works have created empirical model of such sources by marginalizing over the UV properties of high-redshift sources (Tang et al., 2024a) or building a linear model from lower-redshift samples (Oyarzún et al., 2017). Both M_{UV} and β are ideal parameters to perform such models, they both are correlated to the production and escape of Lyα through the stellar population and dust attenuation; and are easily observable with limited photometric data at z>7.

In Prieto-Lyon et al. (in prep) (Chapter 4), we present in our main result a new high-resolution dataset of Lyα detections and non-detections at a median z~ 5.6. We report the first Lyα FWHM distribution of galaxies near the end of the EoR, and new velocity offset results. This implies that Lyα might be boosted ~ 5 times more than expected by models based on z~ 2 observations. We also use this dataset and Bayesian inference to build an empirical model of $\mathrm{EW}_{\mathrm{Ly}\alpha}$ and $f_{\mathrm{esc}}^{\mathrm{Ly}\alpha}$. Each model is built from their correlation with M_{UV} , and we find both: $\mathrm{EW}_{\mathrm{Ly}\alpha}$ and $f_{\mathrm{esc}}^{\mathrm{Ly}\alpha}$ to be strongly correlated to it. Our new $\mathrm{EW}_{\mathrm{Ly}\alpha}$ model allows us to infer the emergent Lyα strength of a galaxy based on an easily observable UV property, and will hopefully prove to be useful in future measurements of reionization history as a baseline model of emergent Lyα .

In this thesis, I have aimed to answer: What are the emergent properties of the first galaxies (z$\sim 7-10$)? In my two publications and my upcoming paper, I have attempted to answer this from the angle of Lyα and the ionizing photon production, using galaxies near the end of the EoR as analogs. Overall, we have found a rich distribution of ξ_{ion} in UV-faint galaxies above z>3 and its correlation to UV observables. We have found that overall, UV-faint Lyα galaxies tend to have small $\Delta v_{\mathrm{Ly}\alpha}$ compared to massive UV-bright galaxies. And we have constructed empirical Bayesian models to connect Lyα emission to easy to observe UV continuum properties. All of this with the goal of procuring new insight and tools for the future of studying the reionization timeline at z>7.

My thesis is divided in 3 chapters. In the second chapter I present for the first time results on the non-escaping ionizing photon production of UV-faint galaxies (Prieto-Lyon et al., 2023a). In Chapter 3, I show for the first time the emergent wavelength of Lyα from the faintest galaxies at z $\sim 3-6$ (Prieto-Lyon et al., 2023b). In Chapter four I present my upcoming work Prieto-Lyon et al.(in prep) which focuses on an empirical Bayesian model of the emergent Lyα equivalent width based in UV observables at the EoR. The thesis reaches its end with a summary of my work and prospects for the future of the area.

THE FIRST LOOK INTO THE FAINTEST IONIZERS

2

This chapter contains the following article written by me as the main author:

"The production of ionizing photons in UV-faint z $\sim$ 3 - 7 galaxies"

Published in Astronomy & Astrophysics : Volume 672, Article 186, 10 pp. (April 2023)

Authors: ***Gonzalo Prieto-Lyon****, Victoria Strait, Charlotte A. Mason, Gabriel Brammer, Gabriel B. Caminha, Amata Mercurio, Ana Acebron, Pietro Bergamini, Claudio Grillo, Piero Rosati, Eros Vanzella, Marco Castellano, Emiliano Merlin, Diego paris, Kristian Boyett, Antonello Calabro, Takahiro Morishita, Sara Mascia, Laura Pentericci, Guido Roberts-Borsani, Namrata Roy, Tomasso Treu and Benedetta Vulcani*

Abstract

The demographics of the production and escape of ionizing photons from UV-faint early galaxies is a key unknown that has hindered attempts to discover the primary drivers of reionization. With the advent of JWST, it is finally possible to observe the rest-frame optical nebular emission from individual sub-L^* $z > 3$ galaxies to measure the production rate of ionizing photons, $\xi_{\rm ion}$.

Here we study a sample of 370 $z \sim 3 - 7$ galaxies spanning $-23 < M_{\rm UV} < -15.5$ (median $M_{\rm UV} \approx -18$) with deep multiband HST and JWST/NIRCam photometry that covers the rest-UV to the optical from the GLASS and UNCOVER JWST surveys. Our sample includes 102 galaxies with Lyman-alpha emission detected in MUSE spectroscopy. We used Hα fluxes inferred from NIRCam photometry to estimate the production rate of ionizing photons that do not escape these galaxies, $\xi_{\rm ion}(1 - f_{\rm esc})$.

We find median $\log_{10} \xi_{\rm ion}(1 - f_{\rm esc}) = 25.33 \pm 0.47$, with a broad intrinsic scatter of 0.42 dex, which implies a broad range of galaxy properties and ages in our UV-faint sample. Galaxies detected with Lyman-alpha have ~ 0.1 dex higher $\xi_{\rm ion}(1 - f_{\rm esc})$, which is explained by their higher Hα equivalent width distribution; this implies younger ages and higher specific star formation rates and, thus, more O/B stars. We find significant trends of increasing $\xi_{\rm ion}(1 - f_{\rm esc})$ with increasing Hα equivalent width, decreasing UV luminosity, and decreasing UV slope; this implies that the production of ionizing photons is enhanced in young galaxies with assumed low metallicities. We find no significant evidence for sources with very high ionizing escape fractions ($f_{\rm esc} > 0.5$) in our sample based on their photometric properties, even amongst the Lyman-alpha-selected galaxies.

This work demonstrates that considering the full distribution of $\xi_{\rm ion}$ across galaxy properties is important for assessing the primary drivers of reionization.

2.1 Introduction

In recent years, we have obtained increasing evidence that the reionization of hydrogen happened fairly late, approximately one billion years after the Big Bang ($z \sim 5.5 - 10$), with a mid-point around $z \sim 7 - 8$ (e.g., Fan et al., 2006; Stark et al., 2010; McGreer et al., 2015;

Mason et al., 2018a; Davies et al., 2018; Qin et al., 2021; Planck Collaboration et al., 2020; Bolan et al., 2022). However, there is evidence for significant star formation before this time (e.g., Oesch et al., 2018; Hashimoto et al., 2018; McLeod et al., 2021), and thus it appears that reionization lags behind galaxy formation. The reason for this lag is unknown: we are still lacking a full physical understanding of the reionization process. In particular, we still do not know which types of galaxies drive the process, that is to say, which physical mechanisms mediate the production and escape of ionizing photons from galaxies. In order to produce such a late and fairly rapid reionization, the ionizing population could have been dominated by low mass, UV-faint galaxies with a low average escape fraction ($\sim$ 5%; e.g., Mason et al., 2019; Qin et al., 2021). Alternatively, rarer, more massive galaxies with higher escape fractions could have been responsible (e.g., Sharma et al., 2017; Naidu et al., 2020). With only measurements of the timing of reionization, these scenarios are degenerate, and thus physical priors on the ionizing properties of galaxies across cosmic time are necessary to pinpoint the sources of reionization.

The total ionizing output of galaxies can be simply parameterized (e.g., Madau et al., 1999; Robertson et al., 2010) as the product of the production rate of ionizing photons relative to non-ionizing UV photons, ξ_{ion} (determined by the stellar populations; e.g., Stanway et al., 2016) and the fraction of ionizing photons that escape the interstellar medium (ISM) into the intergalactic medium, f_{esc} (determined by the structure and ionization state of the ISM, which is likely shaped by star formation and feedback; e.g., Trebitsch et al., 2017; Ma et al., 2020). Both of these quantities are also expected to vary with time in an individual galaxy, for example due to the lifetime and properties of young stellar populations, and depending on the effects of feedback and bursty star formation on the ISM.

While we can easily observe the non-ionizing UV photons from galaxies, the high optical depth of the intergalactic medium to ionizing photons makes direct measurements of the escaping ionizing spectrum statistically unlikely at $z \gtrsim 3$ (Inoue et al., 2014; Becker et al., 2021; Vanzella et al., 2018b). Alternatively, fluxes of nonresonant recombination lines, emitted by gas that was ionized in HII regions around massive stars, can crucially measure the flux of ionizing photons that do not escape galaxies. In particular, Hα emission can be used to directly estimate $(1-f_{\rm esc})\xi_{\rm ion}$ (e.g., Leitherer & Heckman, 1995; Bouwens et al., 2016b; Shivaei et al., 2018; Emami et al., 2020). As $f_{\rm esc}$ is inferred to be low ($\lesssim 10\%$) on average for Lyman-break galaxies at $z \sim 2-4$ (Steidel et al., 2018; Begley et al., 2022; Pahl et al., 2023), measurements of Hα should trace the intrinsic production of ionizing photons reasonably well. The value of $\xi_{\rm ion}$ can also be inferred from the strength of [OIII]+Hβ emission; however, due to the dependence of [OIII] emission on metallicity and the ionization parameter, the correlation is not as tight as with Hα (e.g., Chevallard et al., 2018).

Previous work at $z \lesssim 2.5$, where direct Hα spectroscopy has been possible from the ground, has found a mean $\log_{10}\xi_{\rm ion}[\rm erg\ Hz^{-1}] \approx 25.3$, with a scatter of ~ 0.3 dex, likely dominated by variations in stellar populations between galaxies (e.g., Shivaei et al., 2018; Tang et al., 2019). At higher redshifts, where Hα redshifts into the infrared, broadband photometry with *Spitzer* has been used extensively to estimate Hα line fluxes (e.g., Schaerer & de Barros, 2009; Shim et al., 2011; Stark et al., 2013; Smit et al., 2015; Bouwens et al., 2016b; Lam et al., 2019a; Maseda et al., 2020; Stefanon et al., 2022).

However, due to the limited spatial resolution and sensitivity of *Spitzer*, previous works were limited to studying $\xi_{\rm ion}$ in isolated, bright ($> L^*$) galaxies, where de-blending *Infrared Array Camera* (IRAC) photometry was possible (e.g., Bouwens et al., 2016b), and using stacks for fainter galaxies (e.g., Lam et al., 2019a; Maseda et al., 2020). With *James Webb Space Telescope* (JWST) it is finally possible to extend these studies to individual UV-faint galaxies (Endsley et al., 2022b) and obtain rest-frame optical spectroscopy at $z > 3$ (e.g., Sun et al., 2022; Williams et al., 2022).

Results from previous analyses have been intriguing but require further investigation. Using stacked IRAC photometry, Lam et al. (2019a) find no significant evidence for a strong correlation of $\xi_{\rm ion}$ with $\rm M_{UV}$. However, Maseda et al. (2020) find a population of extremely UV-faint galaxies ($\rm M_{UV} > -16$) selected as Lyα emitters in deep *Multi Unit Spectroscopic Explorer* (MUSE) observations, which have very elevated $\xi_{\rm ion}$ compared to higher luminosity galaxies and at fixed Hα equivalent widths (EWs), which implies that these efficient ionizing galaxies are particularly young and of low metallicity. It is thus important to examine the distribution of $\xi_{\rm ion}$ at low UV luminosities, and to compare galaxies with and without Lyα emission to better understand the demographics of the ionizing population.

Furthermore, using early JWST NIRCam data, Endsley et al. (2022b) discovered a population of UV-faint galaxies ($M_{\rm UV} \sim -19$) at $z \sim 6.5 - 8$ with high specific star formation rates (sSFRs) but low EW [OIII]+Hβ inferred from photometry. The high sSFR would imply high $\xi_{\rm ion}$ due to the increased abundance of O and B stars. To explain the low [OIII]+Hβ EW, Endsley et al. (2022b) suggest that either these galaxies have extremely low metallicities (reducing oxygen abundance) or, alternatively, that all nebular lines are reduced. A reduction in all nebular lines could be due to either them being produced in density-bounded HII regions with a very high ionizing escape fraction (e.g. Zackrisson et al., 2013; Marques-Chaves et al., 2022) or a recent cessation of star formation. At $z \sim 3 - 7$, both [OIII]+Hβ and Hα are visible in NIRCam photometry, enabling us to test these scenarios.

In this paper we make use of deep multiband *Hubble* Space Telescope (HST)/ACS, WFC3, and JWST/NIRCam imaging with overlapping MUSE observations, which enables us to blindly detect a spectroscopic sample with precision rest-frame UV-to-optical photometry. We measure the distribution of $\xi_{\rm ion}$ over a broader luminosity range ($-23 \lesssim M_{\rm UV} \lesssim -15.5$) than previously possible in individual galaxies thanks to the excellent resolution and sensitivity of NIRCam at rest-optical wavelengths compared to *Spitzer*/IRAC as well as the power of gravitational lensing. We explore correlations of $\xi_{\rm ion}$ with empirical galaxy properties. We find significant trends of increasing $\xi_{\rm ion}$ with decreasing UV luminosity, decreasing UV β slope, and increasing Hα EW, all of which implies that the strongest ionizers are young sources with expected low metallicities. We also explore whether our sample shows evidence for very low metallicities or an extremely high escape fraction.

The paper is structured as follows. In Sect. 3.2 we describe the photometric and spectroscopic data for our study. In Sect. 2.3 we describe how we infer the ionizing production rate, $\xi_{\rm ion}$, and in Sect. 3.4 we describe the correlations we find between $\xi_{\rm ion}$ and other galaxy properties and present a comparison to the literature. We discuss our results and state our conclusions in Sect. 4.7.

We assume a flat Λ cold dark matter cosmology with $\Omega_m = 0.3,\ \Omega_\Lambda = 0.7$ and $h = 0.7$. All magnitudes are in the AB system.

2.2 DATA

For this work we selected fields with multiband HST/ACS and JWST/NIRCam imaging and overlapping MUSE spectroscopy. We selected sources detected with Lyα emission ($z \sim 2.9-6.7$ in MUSE) and sources with a high probability of being in the same redshift range based on photometric redshift, and we used the HST + JWST photometry to extract optical emission line fluxes. Below we describe the data sets and the selection of our sample.

2.2.1 IMAGING

We used JWST NIRCam imaging in parallel to and of the cluster Abell 2744 from the GLASS-JWST program ERS-1324 (PI Treu Treu et al., 2022) and the UNCOVER* program GO-2561 (co-PIs Labbé and Bezanson).

The GLASS-JWST NIRCam observations discussed in this paper were taken in parallel to NIRISS observations of the cluster Abell 2744 on June 28-29, 2022. They are centered at RA= 3.5017025 deg and Dec= -30.3375436 deg and consist of imaging in seven bands: F090W (total exposure time: 11520 seconds), F115W (11520 s.), F150W (6120 s.), F200W (5400 s.), F277W (5400 s.), F356W (6120 s.), and F444W (23400 s.). The UNCOVER NIRCam observations of the Abell 2744 cluster were taken on November 2-15, 2022. They are centered at RA=3.5760475 deg and Dec= -30.37946 deg and consist of imaging in seven bands: F115W (10823 s.), F150W (10823 s.), F200W (6700 s.), F277W (6700 s.), F356W (6700 s.), F410M (6700 s.), and F444W (8246 s.).

In our analysis, we also included new and archival HST imaging; the ACS imaging is particularly important for constraining photometric redshifts. This includes new HST/ACS data in F606W (59530 s.), F775W (23550 s.), and F814W (123920 s) from HST-GO/DD program 17231† (PI Treu), as well as archival data acquired under the *Hubble* Frontier Fields program (HST-GO/DD-13495, PI Lotz; Lotz et al., 2017), BUFFALO (HST-GO-15117 PI

---

[*] `https://www.stsci.edu/jwst/science-execution/program-information.html?id=2561`

[†] `https://www.stsci.edu/cgi-bin/get-proposal-info?id=17231&observatory=HST`

Steinhardt; Steinhardt et al., 2020), and programs HST-GO-11689 (PI Dupke), HST-GO-11386 (PI Rodney), HST-GO-13389 (PI Siana), HST-GO-15940 (PI Ribeiro), and HST-SNAP-16729 (PI Kelly). Not all HST bands cover every object in our sample, and we only kept objects in our sample that have a well-constrained photometric redshift, usually meaning that there is ACS coverage (see Sect. 2.2.4). We also included HST/WFC3 imaging for completeness, but it is generally not as constraining as the NIRCam fluxes.

The image reduction and calibration, and the methods used to detect sources and measure multiband photometry in both fields, closely follow that of Brammer et al., (in prep). Briefly, we pulled calibrated images from the *Mikulski Archive for Space Telescopes* (MAST) [‡] and processed them with the `grizli` pipeline (Brammer et al., 2022). The pipeline first aligns the exposures to external catalogs and to one another and corrects for any distortion within the image. Following this, we subtracted a sky-level background, divided out flat-field structure using custom flat-field images, and corrected for $1/f$ noise. We also corrected for NIRCam image anomalies, which include persistence, any remaining cosmic rays, and "snowballs" (see Rigby et al., 2022). Finally, we applied zero-point corrections calculated by G. Brammer[§] and drizzled all exposures to a common pixel grid.

For source detection, we used SEP, Source Extraction and Photometry (Barbary, 2018), to perform aperture photometry on the F444W detection image in each field.

2.2.2 Lyα Spectra: VLT/MUSE spectroscopy

MUSE spectroscopy of the Abell 2744 cluster was obtained through ESO program 094.A-0115 (PI Richard) and is described by Mahler et al. (2018) and Richard et al. (2021). We used their publicly available catalog to select Lyα -emitting galaxies. The data comprise a 4 sq. arcmin mosaic centered on the cluster core. Four 1 sq. arcmin quadrants were observed for a total of 3.5, 4, 4, and 5 hours, respectively, and the center of the cluster was observed for an additional 2 hours. The median line flux 1σ uncertainty in the MUSE data is 3.6×10^{-19} erg s^{-1} cm^{-2}. This corresponds to a 5σ EW limit of $\sim 4 - 30$ Å over $z \sim 3 - 7$ for a galaxy with $M_{UV} = -19$ (the median for our sample before accounting for magnification as EW is

---

[‡] https://archive.stsci.edu

[§] https://github.com/gbrammer/grizli/pull/107 invariant under magnification).

Very Large Telescope (VLT)/MUSE spectroscopy in the GLASS-JWST NIRCam fields were obtained through a new ESO Director's Discretionary Time program, 109.24EZ.001 (co-PIs Mason, Vanzella), on the nights of July 28 and August 20, 2022. The data comprise five pointings (four of which are over 4 sq. arcmin and overlap with NIRCam imaging), each with 1 hour of exposure time. The raw data are publicly available on the ESO archive[¶]. The reduction, calibration, and source detection methods used for this work are identical to techniques described in Caminha et al. (2017) and Caminha et al. (2019). A full assessment of the depth is ongoing, but, based on the ~ 4 hour depth of the Mahler et al. (2018) observations described above, we estimate a 5σ EW limit of $\sim 8-60$ Å in these shallower data.
In this work we used 102 spectroscopic confirmations at $z \sim 2.9-6.7$: 42 from the GLASS-JWST NIRCam fields and 60 from the Abell 2744 cluster field.

2.2.3 Gravitational lensing magnification

For the galaxies detected in the core of the Abell 2744 cluster, we corrected for gravitational lensing magnification using the model from Bergamini et al. (2022). The median magnification of the sample is $\mu = 3.54$, and 90% of the galaxies have $\mu = 2-20$. We removed sources with a magnification with $\mu > 50$ (12 sources) due to high uncertainties in the model near the critical curves. The galaxies in the parallel fields are $\sim 3-10'$ away from the cluster core, where the magnification is expected to be modest ($\mu \approx 1$). We do not account for the magnification of these sources.

2.2.4 Sample selection

For this work we focused on selecting a sample of galaxies at $z \sim 3-7$ with high purity. We selected 102 MUSE Lyα -detected galaxies with overlapping HST/ACS and JWST/NIRCam data as described above. We also selected a comparison sample of galaxies based on peak photometric redshift, within the same footprint as the MUSE observations, which we expect to

---

[¶] `http://archive.eso.org/wdb/wdb/eso/sched_rep_arc/query?progid=109.24EZ.001`

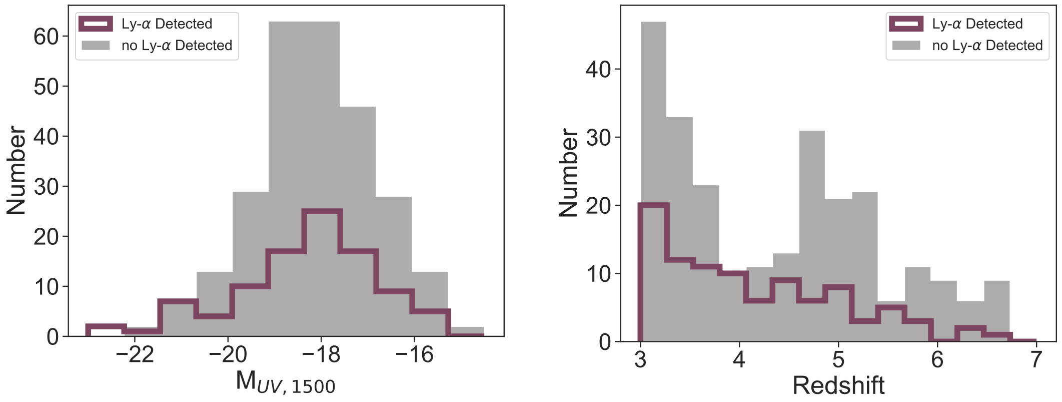

Figure 2.1: Galaxies studied in this work: Lyα -detected galaxies (in purple) and galaxies photometrically selected (with no Lyα detected, in gray). *Left:* Distribution of redshifts for the spectroscopic and photometric samples. We show the spectroscopic redshift, where available, or the peak photometric redshift. *Right:* UV magnitude distribution for our sample. We find a median value of -18.14 ± 1.58, with no statistically significant difference between the two samples.

have slightly lower Hα EWs than the Lyα selected sample.

We found the photometric redshift distribution of all sources detected as described in Sect. 3.2.2 using EAZY (Brammer et al., 2008) and using all available photometric bands. To build a photometric sample with high purity, following Bouwens et al. (2016b), we selected sources with the peak of their photometric redshift between $2.9 < z < 6.7$ and kept only sources that have 90% of the redshift probability density between $\Delta z \sim 1$ of the peak of their distribution. The resulting high purity photometric sample consists of 268 galaxies.

The redshift and UV magnitude distribution of our sample is shown in Figure 2.1. The median redshift of the full sample is 4.02, and the Lyα -selected sample has a median redshift of 3.95. The median M_{UV} is -18.1, with a Kolmogorov-Smirnov (KS) test showing no significant difference between the Lyα - and photometrically selected samples.

2.3 Inferring the ionizing photon production rate

2.3.1 Inferring nebular emission line strengths from photometry

To estimate nebular emission line fluxes from broadband photometry, we followed approaches in the literature and fit the spectral energy distribution (SED) to the full photometry, excluding bands we expected to contain strong nebular emission lines (e.g., Shim et al., 2011; Stark et al., 2013; Mármol-Queraltó et al., 2016; Bouwens et al., 2016b). This provided us with a model for the continuum flux in those bands that we could subtract from the observed photometry to infer the line flux.

We used BAGPIPES to fit SEDs (Carnall et al., 2018). We adopted BC03 (Bruzual & Charlot, 2003) templates and excluded any nebular emission contribution. We did not consider any broadbands where Hα or [OIII]+Hβ are observed according to each galaxy's redshift. For ease of comparison to the literature (e.g., Maseda et al., 2020; Lam et al., 2019a), we assumed a Chabrier (2003) initial mass function and a Small Magellanic Cloud (SMC; Prevot et al., 1984) dust attenuation law, allowing A_V to vary from $0-3$ mag. Because metallicity is not well known at the range of redshifts we explored, we allowed metallicity to vary from $0-2\,Z_{\odot}$. And because star formation histories are notoriously difficult to constrain at high redshifts (Strait et al., 2021), we assumed an exponentially rising delayed τ star formation history, allowing τ to vary freely. For the spectroscopically confirmed Lyman α emitters, we fixed the redshift at the Lyα redshift. For our photometric sample, we used the photometric redshift obtained from EAZY with a uniform prior with $\Delta z = 1$ (see Sect. 2.2.4).

We then compared the SED model of the galaxy's continuum to the broadbands where Hα or [OIII]+Hβ fall. We multiplied the non-nebular SED posteriors by the transmission of the aforementioned broadbands to obtain the contribution of the galaxy's continuum to the observed flux. By subtracting this continuum flux contribution from the observed photometry, we were then able to recover the flux distributions of the Hα and [OIII]+Hβ emission lines for each galaxy. We compared our measurements with a sample of six galaxies with [OIII]+Hβ EW measurements from the GLASS-ERS program using JWST/NIRISS (Boyett et al., 2022a), finding that our method recovers the EW of these sources to within $\sim 20-$

40%. A full comparison of these photometric inference methods is left to future work.

There are some limitations to our method for obtaining line fluxes, such as contamination from the 4000 Å break in the broadband that contains [OIII]+Hβ , the chance that the line falls outside the effective width of any of our broadband filters, or Hα and [OIII]+Hβ falling on the same band. We considered a contribution of 6.8% from [NII] to the calculated Hα flux, and 9.5% from [SII] according to Anders & Fritze-v. Alvensleben (2003). We removed galaxies with a poor χ^2 score (>50) on their SED fit; we chose this value by ignoring all galaxies on the high end of the χ^2 distribution.

The advantage of this approach, unlike estimating line fluxes directly from the SED fitting, is that it does not depend strongly on star formation history assumptions and allows us to make a mostly empirical measurement of the line fluxes. We obtain comparable results using the flux in the band redward of Hα as the continuum flux, assuming a flat optical continuum (see also, e.g., Maseda et al., 2020). Estimating other physical parameters, such as the star formation rate and stellar mass, from the SED fitting did not give reliable results. This is because the fitting was too dependent on the initial assumptions and needed extremely young ages (<10Myrs) and an instantaneous burst of star formation to recreate the observed nebular emissions.

The following results consist of 83 and 64 Lyα -emitting galaxies with Hα and [OIII]+Hβ emissio line measurements, respectively, and a photometric sample of 220 and 203 galaxies with Hα and [OIII]+Hβ emission line measurements, respectively. We see both lines in 62 Lyα galaxies and 177 photometrically selected galaxies. We see no apparent biases in our $\mathrm{M_{UV}}$ distribution after narrowing down the sample. Nebular emission flux errors are derived from the 68% confidence interval of the resulting distributions.

2.3.2 Measuring UV absolute magnitude and slope

To infer the UV absolute magnitude, $\mathrm{M_{UV}}$ (magnitude at 1500Å), and β slope, we fit the power law (e.g., Rogers et al., 2013) $f_\lambda \propto \lambda^\beta$ to the fluxes from the HST and JWST bands.

We performed the fit using a Markov chain Monte Carlo sampling and the python module `emcee` (Foreman-Mackey et al., 2013). We assumed flat priors for β and M_{UV}, with bounds $-4 < \beta < 1$ and $-25 < M_{UV} < -12$, sufficient to explore the common value ranges for galaxies (e.g., Bouwens et al., 2014).

To obtain the photometric bands that are observing the UV rest frame of our galaxies, we excluded any bands that fall blueward of Lyman-α and might be affected by the Lyman break. For the same reason, we excluded bands redward of the 4000Å break in the rest frame. After these requirements, we are left with three or four bands for each source. In the case of galaxies with Lyman-α detected in MUSE, we used the line's redshift. For photometrically selected galaxies, in each call of the likelihood, we randomly drew a redshift from a Normal distribution, $N(\mu = z_{phot}, \sigma = 0.5)$, and selected the appropriate photometric bands. For lensed sources, we considered magnifications and applied them following the same random draw method as for the redshift. We used the corresponding magnification and error obtained from the Bergamini et al. (2022) lensing model.

2.3.3 DETERMINATION OF ξ_{ion}

We define the production rate of ionizing photons, ξ_{ion}, as the ratio between the luminosity of observed ionizing photons and the intrinsic luminosity of the ionizing UV photons (e.g., Leitherer & Heckman, 1995):

$$\xi_{\text{ion}} = \frac{L_{\text{H}\alpha}}{(1 - \text{f}_{\text{esc}})L_{\text{UV},\nu}^{\text{intr}}} \times 7.37 \times 10^{11} \text{ Hz erg}^{-1} \tag{2.1}$$

where $L_{\text{H}\alpha}$ is the unattenuated Hα luminosity in erg s^{-1} and $L_{\nu,\text{UV,intr}}$ is the intrinsic UV luminosity density at 1500Å. The models from where the conversion factor is derived assume a young population of massive stars equivalent to a massive HII region. We assumed this type of environment to be similar to what we would find in young galaxies.

Because Hα is produced by the excitation of hydrogen gas from ionizing radiation that does not escape the galaxy, and because we cannot directly measure f_{esc} in our sample, we note that the production rate we obtain is for ionizing photons that did not escape the galaxy, $\xi_{\rm ion}$ (1 - $f_{\rm esc}$).

We first calculated $L_{\rm H\alpha}$ directly from the SED obtained in Sect. 2.3.1, after accounting for dust attenuation (Prevot et al., 1984). To obtain the intrinsic value of the UV luminosity, we took the dust attenuation into account following Lam et al. (2019a), who defined the intrinsic UV luminosity as :

$$L_{\rm UV,\nu}^{\rm intr} = L_{\rm UV,\nu}/f_{\rm esc,UV}$$

Where $f_{\rm esc,UV}$ is the fraction of escaping UV photons not absorbed by the dust. For this, we used the SMC dust law defined by Prevot et al. (1984):

$$f_{\rm esc,UV} = 10^{-1.1(\beta+2.23)/2.5}, \quad \beta > -2.23 \tag{2.2}$$

Where β is the UV slope obtained in Sect. 2.3.2. Galaxies with slopes bluer than $\beta <$ -2.23 were assumed to be dust-free and therefore not corrected for dust. In the following, uncertainties on $\xi_{\rm ion}$ are at the 68% confidence intervals and were obtained from propagating the uncertainty in the Hα flux from its resulting distribution, as described in Sect. 2.3.1. The posterior distributions for β and $M_{\rm UV}$ were obtained as described in Sect. 2.3.2.

2.3.4 Correlation analysis

For the purpose of studying the correlations between galaxy properties, we used the python package `linmix`[‖] to perform Bayesian linear regression, including intrinsic scatter and accounting for two-dimensional errors (Kelly, 2007). We fit for $\log_{10}[(1-f_{\rm esc})\xi_{\rm ion}] = \alpha+\beta X+\varepsilon$, where ε is the intrinsic scatter and is assumed to be normally distributed with a variance of σ_ε^2. We recovered the best-fit trend line from the posteriors as well the 68% confidence interval on the parameters. We report the results in Table 2.1 and show the best-fit line in the figure plots.

[‖] `https://github.com/jmeyers314/linmix`

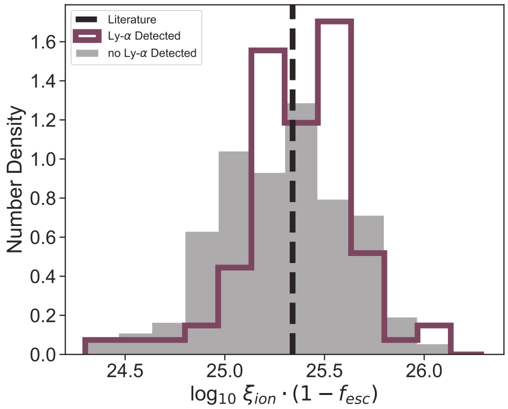

Figure 2.2: Distribution of (1-$f_{\rm esc}$)$\xi_{\rm ion}$. The purple histogram includes galaxies with Lyα emission detection and the gray, galaxies without. Overall, Lyα -emitting galaxies show stronger ionizing photon production than galaxies with no Lyα emission, with median values 25.39±0.64 and 25.31±0.43, respectively. We show the median relation from the literature at $z \sim 2-5$ as a dashed black line (e.g., Shivaei et al., 2018; Bouwens et al., 2016b; Lam et al., 2019a)

2.4 RESULTS

In this section we present our results. In Sect. 2.4.1 we study the trends between $\xi_{\rm ion}$, EW$_{\rm H\alpha}$, M$_{\rm UV}$, and the β slope, and in Sect. 2.4.2 we investigate whether our sample shows evidence for galaxies with very high ionizing photon escape fractions and/or very low metallicities.

2.4.1 BEHAVIOR OF $\xi_{\rm ion}$

Figure 2.2 shows the distribution of $(1 - f_{\rm esc})\xi_{\rm ion}$ for our Lyα -selected and photometric samples. We find median values of $\log_{10} \xi_{\rm ion}$ 25.39±0.64 and 25.31±0.43, respectively, and 25.33±0.47 [Hz erg^{-1}] for the complete data set. We find an intrinsic scatter of 0.42 dex, obtained by subtracting in quadrature the average uncertainty in $\log_{10} \xi_{\rm ion}$ ($= 0.21$ dex) from the standard deviation of the observed distribution. The recovered intrinsic scatter is broader by ~ 0.1 dex than that found by Bouwens et al. (2016b) and Shivaei et al. (2018) in M$_{\rm UV} \lesssim -20$ galaxies. The broad distribution of $\xi_{\rm ion}$ is likely an outcome of the broad range of stellar populations in these galaxies, that is to say, due to a range of star formation histories (and thus ages) and stellar metallicities (see e.g., Shivaei et al., 2018).

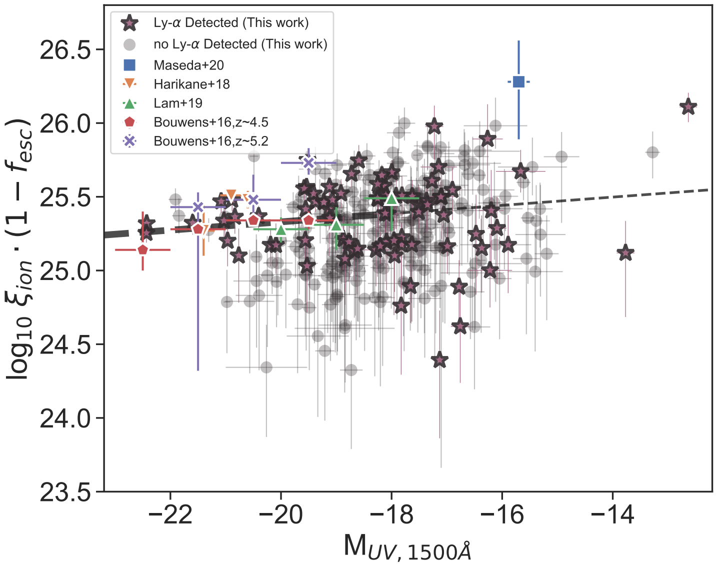

Figure 2.3: M_{UV} vs. (1-f_{esc})ξ_{ion}. Lyα-detected galaxies are shown with purple stars and photometrically selected sample with no Lyα detected with gray circles. We show data from Maseda et al. (2020), Harikane et al. (2018), Lam et al. (2019a), and Bouwens et al. (2016b) as colored boxes for comparison. We find evidence for an increase in $\log_{10}[(1-f_{esc})\xi_{ion}]$ toward fainter UV magnitudes, with a slope of 0.03 ± 0.02, but only when considering the range where our sample is M_{UV} complete ($M_{UV} <$ -18.1). We show literature constraints at similar redshifts as colored shapes (Bouwens et al., 2016b; Harikane et al., 2018; Lam et al., 2019a; Maseda et al., 2020), noting that all constraints fainter than $M_{UV} >$ -20 were obtained by stacking IRAC photometry.

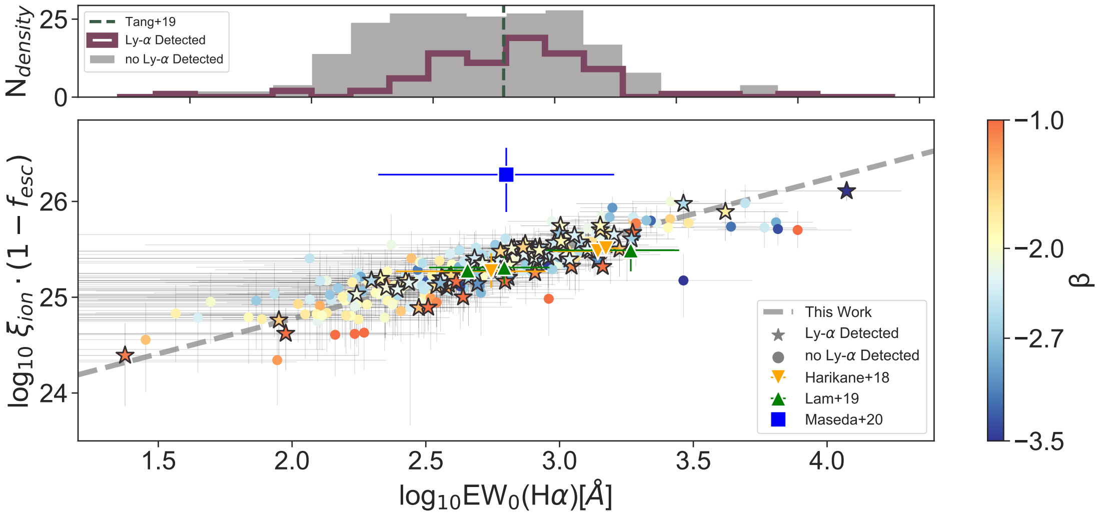

Figure 2.4: Comparison of the Hα EW with the ionizing photon production that does not escape the galaxy. Lyα -detected galaxies are shown as stars and photometrically selected galaxies with no Lyα as circles. As above, error bars are only shown for 30% of the sources for clarity. We color-code these two samples by UV β slope. In the top panel we show the distribution of Hα EWs for the same two samples compared to the values found by Tang et al. (2019). We add data from Harikane et al. (2018) and Lam et al. (2019a), which are at the high end of our observed Hα EW distribution, for comparison. We see that a higher $\xi_{\rm ion}$ correlates very strongly with a higher Hα EW. Galaxies with detected Lyα emission have an Hα EW distribution with higher values, median 732 ± 187 Å compared to 457 ± 161 with a Kolmogorov–Smirnov test p-value $\ll 0.01$. The sources with the reddest UV slopes systematically lie below the best-fit relation at fixed $\mathrm{EW}_{\mathrm{H}\alpha}$.

We performed a two-sample KS test to determine whether the Lyα -selected and photometric samples are drawn from the same distribution. We recover a p-value of 0.03, meaning it is likely that the underlying distributions are different; this is consistent with the results from Saldana-Lopez et al. (2022), where a statistically significant difference is found between the $\xi_{\rm ion}$ distributions of Lyα emitters and non-Lyα emitters at $z \sim 3-5$. Given that galaxies with strong Lyα emission also likely have high ionizing photon escape fractions (e.g., Verhamme et al., 2015; Dijkstra et al., 2016), it is likely that the intrinsic ionizing photon production efficiency of these galaxies is even higher than what we can infer based on Hα emission.

Figure 2.3 shows $(1-f_{\rm esc})\xi_{\rm ion}$ versus UV magnitude and demonstrates the revolutionary capabilities of MUSE and JWST/NIRCam: we are able to spectroscopically confirm extremely UV-faint galaxies via their high Lyα EW, and we are able to infer Hα , and therefore $\xi_{\rm ion}$, from much fainter individual galaxies than was previously possible with *Spitzer*, where

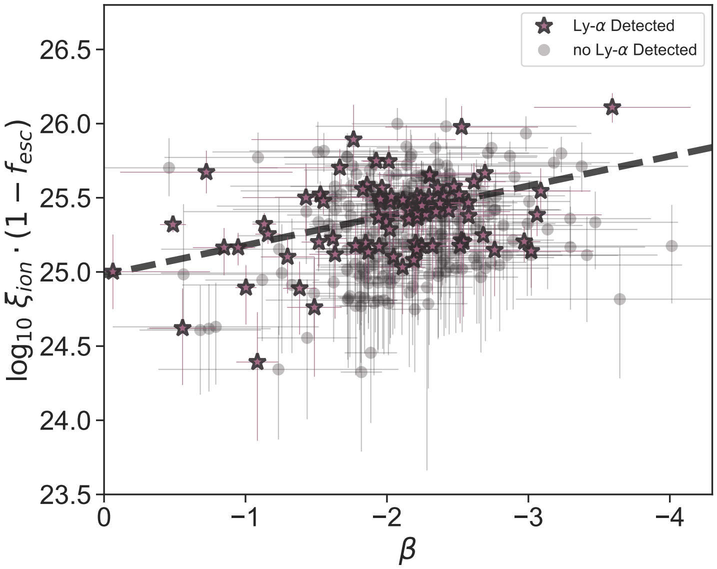

Figure 2.5: UV β slope vs. $\xi_{\rm ion}$ (1-f$_{esc}$). Lyα -detected galaxies are shown in purple and the photometrically selected sample with no Lyα detected in gray. As above, error bars are only shown for 30% of the sources for clarity. We add the stacked measurements from Lam et al. (2019a) for comparison. We find a very weak trend of increasing $\xi_{\rm ion}$ with decreasing β, with a linear slope of -0.10 ± 0.06.

stacking was necessary at $\mathrm{M}_{\mathrm{UV}} \gtrsim -20$ (e.g., Lam et al., 2019a; Maseda et al., 2020). We reach ~ 1 dex lower than any previous studies at similar redshifts and without needing to use stacking methods. We can reach individual detections of very faint galaxies, $\mathrm{M}_{\mathrm{UV}} < -17$. We also find results consistent with those at $z \sim 2$ (Shivaei et al., 2018) and at $z \sim 4-5$ for $> L^*$ galaxies (Bouwens et al., 2016b) and $< L^*$ galaxies (Lam et al., 2019a, where a stacking analysis was used), as shown in Fig. 2.2. We note that our observations demonstrate the large scatter in $(1-f_{\mathrm{esc}})\xi_{\mathrm{ion}}$ at fixed M_{UV} , which was not possible to observe in previous analyses that used the stacking of *Spitzer* photometry for UV-faint galaxies.

As described in Sect. 2.3.4, we performed a linear regression to assess correlations in our data. In contrast to Lam et al. (2019a), we find significant evidence for a weak trend between ξ_{ion} and M_{UV} , where the highest ξ_{ion} tends to come from the faintest galaxies. Since our sample is not M_{UV} complete, we only study the correlation up to the peak of our M_{UV} distribution (=-18.14) in Fig. 2.1. We find $\log_{10}[(1-f_{\mathrm{esc}})\xi_{\mathrm{ion}}] = (0.03\pm0.02)(\mathrm{M}_{\mathrm{UV}}+20)+25.36\pm0.03$, but with a large scatter (see Table 2.1).

Figure 2.4 shows that ξ_{ion} follows a strong trend with Hα EW, as found in previous work (Harikane et al., 2018; Lam et al., 2019a; Tang et al., 2019). Such works were limited to the highest Hα EW values, while we reach ~ 0.75 dex lower due to the sensitivity of NIRCam. This trend is consistent with a picture where ξ_{ion} is elevated in the youngest, most highly star-forming galaxies (e.g., Tang et al., 2019). We find $\log_{10}[(1-f_{\mathrm{esc}})\xi_{\mathrm{ion}}] = (0.73 \pm 0.04)(\log_{10} EW_{\mathrm{H}\alpha} - 2.5) + 25.15 \pm 0.02$. The measurement by Maseda et al. (2020), obtained from a stack of extremely UV-faint galaxies with high Lyα EWs, lies significantly above our sample and values from the rest of the literature, with higher $(1-f_{\mathrm{esc}})\xi_{\mathrm{ion}}$ at fixed Hα EWs. As discussed by Maseda et al. (2020), this likely implies their sources have a much lower gas-phase metallicity than other samples.

We also find that Lyα -selected galaxies have a higher Hα EW than the photometrically selected sample (median EW=732 ± 187 Å compared to 457 ± 161 Å for the photometric sample). A two-sample KS test establishes that the EW distributions of the two samples are different (p-value $\ll 0.01$). This is likely the primary driver of the increased ξ_{ion} distribution for the Lyα -selected sample (Fig. 2.2).

At a fixed Hα EW, we see a clear tendency for galaxies with very blue β UV slopes to have elevated ξ_{ion} (Fig. 2.4). This trend is also seen in the full sample (Fig. 2.5), where we find high

Table 2.1: Linear fitting parameters for trends with $\log_{10}(1-f_{\rm esc})\xi_{\rm ion}$. We fit for $\log_{10}[(1-f_{\rm esc})\xi_{\rm ion}] = \alpha + \beta X + \varepsilon$, where ε is the intrinsic scatter and is assumed to be normally distributed with variance σ_ε^2.

Parameter	Slope, α	Intercept, β	Scatter variance, σ_ε^2
$\mathrm{M_{UV}} + 20$	0.03 ± 0.02	25.33 ± 0.03	0.027 ± 0.006
$\log_{10} \mathrm{EW_{H\alpha}} - 2.5$	0.73 ± 0.04	25.14 ± 0.02	0.003 ± 0.001
$\beta + 2$	-0.20 ± 0.04	25.38 ± 0.01	0.032 ± 0.005

$\xi_{\rm ion}$ is weakly correlated to a blue β slope, but with a large scatter. We find $\log_{10}(1-f_{\rm esc})\xi_{\rm ion} = (-0.20 \pm 0.04)(\beta + 2) + 25.41 \pm 0.01$ (see Table 2.1). Similar correlations have been seen at z$\sim$6 (e.g., Ning et al., 2022). Using a KS test, we find no significant difference in the β distributions for the Lyα and photometric samples. Our sample has a median $\beta = -2.1$.

2.4.2 A SEARCH FOR HIGH-ESCAPE-FRACTION AND EXTREMELY LOW-METALLICITY GALAXIES

As well as being a tracer of the ionizing photon production of galaxies, nebular emission lines are also sensitive to the escape fraction. Zackrisson et al. (2013) proposed that in galaxies with a very high ionizing escape fraction, one would expect a reduction in nebular emission line strength ($\mathrm{EW_{H\beta}} \lesssim 30$ Å) and extremely blue UV slopes ($\beta < -2.5$) due to the lack of nebular continuum. Early JWST observations have discovered potentially very blue galaxies (Topping et al., 2022, though c.f. Cullen et al. 2023) and galaxies with weak nebular line emission yet high sSFRs (via [OIII]+Hβ ; Endsley et al., 2022b), potentially indicating a population with a high ionizing escape fraction. However, the observation of low [OIII]+Hβ line strengths could also be caused by very low gas-phase metallicity (decreasing the strength of [OIII] emission) or a recent turnoff in star formation (which would also decrease all nebular emission lines). Given the redshift range of our sample, we can infer both Hα and [OIII]+Hβ line strengths for 241 galaxies, allowing us to test these scenarios and to search for galaxies with a high escape fraction. We obtained the [OIII]+Hβ nebular line fluxes as described in Sect. 2.3.1.

In Fig. 2.6 we show UV β slopes as a function of intrinsic $\mathrm{EW_{H\alpha}}$ for our sample (where we correct for dust attenuation as described in Sect. 2.3.1). We compare our sample to the region proposed by Zackrisson et al. (2017) to have $f_{\rm esc} > 0.5$. While several sources fall into this region, and also have low [OIII]+Hβ EWs ($\lesssim 100$ Å), the uncertainties are too large to make them robust candidates. We discuss this further in Sect. 2.5.2.

Figure 2.7 shows the Hα EW as a function of [OIII]+Hβ for our sample. We see the expected positive correlation between both nebular emission lines, as these lines are all generated by the effects of stellar ionizing radiation. We see a very large scatter (with a range of $\sim$ 1.5 dex) as expected due to variations in metallicity, temperature, and the ionization parameter, all of which affect the strength of individual [OIII] galaxies (e.g., Maiolino et al., 2008; Steidel et al., 2014; Sanders et al., 2021). We find $\log_{10} {\rm EW}_{\rm H\alpha} = 0.97 \pm 0.06(\log_{10} {\rm EW}([{\rm OIII}] + {\rm H}\beta)$ - 2.5) + 2.52±0.03.

Galaxies with detected Lyα emission tend to occupy the top right of the plot, with strong nebular emission lines, suggesting they are young star-forming galaxies with low metallicities and large ionization parameters that produce the copious amounts of ionizing photons needed to power these emission lines (see e.g., Yang et al., 2017a; Du et al., 2020; Tang et al., 2021, for more detailed studies). We find the Lyα -selected galaxies have stronger [OIII]+Hβ EWs compared to the photometric population, following the trend with Hα EW in Fig. 2.4. However, as discussed by Tang et al. (2021), not all galaxies with strong nebular emission are detected in Lyα , indicating that Lyα transmission is reduced due to a high column density of neutral gas in these systems and/or inclination effects. We compare our data to a $z \sim 2$ sample by Tang et al. (2019), which was selected based on strong [OIII] emission. We find a similar correlation, but overall our ratio of Hα EW/[OIII]+Hβ EW is higher by ~0.1 dex. Given that the Tang et al. (2019) sample has a significantly subsolar gas-phase metallicity, Z < 0.3 $Z_\odot$ (Tang et al., 2021), the decrease we observe in [OIII] at fixed Hα EW would likely imply an overall lower metallicity due to a lower number of metal atoms in our sample.

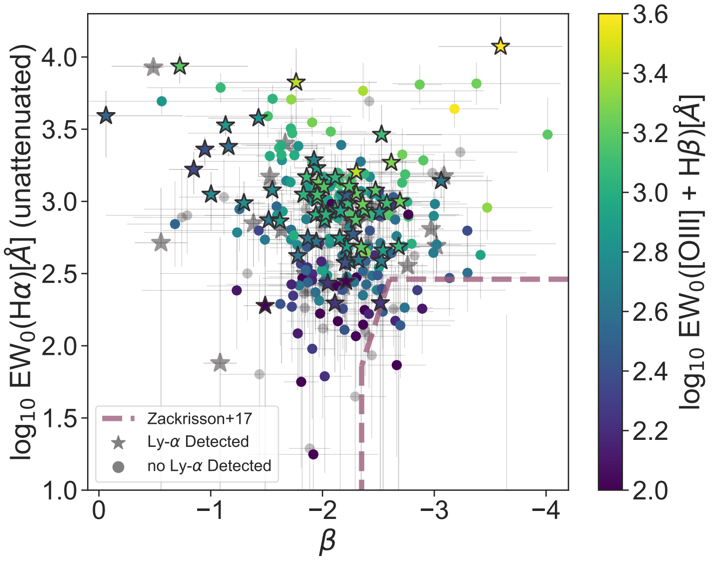

Figure 2.6: Comparison between the intrinsic (unattenuated) EW of Hα and the UV β slope, color-coded by [OIII]+Hβ EW. Lyα galaxies are shown with star-shaped markers, and the photometric sample as circles. Galaxies shown in gray do not have [OIII]+Hβ EW measurements. We show the region predicted by Zackrisson et al. (2017) to show $f_{\rm esc} > 0.5$. We rescale from Hβ EW to intrinsic Hα with a case B recombination scenario of factor 2.89, assuming a flat optical continuum in f_λ, which we confirm from the SED fitting done in Sect. 2.3.1.

2.5 DISCUSSION

2.5.1 THE PROFILE OF A STRONG IONIZER

Thanks to the depth of JWST/NIRCam, we have been able to assess trends of $\xi_{\rm ion}$ at $z > 3$ across the broadest range of galaxy properties to date. From these results, we corroborate previous work at lower redshifts and high luminosities and push the measurement of $\xi_{\rm ion}$ to a large sample of individual UV-faint galaxies for the first time.

We find that galaxies with strong ionizing photon emission tend to have high Hα EWs, low UV luminosities, blue UV β slopes, and Lyα emission – all implying that these galaxies are young and likely have a low dust content, low metallicity, and a high O/B star population that is capable of producing hard ionizing photons (e.g., Tang et al., 2019; Boyett et al., 2022b). This picture of the integrated emission from galaxies is complemented by high spatial resolu-

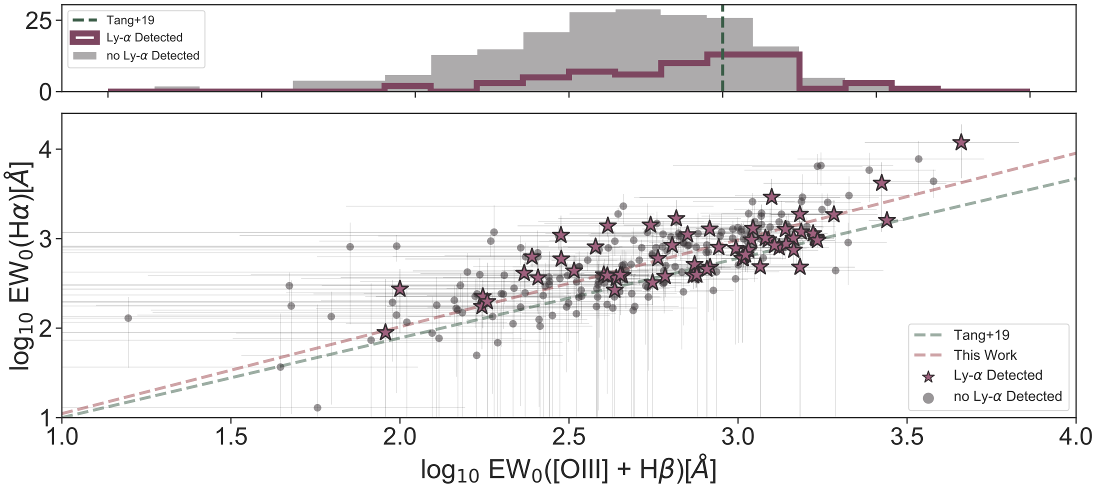

Figure 2.7: Comparison between the EW of Hα and [OIII]+Hβ . Lyα -detected galaxies are shown as stars and the photometrically selected sample with no Lyα detected as circles. In the top panel we show the distribution of [OIII]+Hβ EW for both of our samples. We find a very strong correlation between Hα EW and the [OIII]+Hβ EW, though with large scatter. The dashed lines are the correlation trends found for this work (red) and Tang et al. (2019, green). The Hα EW/[OIII]+Hβ EW is higher than the $z \sim 2$ sample from Tang et al. (2019), which was selected to have a strong [OIII] EW, implying that we might be observing lower-metallicity galaxies.

tion observations of highly magnified arcs with JWST. They have revealed extremely young star clusters ($\lesssim 10$ Myr) with [OIII]+Hβ EW > 1000 Å. They dominate the ionizing photon production in their galaxy (Vanzella et al., 2022, 2023), indicating that there can be large variations in $\xi_{\rm ion}$ in individual galaxies if they contain multiple stellar populations, but also that the variation is primarily driven by the age of the stellar populations. We also find that, overall, our Lyα galaxy sample has higher $\xi_{\rm ion}$ than the photometrically selected one; the primary reason for this difference is that the former has higher Hα EWs (Fig. 2.4). The enhanced prevalence of Lyα emission in strong Hα emitters is likely a combination of an increased production of Lyα photons due to the young stellar population implied by the strong Hα and (potentially) an increase in the Lyα escape fraction in the ISM (Tang et al., 2021; Naidu et al., 2022). In these rapidly star-forming galaxies, the hard ionizing radiation may be ionizing the ISM and/or feedback may disrupt the ISM gas, leading to a reduced HI column density and dust cover. We note that the galaxies with the highest $(1 - f_{\rm esc})\xi_{\rm ion}$ are not necessarily all Lyα emitters, likely due to variance in the geometry and column density of neutral gas and dust in these sources. Ning et al. (2022) show this same correlation between $\xi_{\rm ion}$ and Lyα for a broad range of luminosities and EWs.

2.5.2 The ionizing photon escape fraction

In Sect. 2.4.2 we explore whether our sample shows signs of high ionizing photon escape fraction, $f_{\rm esc}$, using the low Hβ EW–blue UV β slope region defined by Zackrisson et al. (2017) for $f_{\rm esc} > 0.5$. While several sources fell into this region, with both low Hα EW and [OIII]+Hβ EW ($\lesssim 100$ Å), the uncertainties on the line flux measurements are too large for them to be robust candidates. More precise emission line measurements with JWST spectroscopy will be vital for identifying such candidates and their relative abundance in the galaxy population.

The lack of high $f_{\rm esc}$ candidates amongst the Lyα -selected galaxies is also surprising. As the same conditions (a low neutral gas covering fraction) facilitate both Lyα escape and Lyman continuum escape, a correlation between the two is expected (e.g., Verhamme et al., 2015; Dijkstra et al., 2016; Reddy et al., 2016).

As discussed by Topping et al. (2022), however, it is possible for galaxies with high $f_{\rm esc}$ but very young ages to still have high nebular emission due to high ionizing photon production. It is likely that the criteria proposed by Zackrisson et al. (2017) can only find high $f_{\rm esc}$ systems within the bounds of the assumptions made for their model, such as galaxy star formation histories, ages, metallicities, and dust levels, but also the stellar models used. Our results suggest the low luminosity galaxies with high sSFRs but low [OIII]+Hβ EWs observed by Endsley et al. (2022b) may be more likely due to variations in metallicity than due to the high $f_{\rm esc}$.

2.6 Conclusions

We have inferred the hydrogen ionizing photon production rate, modulo the escape fraction, in the largest sample of individual sub-L^* $z > 3$ galaxies to date, spanning $-23 \lesssim \mathrm{M_{UV}} \lesssim -15.5$ with a median $\mathrm{M_{UV}} = -18.1$, thanks to deep JWST/NIRCam imaging. This has enabled us to track the demographics of the ionizing population. Our conclusions are as follows:

1. The median $\log_{10}(1-f_{\rm esc})\xi_{\rm ion}$ of our sample is 25.33 ± 0.47 with an intrinsic scatter of 0.42 dex. The inferred $\xi_{\rm ion}$ distribution of our sample has values in a range of ~ 1.5 dex, implying a wide range of galaxy properties and ages.

2. We find significant trends of increasing $(1-f_{\rm esc})\xi_{\rm ion}$ with increasing Hα EW, decreasing UV luminosity, and decreasing UV slope, all suggesting that the galaxies most efficient at producing ionizing photons are young, highly star-forming, and normally expected to have low metallicities and be dust-poor.

3. We find galaxies selected with strong Lyα emission to have higher $\xi_{\rm ion}$ than photometrically selected galaxies, with median $\log_{10}(1-f_{\rm esc})\xi_{\rm ion}$ values of 25.39 ± 0.64 and 25.31 ± 0.43, respectively. We find the Lyα -detected galaxies have an elevated Hα EW distribution, and thus the increased $\xi_{\rm ion}$ is likely driven by the selection based on Lyα selecting a younger population. As strong Lyα emitters also likely have high ionizing photon escape fractions, this implies the intrinsic production rate of ionizing photons in these galaxies could be significantly higher than what we can infer from Hα luminosities.

4. We examine our sample for signs of very high $f_{\rm esc}$ by comparing the inferred strengths of nebular emission lines ([OIII]+Hβ and Hα) and the strength of the nebular continuum via the UV β slope. We find no significant evidence for sources with high-escape-fraction galaxies with low nebular emission line strengths and very blue UV β slopes. The reduced strength of the [OIII]+Hβ EWs in our $z > 3$ sample compared to a sample at $z \sim 2$ from Tang et al. (2019) implies our sample likely has a lower gas-phase metallicity and/or ionization parameter.

We have demonstrated the power of JWST/NIRCam photometry to more precisely constrain the rest-frame optical emission of UV-faint high redshift galaxies than previously possible with *Spitzer*/IRAC. These observations allow us to constrain the production rate of ionizing photons from early galaxies, corroborating the picture obtained from previous stacking analyses, that $\xi_{\rm ion}$ is elevated in young, highly star-forming galaxies but that there is a broad distribution of $\xi_{\rm ion}$, likely driven by variations in galaxy properties and ages.

With JWST spectroscopy it is becoming possible to obtain direct measurements of optical emission lines in large samples (e.g., Sun et al., 2022; Williams et al., 2022; Matthee et al., 2022). Deriving a census of the ionizing photon production rate across the full galaxy population will be necessary to fully understand reionization. Here we have shown that $\xi_{\rm ion}$ is elevated in UV-faint galaxies with strong nebular emission lines, likely due to young ages. While a thorough analysis of the implications of our results for reionization is beyond the scope of this work, it becomes more prominent at high redshift (e.g., Boyett et al., 2022b; Endsley et al., 2022b), implying that it would be possible to complete reionization with modest $f_{\rm esc}$. Considering the full distributions of $\xi_{\rm ion}$ and $f_{\rm esc}$ across galaxy properties will be required to assess the primary drivers of reionization.

ACKNOWLEDGMENTS

We thank the co-PIs Ivo Labbé and Rachel Bezanson for the conception and public availability of the UNCOVER JWST Program (GO-2561), which made much of this work possible. We thank Mengtao Tang for sharing data the emission line catalog from Tang et al. (2019). This work is based on observations collected at the European Southern Observatory under ESO programmes 109.24EZ.001 and 094.A-0115. This work is based on NASA/ESA HST and JWST data which were obtained from the Mikulski Archive for Space Telescopes at the Space Telescope Science Institute, which is operated by the Association of Universities for Research in Astronomy, Inc., under NASA contract NAS 5-03127 for JWST. The HST observations are associated with programs GO/DD-17231, GO/DD-13495, GO-15117, GO-11689, GO-11386, GO-13389, GO-15940 and SNAP-16729. The JWST observations are associated with programs JWST-ERS-1324 and GO-2561. CM and GP acknowledge support by the VILLUM FONDEN under grant 37459. The Cosmic Dawn Center (DAWN) is funded by the Danish National Research Foundation under grant DNRF140. We acknowledge financial support from NASA through grant JWST-ERS-1324. We acknowledge support from the INAF Large Grant 2022 "Extragalactic Surveys with JWST" (PI Pentericci), and support through grants PRIN-MIUR 2017WSCC32, 2020SKSTHZ. This research is supported in part by the Australian Research Council Centre of Excellence for All Sky Astrophysics in 3 Dimensions (ASTRO 3D), through project number CE170100013.

THE EMERGENCE OF LYMAN-ALPHA FROM THE FAINTEST GALAXIES 3

This chapter contains the following article written by me as the main author:

"Early Results from GLASS-JWST XXIII: The transmission of Lyman-alpha from UV faint z $\sim$ 3 - 6 galaxies"

Published in The Astrophysical Journal: Volume 956, Issue 2, id.136, 10 pp. (October 2023)

Authors: ***Gonzalo Prieto-Lyon****, Charlotte Mason, Sara Mascia, Emiliano Merlin, Namrata Roy, Alaina Henry, Guido Roberts-Borsani, Takahiro Morishita, Xin Wang, Kit Boyett, Patricia Bolan, Themiya Nanayakkara, Diego Paris, Laura Pentericci, Claudia Scarlata, Michele Trenti, Tommaso Treu, Eros Vanzella*

ABSTRACT

Lyman-alpha (Lyα) emission from galaxies can be used to trace neutral hydrogen in the epoch of reionization, however, there is a degeneracy between the attenuation of Lyα in the intergalactic medium (IGM) and the line profile emitted from the galaxy. Large shifts of Lyα redward of systemic due to scattering in the interstellar medium can boost Lyα transmission in the IGM during reionization. The relationship between Lyα velocity offset from systemic and other galaxy properties is not well-established at high-redshift or low luminosities, due to the difficulty of observing emission lines which trace systemic redshift. Rest-frame optical spectroscopy with JWST/NIRSpec has opened a new window into understanding of Lyα at $z > 3$. We present a sample of 12 UV-faint galaxies ($-20 \lesssim M_{\rm UV} \lesssim -16$) at $3 \lesssim z \lesssim 6$, with Lyα velocity offsets, $\Delta v_{\rm Ly\alpha}$, measured from VLT/MUSE and JWST/NIRSpec from the GLASS-JWST Early Release Program. We find median $\Delta v_{\rm Ly\alpha}$ of 205 km s^{-1} and standard deviation 75 km s^{-1}, compared to 320 and 170km s^{-1} for $M_{\rm UV} < -20$ galaxies in the literature. Our new sample demonstrates the previously observed trend of decreasing Lyα velocity offset with decreasing UV luminosity and optical line velocity dispersion, extends to $M_{\rm UV} \gtrsim -20$, consistent with a picture where the Lyα profile is shaped by gas close to the systemic redshift. Our results imply that during reionization Lyα from UV-faint galaxies will be preferentially attenuated, but that detecting Lyα with low $\Delta v_{\rm Ly\alpha}$ can be an indicator of large ionized bubbles.

3.1 INTRODUCTION

Lyman-alpha (1216 Å, Lyα) emission from astrophysical sources has long been used as a tracer of neutral gas in the intergalactic medium (IGM) (e.g., Gunn & Peterson, 1965; Miralda-Escude, 1998). At $z \gtrsim 6$, the declining strength of Lyα emission from galaxies has been used to infer the timing of reionization (e.g., Stark et al., 2010; Ouchi et al., 2010; Treu et al., 2012; Mesinger et al., 2015; Mason et al., 2018a; Morales et al., 2021; Bolan et al., 2022), complementary to measurements from the CMB electron scattering optical depth (Planck Collaboration et al., 2018) and the optical depth in the Lyα forest of quasars (e.g., Fan et al., 2006; McGreer et al., 2015; Lu et al., 2020; Qin et al., 2021).

However, there is a degeneracy between the strength of the damping wing absorption – due to the abundance of neutral hydrogen in the IGM – and the Lyα emission line profile emerging from the galaxy – set by scattering by neutral hydrogen within the interstellar and circumgalactic medium (ISM, CGM) (e.g., Neufeld, 1991). If a Lyα emission line emerges from a galaxy with its flux profile redshifted to $\gtrsim 300\ \mathrm{km\,s^{-1}}$ from the systemic velocity of the galaxy, these photons will experience a greatly reduced optical depth in the IGM and thus have high Lyα transmission, even in a highly neutral IGM (e.g., Dijkstra et al., 2011; Mason et al., 2018a; Mason & Gronke, 2020; Endsley et al., 2022b). Indeed, high rates of Lyα detection that have been reported in $z > 7.5$ luminous galaxies (Zitrin et al., 2015; Oesch et al., 2015; Roberts-Borsani et al., 2016; Stark et al., 2017) could be partially explained if substantial HI ISM reservoirs in these systems strongly scatter Lyα, and/or if strong outflows are more common in UV-bright galaxies, such that Lyα emerges from the galaxy at highly redshifted velocities (Mason et al., 2018b; Endsley et al., 2022b; Tang et al., 2023). Nonetheless, even if Lyα transmission is boosted by high velocity offsets, the resulting broadening of the profile is likely accompanied by a weakening of the line, reducing its detectability (Verhamme et al., 2018).

Until the advent of JWST, measurements of Lyα velocity offsets have only been possible for statistical samples at $z \lesssim 2$, where rest-frame optical emission is visible from the ground for Lyman-break galaxies (e.g., Erb et al., 2014; Steidel et al., 2014); for local analogs, strong line emitters at $z \sim 0.3-0.4$, with detailed HST/COS spectroscopy (e.g., Henry et al., 2015; Yang et al., 2017b; Hayes et al., 2023); and for smaller samples of UV-luminous sources with bright [CII] emission lines visible with ALMA (Willott et al., 2015; Pentericci et al., 2016; Inoue et al., 2016; Bradač et al., 2017; Cassata et al., 2020; Endsley et al., 2022b) or the highly ionized UV line CIII] (Stark et al., 2015, 2017), or in stacks of absorption line spectra of LAEs (Muzahid et al., 2020). Thus, reionization inferences have relied on extrapolating z < 2 samples to higher redshifts and direct measurements for only a handful of galaxies in the Epoch of Reionization (e.g., Mason et al., 2018a). JWST's near-IR spectroscopy opens the gates to accurate measurements of the Lyα velocity offset and its evolution with galaxy properties, which will allow us to break the degeneracy between ISM scattering and IGM opacity.

In this paper we present a first look at the Lyα velocity offsets, $\Delta v_{\mathrm{Ly}\alpha}$, of $z > 3$ UV-faint galaxies, made possible for the first time by JWST. We use JWST/NIRSpec (Jakobsen et al., 2022) spectra of rest-frame optical emission lines, obtained as part of the GLASS-JWST ERS program (Treu et al., 2022), to measure the Lyα velocity offsets of 12 $\mathrm{M_{UV}} \gtrsim -20$ galaxies at $z \sim 3-6$, with lower luminosity and at higher redshifts than previously possible. We explore empirical trends between $\Delta v_{\mathrm{Ly}\alpha}$ and other galaxy properties, to explore the physical mechanism behind $\Delta v_{\mathrm{Ly}\alpha}$, and we discuss our results in the context of Lyα observations during the Epoch of Reionization.

The paper is structured as follows. In Section 3.2 we describe the photometric and spectroscopic data for our study. In Section 3.3 we describe how we measure the Lyα velocity offsets for our sample and other relevant properties for the galaxies. We describe our results and comparison to the literature in Section 3.4. We discuss our results in Section 3.5 and state our conclusions in Section 4.7.

We assume a flat ΛCDM cosmology with $\Omega_m = 0.3,\ \Omega_\Lambda = 0.7,\ h = 0.7$, all magnitudes are in the AB system, and all distances are proper unless specified otherwise.

3.2 DATA

In this section we describe the data and sample selection used for our study. All observations are made in the lensing cluster Abell 2744.

3.2.1 VLT/MUSE SPECTROSCOPY

Lyα emitters (LAEs) at $2.9 < z < 6.7$ were selected from VLT/MUSE spectroscopy in Abell 2744 performed by the ESO program 094.A-0115 (Mahler et al., 2018; Richard et al., 2021). These data consist of four 1 sq. arcmin regions centered on the Abell 2744 cluster core. These quadrants have observing times of 3.5, 4, 4 and 5 hours respectively, with 2 extra hours of observation overlapping at the center of the cluster. The MUSE data have a median emission line flux 1σ uncertainty of 3.6×10^{-19} erg s^{-1} cm^{-2}, translating to an EW 5σ limit of $\sim$ 4 - 30 Å for a $\mathrm{M_{UV}} = -19$ galaxy at $z \sim 3-7$.

The MUSE program applied three complementary detection methods: (i) forced extraction in the location of $m_{\mathrm{AB}} \lesssim 30$ sources detected in Hubble Frontier Fields imaging (HST-GO/DD-13495 Lotz et al., 2017), using an extraction aperture corresponding to the `SExtractor` segmentation map convolved with the MUSE point spread function; (ii) detection of emission lines via narrow-band filtering of the MUSE cube; (iii) manual extractions of a field sources found through visual inspection, e.g. multiply-imaged systems. In the following, we will compare MUSE-selected Lyα -emitters (LAEs) to, mostly, Lyman-break selected samples. It is known that LAEs may be the extreme end of the Lyman break galaxy population (e.g., Dijkstra & Wyithe, 2012; Morales et al., 2021), undergoing very recent star formation, and are more likely to be low mass, less dusty and show lower Lyα velocity offsets than Lyman-break selected samples (e.g., Hashimoto et al., 2013; Shibuya et al., 2014).

In this study, we are most interested in understanding the expected properties of Lyα emission from Lyman-break selected galaxies at $z \gtrsim 6$, during the Epoch of reionization. At $z \sim 6$ a much larger fraction ($\sim 30-60\%$) of UV-faint galaxies are detected with high Lyα EW (> 25 Å, e.g., Stark et al., 2011; Cassata et al., 2015; De Barros et al., 2017; Fuller et al., 2020) than at $z \lesssim 3$ ($\sim 10\%$, e.g., Cassata et al., 2015). Furthermore, due to both an expected reduction in dust attenuation (as evidenced by steepinging UV slopes, β, e.g., Bouwens et al., 2014) and an increase in specific star formation rates (e.g., Stark et al., 2013; Endsley et al., 2022a) we should expect strong Lyα emission to be even more prevalent at $z > 6$. Therefore, we assume that the MUSE LAE sample is a suitable analog of UV-faint $z \gtrsim 6$ Lyman-break galaxies.

To test this assumption we compare with the sample of Fuller et al. (2020) who obtained deep Lyα spectroscopy of lensed UV-faint Lyman break galaxies at $z \sim 6$, with that of Richard et al. (2021, the origin catalog for our Lyα -selected galaxies). We select sources in the Fuller et al. (2020) catalog with $5.5 < z < 6.5$ (using photometric redshift for non-detections, where we only include sources with $P(5.5 < z_{\rm phot} < 6.5) > 0.6$ to minimize contamination by low-redshift interlopers) and $M_{\rm UV}$ in the same range as our sample. Non-detections for this subset of the Fuller et al. (2020) catalog have median upper limit EW$\lesssim 42$ Å. The Richard et al. (2021) sample has a slightly bluer UV slope by $\Delta\beta = 0.4$. This means that we are possibly studying a population slightly younger and/or less dust-attenuated than galaxies selected by their Lyman Break. However, we find that the Lyα EW distributions have similar medians, Lyα EW $= 36$ Å for our parent MUSE sample, and the Fuller et al. (2020) sample has median Lyα EW $= 42$ Å if all non-detections are treated as having Lyα EW uniformly distributed between 0 and their $\mathrm{EW}_{upperlim}$. Performing 10,000 iterations, and doing a Kolmogorov–Smirnov test of each, we find a median 80% chance that the underlying distributions are statistically the same. We conclude it is highly likely that the underlying EW distributions of our parent sample are representative of $5.5 < z < 6.5$ UV-faint LBG selected galaxies.

We further compare the Lyα EW of Richard et al. (2021) with all LBGs targeted by the GLASS-NIRSpec program between $3 < z_{\mathrm{phot}} < 7$. To form the sub-sample of LBGs, we perform a color criteria with their HST photometry (Bouwens et al., 2015, 2016b), this sample has a median z$\sim$4. We match the resulting 48 NIRSpec LBGs to Richard et al. (2021), obtain Lyα fluxes and compute their EWs. For 38 galaxies we find no Lyα counterpart, and use the 5σ flux limit of the MUSE observations. As in the previous paragraph, we treat upper-limits as a uniform distribution and iterate 10,000 times performing a Kolmogorov–Smirnov test between each distribution. Including the non-detections, we find it unlikely (p $<$ 5%) that the LBG selected sample has the same Lyα EW distribution as our MUSE LAE parent sample. In summary, we conclude that our parent sample (Richard et al., 2021) is likely biased towards high EWs compared to z$\sim$4 LBG selected galaxies, but that it is comparable to UV-faint LBG selected sources at the end of reionzation, z$\sim$6.

We note that it is possible that the Lyα fluxes reported by Richard et al. (2021) are underestimated, since they do not consider spatially extended Lyα emission of the galaxies for their Lyα extractions. Measurements including the spatially extended Lyα flux for MUSE LAEs with NIRSpec observations in the GLASS-ERS survey will be presented by Roy et al. (2023). In this we use the flux as reported by Richard et al. (2021) which we consider a more similar measurement to that obtained by slit spectrographs, which is how the majority of our comparison samples have been observed[*]

3.2.2 JWST NIRSpec spectroscopy

Near infrared spectroscopic data in Abell 2744 was obtained from the GLASS-JWST Early Release Science Program (PID 1324, Treu et al., 2022), observed on November 10, 2022. Three grating configurations were used, G140H/F100LP, G235H/F170LP and G395H/F290LP,

---

[*] We note that this assumption may not be valid if Lyα is significantly offset from the UV continuum, but recent work shows this is not likely to be the significant at the redshifts and magnitude range we are considering (Hoag et al., 2019a; Lemaux et al., 2021).

each with 4.9 hours exposure time. This allows observations spanning the wavelength range $0.81 - 5.14\,\mu$m. It is possible to observe Hα up to $z \sim 6.8$ and [OIII]5007 up to $z \sim 9.2$. The high-resolution, $R \sim 2700$ (corresponding to $\sigma \sim 50$ km s^{-1}), allows for precise measurements of spectral properties of the emission lines: most important for us is the line centroid and dispersion.

Details of the reduction process are given by Roberts-Borsani et al. (2022); Morishita et al. (2022). Briefly, we use the STScI JWST pipeline (ver.1.8.2)[†] for Level 1 data products, and the `msaexp`[‡] Python package for Level 2 and 3 data products. We extract the 1D spectrum following Morishita et al. (2022) and use the `msaexp` package to optimize our extraction using an inverse-variance weighted kernel following Mascia et al. (2023). The kernel is derived by summing the 2D spectrum along the dispersion axis and fitting the resulting signal along the spatial axis with a Gaussian profile ($\sigma \sim 0.4''$). This 2D kernel is then used to extract the 1D spectrum along the dispersion axis.

MUSE LAEs from the Mahler et al. (2018); Richard et al. (2021) catalog were included in the GLASS NIRSpec MSA. The MSA target selection is described by Treu et al. (2022) briefly, $z > 5$ and spectroscopically confirmed sources were prioritized. Therefore, the sample of MUSE LAEs observed is not guaranteed to be magnitude complete, but provides a qualitative comparison sample to UV-bright literature samples galaxies with measured velocity offsets.

A total of 17 MUSE LAEs were observed with NIRSpec in the GLASS-JWST ERS program. We detect rest-frame optical emission lines for 12 out of the 17 sources in the NIRSpec spectra, which we use for our work. From the remaining 5 sources we did not detect any optical emission lines (see also Mascia et al., 2023). The lack of detection is not surprising, the 5 sources are faint ($\mathrm{m}_{F150W} \sim 27.5$) and were selected from a single faint Lyα line detection. Properties of our sample are presented in Table 3.1.

We check if our 12 galaxy sub-sample of Richard et al. (2021) is representative of the complete sample. Following the methods in Section 3.2.1, we extend our statistical KS test to our 12 galaxy sub-sample and compare them to Richard et al. (2021). We find a ∼70% probability that the EW$_{\mathrm{Ly}\alpha}$ distributions of these two are the same. If we compare the 12 galaxy

---

[†] https://github.com/spacetelescope/jwst

[‡] https://github.com/gbrammer/msaexp

sample with Fuller et al. (2020) ($5.5 < z < 6.5$) and the LBGs targeted by GLASS-NIRSpec ($z \sim 4$), we arrive to the same conclusion of Section 3.2.1: Our 12 galaxy sample behaves similar to it's parent sample and is representative of UV-faint LBGs at the end of reionization.

3.2.3 PHOTOMETRIC CATALOGS

We use the photometric catalogs for Abell 2744 by Paris et al. (2023). The catalogs include HST/ACS and WFC3/IR from the *Hubble Frontier Fields* project (HST-GO/DD-13495 Lotz et al., 2017), photometric bands include: F435W, F606W, F814W, F105W, F125W, F140W, F160W. These catalogs also include JWST/NIRCam data from the UNCOVER collaboration (GO-2561, Bezanson et al., 2022): including photometry from the following 7 JWST/NIRCam filters: F115W, F150W, F200W, F277W, F356W, F410M and F444W. The catalogs by Paris et al. (2023) use F444W as the detection band but as we require the photometry to measure the UV-restframe continuum of our sources, we only use HST photometry in this work as our sample are all at $z < 6$.

3.2.4 GRAVITATIONAL LENSING MODELS

To account for the magnification caused by the strong lensing of Abell 2744 cluster, we use the lensing maps developed by Bergamini et al. (2022), which can be accessed in their online tool[§]. We do not find any galaxies near the critical curves, with all sources having magnifications between $\mu \sim 2 - 7$, with less than 10% uncertainties.

3.3 METHODS

In the following section we present our methods to retrieve the UV magnitude of our sample (Section 3.3.1), Lyα equivalent widths and velocity offsets $\Delta v_{\mathrm{Ly}\alpha}$, and the dispersion of optical emission lines (Section 3.3.2). All resulting values are shown in Table 3.1.

[§] http://bazinga.fe.infn.it:5007/SLOT

3.3.1 MEASURING M_{UV}

To measure M_{UV} (absolute magnitude at 1500Å) and β slope we fit a power-law model $f \propto \lambda^{\beta}$ to the photometry (e.g., Rogers et al., 2013). We use all the photometric bands that have their response cutoffs in the UV continuum between 1216 Å and 3000 Å. We fit the model using Markov Chain Monte Carlo with `emcee` (Foreman-Mackey et al., 2013). Flat priors are used: $-25 < M_{UV} < -12$ and $-4 < \beta < 1$, which covers the expected ranges (e.g., Bouwens et al., 2014). We correct the UV magnitudes for gravitational lensing magnification using the lens model by Bergamini et al. (2022). We take M_{UV} , β and the corresponding 1-σ errors from the resulting posterior distributions of the fitted power-laws.

Three sources were not detected in the Paris et al. (2023) catalogs, due to their extremely low continuum flux. In these cases we perform a forced photometry in the coordinates expected by Lyα (MUSE) observations, with a circular aperture of 0.28" corresponding to the 2 FWHM aperture of the F444W point spread function. One of these galaxies was (ID: 80085) was detected in the forced extraction, but not detected in the Paris et al. (2023) catalogs as it is close to a non-deblended source. We report the other two galaxies (IDs : 70017 and 70022) M_{UV} measurements as 5σ upper-limits in Table 3.1.

The median M_{UV} and 1σ scatter of our sample, corrected for magnification, is -17.8 ± 1.4.

3.3.2 LYα EW AND VELOCITY OFFSETS

To measure the Lyα equivalent width (EW) of these 12 galaxies we use the Lyα fluxes reported in the public catalogs by Richard et al. (2021), and the continuum flux density as inferred from the HST photometry described in Section 3.2.3. We use the posteriors of M_{UV} and β obtained in Section 3.2.3 to infer the posterior distribution of flux densities at 1250 Å. The median EW and 1σ scatter of our sample is 34 ± 21 Å.

We measure Lyα velocity offsets as follows: $\Delta v_{\mathrm{Ly}\alpha} = \mathrm{c} \left(\frac{z_{\mathrm{Ly}\alpha} - z_{\mathrm{sys}}}{1+z_{\mathrm{sys}}} \right) where z_{\mathrm{sys}}$ is the systemic redshift measured from rest-frame optical emission lines with NIRSpec and $z_{\mathrm{Ly}\alpha}$ is the redshift measured from Lyα , corrected to vacuum wavelength, as reported in the MUSE catalog (Richard et al., 2021). For Lyα , the redshift is measured at the peak of the red peak, if the line is double-peaked (J. Richard, private communication).

For sources at $z < 6.5$ we use Hα and [OIII]5007 emission in NIRSpec to measure velocity offsets. For sources at $6.5 < z < 6.7$ only [OIII]5007 is visible, due to the wavelength coverage. We measure the redshift of Hα and [OIII]5007 by performing a Gaussian profile fit using a Markov Chain Monte Carlo sampling with `emcee` (Foreman-Mackey et al., 2013), and recovering the posterior distribution of the central wavelength of the lines and the velocity dispersion ($\sigma_{\rm opt}$) of the line profile. We repeat this process separately for Hα and [OIII]5007, and take $\sigma_{\rm opt}$ as the average. We include any redshift difference between the lines in the $\Delta v_{\rm Ly\alpha}$ error. We propagate the errors in the central wavelength of the optical lines, and the Lyα central wavelength measured by Richard et al. (2021) for our measurement of $\Delta v_{\rm Ly\alpha}$. Uncertainties in all cases are dominated by the precision of MUSE/VLT measurements of the Lyα centroid, especially in low signal-to-noise sources. The precision of systemic redshifts obtained from optical emission lines (JWST/NIRSpec) is extremely high, with errors $\sim 1 - 8$ km s^{-1} .

Discrepancies between ground-based and JWST/NIRSpec redshifts of the same observed emission lines at $> 1\,\mu$m have been reported (Tang et al., 2023; Larson et al., 2023). This is likely due to the ubiquity of atmospheric skylines in ground-based spectra in the near-IR, which introduce considerable uncertainty in line centroid measurements, though there may also be uncertainties in the wavelength calibration. To verify the consistency of the MUSE and NIRSpec wavelength calibrations we check three galaxies in the Abell 2744 field where it is possible to compare the redshifts measured from nebular lines which trace systemic both with MUSE and NIRSpec. For the systemic redshifts we use: CIII]1909 detections for MUSE (Richard et al., 2021), and Hα and/or [OIII] for NIRSpec. We find a negligible difference in redshifts between the two instruments, with a median offset of ~30 km s^{-1} , which is well within the uncertainties of our $\Delta v_{\rm Ly\alpha}$ measurements, and below the instrumental resolution. We also find one galaxy observed by GLASS-ERS which had a previous systemic redshift measurement from VLT/KMOS from the [OII]3726-3729 doublet (Mason et al., 2017) and find similarly good agreement. Therefore, it is unlikely that any systematic differences between redshift measured from space and ground-based telescope biases our results.

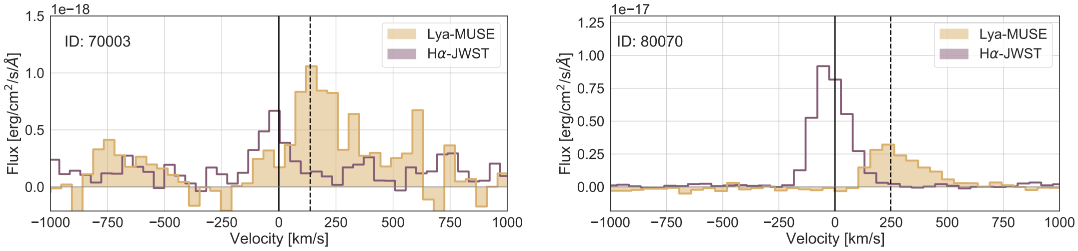

Figure 3.1: Example spectra from this sample, with the velocity axis centered at the systemic redshift given by Hα. We show galaxies 70003 and 80070, which have low and high $\Delta v_{\mathrm{Ly}\alpha}$ respectively. Spectra from JWST/NIRSpec Hα (purple) and VLT/MUSE Lyα (yellow). Vertical lines mark the Hα (solid) and Lyα (dashed) peaks.

3.4 Results

In the following section we present our results and look for evidence of trends that can explain the mechanisms behind the shift of Lyα emission from the systemic redshift. As described above, our sample is not magnitude-complete so our comparison to the literature is qualitative and the sample-selection is different from literature samples which are Lyman-break galaxy selected (and we expect LAEs to be typically lower mass and less dusty than Lyman-break galaxies, e.g., Kornei et al., 2010; Shibuya et al., 2014). Nevertheless, we find our sample is representative of z∼6 UV-faint LBGs, of interest during reionization. Our sample allows us to quantify Lyα velocity offsets in UV-faint galaxies for the first time, and investigate the trends by comparing with UV-bright galaxies from the literature.

Our measured Lyα velocity offsets, velocity dispersion, rest frame EW Lyα , and other observed quantities are presented in Table 3.1. In Figure 3.1 we show examples of the spectra observed with JWST/NIRSpec and legacy spectra from VLT/MUSE extracted by Roy et al. (2023).

3.4.1 $\Delta v_{\mathrm{Ly}\alpha}$ AND UV MAGNITUDE

In Figure 3.2 we show our measured Lyα velocity offsets versus the UV magnitude of the sample, as well as previous measurements from the literature: $z \sim 2-3$ (Erb et al., 2014; Steidel et al., 2014); $4 < z < 7.5$ (Stark et al., 2015; Willott et al., 2015; Bradač et al., 2017; Inoue et al., 2016; Mainali et al., 2018; Pentericci et al., 2016; Stark et al., 2017; Endsley et al., 2022b;

Table 3.1: Lyα and rest-optical properties of $z \sim 3 - 6$ galaxies in GLASS-ERS used in this work.

ID	R.A.	Dec.	$z_{\rm sys}$	$z_{\rm Ly\alpha}$*	μ	$\rm M_{UV}$ *	β	Lyα EW [Å] *	$\Delta v_{\rm Ly\alpha}$ [km/s]	$\sigma_{\rm opt}$ [km/s]
90155	3.60687	-30.38557	2.9402	2.9430	1.9 ± 0.1	-16.6 ± 0.1	-2.2 ± 0.2	59 ± 12	207 ± 83	< 44
80053	3.57497	-30.39678	3.1287	3.1327	3.7 ± 0.1	-19.2 ± 0.1	-2.2 ± 0.1	11 ± 1	287 ± 11	51 ± 3
80113	3.60465	-30.39223	3.4724	3.4782	2.0 ± 0.1	-17.6 ± 0.1	-2.0 ± 0.1	26 ± 5	390 ± 142	< 42
80027	3.56929	-30.40963	3.5796	3.5831	2.0 ± 0.1	-19.4 ± 0.1	-2.4 ± 0.1	7 ± 1	235 ± 38	47 ± 0
80029	3.60318	-30.41571	3.9509	3.9540	2.8 ± 0.1	-18.9 ± 0.1	-2.0 ± 0.1	7 ± 1	192 ± 78	48 ± 1
80013	3.56934	-30.40873	4.0428	4.0454	2.0 ± 0.1	-18.3 ± 0.1	-2.3 ± 0.1	47 ± 5	162 ± 19	50 ± 3
80085	3.57435	-30.41253	4.7246	4.7290	2.1 ± 0.1	-15.4 ± 0.4	-2.5 ± 1.0	85 ± 11	230 ± 56	35 ± 2
80070	3.58232	-30.38765	4.7968	4.8016	5.3 ± 0.2	-18.1 ± 0.1	-1.8 ± 0.1	43 ± 3	245 ± 9	58 ± 1
70017	3.60666	-30.39328	5.1864	5.1892	2.0 ± 0.1	< -16.2	–	> 25	132 ± 105	< 30
70018	3.58790	-30.41159	5.2824	5.2843	6.8 ± 0.2	-18.2 ± 0.1	-2.2 ± 0.1	8 ± 1	83 ± 42	23 ± 4
70022	3.57113	-30.39295	5.4292	5.4335	3.5 ± 0.1	< -15.7	–	> 21	199 ± 150	< 41
70003	3.57585	-30.38929	5.6180	5.6210	4.6 ± 0.1	-16.3 ± 0.2	-3.7 ± 1.2	104 ± 19	144 ± 25	40 ± 10

*For non-detections, 5σ upperlimits are shown.

Cassata et al., 2020); $z > 7.5$ (Stark et al., 2017; Tang et al., 2023). Thanks to gravitational lensing and the sensitivity and wavelength coverage of JWST/NIRSpec to detect rest-frame optical lines, we are able to reach much fainter UV magnitudes than in previous works, down to $\rm M_{UV} \sim -16$. The median $\rm M_{UV}$ with 1σ scatter of our sample is -17.8 ± 1.4 and $\Delta v_{\rm Ly\alpha}$ of 205 ± 75 $\rm km\,s^{-1}$. This is consistent with the median $\Delta v_{\rm Ly\alpha}$ measured for a stack of $z \approx 3.3$ LAEs from the MUSEQuBES survey (their median $\Delta v_{\rm Ly\alpha} = 171 \pm 8$ $\rm km\,s^{-1}$ Muzahid et al., 2020).

The left panel of Figure 3.2 shows a clear trend of increasing $\Delta v_{\rm Ly\alpha}$ with increasing luminosity. Our new results push these measurements to the UV-faint and low $\Delta v_{\rm Ly\alpha}$ end, demonstrating the trend seen from the literature at brighter luminosities extends to lower luminosities. We compare our observations with the semi-empirical model by Mason et al. (2018a), which assumes an underlying relation between Lyα velocity offsets and halo mass which is independent of redshift. This assumes Lyα scattering is predominantly determined by the total mass of the galaxy, which in turn is assumed to be proportional to the column density of neutral hydrogen, which is predicted to be key factor in shaping Lyα line profiles (e.g., Neufeld, 1990; Verhamme et al., 2006, 2008; Gronke et al., 2016; Kakiichi & Gronke, 2021). In this model, redshift evolution of $\Delta v_{\mathrm{Ly}\alpha}$ arises only from the predicted evolution in the UV luminosity – halo mass relation, whereby galaxies with fixed halo mass are brighter at higher redshifts, due to increased mass accretion rates (e.g., Mason et al., 2015).

In the right panel of Figure 3.2 we map our measured UV magnitudes to an inferred halo mass, M_h, using the UV luminosity – halo mass model by Mason et al. (2015) to compare with the redshift-independent $\Delta v_{\mathrm{Ly}\alpha}(M_h)$ model by Mason et al. (2018a). When transforming to halo mass we see a similar trend as with $\mathrm{M_{UV}}$, with less massive galaxies having lower Lyα offsets, and that our new results are consistent with the model, suggesting there is not strong evolution of $\Delta v_{\mathrm{Ly}\alpha}(M_h)$ with redshift. While our new data follows the model trend, our sample appears to have slightly higher velocity offsets than predicted at faint UV luminosities, which we discuss further in Section 3.5.1.

We see reasonable agreement with the models for galaxies between $6 < z < 7.5$ from the literature. Galaxies with $z > 7.5$ (Stark et al., 2017; Tang et al., 2023; Bunker et al., 2023) have much higher Lyα offsets than those expected for galaxies given their $\mathrm{M_{UV}}$ or halo mass, indicating a possible bias towards detecting high Lyα offsets during the epoch of reionization, which we will discuss in Section 3.5.2.

3.4.2 $\Delta v_{\mathrm{Ly}\alpha}$ AND NEBULAR LINE VELOCITY DISPERSION

The emerging Lyα line profile is expected to be shaped by both the column density (N_{HI}) and the kinematics of neutral gas close to line center (e.g., Verhamme et al., 2006, 2008; Hashimoto et al., 2015; Henry et al., 2015; Kakiichi & Gronke, 2021; Hayes et al., 2023). As Lyα and Hα likely are produced in the same HII regions, we therefore expect the Lyα profile may be linked to the kinematics of the gas as traced by Hα (e.g. see Hayes et al., 2023, who find the correlation between optical line dispersion and $\Delta v_{\mathrm{Ly}\alpha}$ is primarily driven by the correlation of both those properties with mass). We follow Erb et al. (2014) and examine the correlation between $\Delta v_{\mathrm{Ly}\alpha}$ and the velocity dispersion of optical lines, as measured by rest-frame optical emission lines. We report the intrinsic dispersion, corrected for the instrumen-

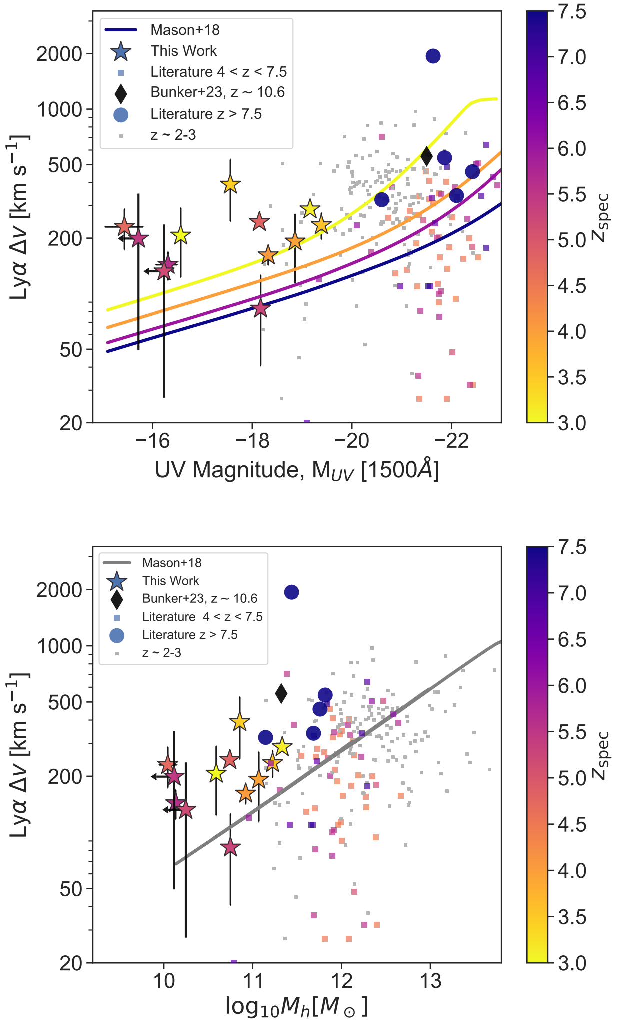

Figure 3.2: Lyα velocity offset versus UV magnitude and implied halo mass, using the mapping derived in the UV luminosity function model by Mason et al. (2015), color-coded by redshift. Our new sample is shown as colored stars. For comparison, we show values from the literature at $z \sim 2-3$ (Erb et al., 2014; Steidel et al., 2014, gray squares), at $4 < z < 7.5$ (Stark et al., 2015; Willott et al., 2015; Bradač et al., 2017; Inoue et al., 2016; Mainali et al., 2018; Pentericci et al., 2016; Stark et al., 2017; Endsley et al., 2022b; Cassata et al., 2020, colored squares), at $z > 7.5$ (Tang et al., 2023, blue circles), and GN-z11 (Bunker et al., 2023, black diamond). We also show the model by Mason et al. (2018a) which was derived from the $z \sim 2$ literature samples. The new GLASS-ERS sample extends this measurement to galaxies ~ 2 mag fainter than previously possible. $\Delta v_{\mathrm{Ly}\alpha}$ error bars are dominated by the uncertainty of the centroid in MUSE Lyα emission observations.

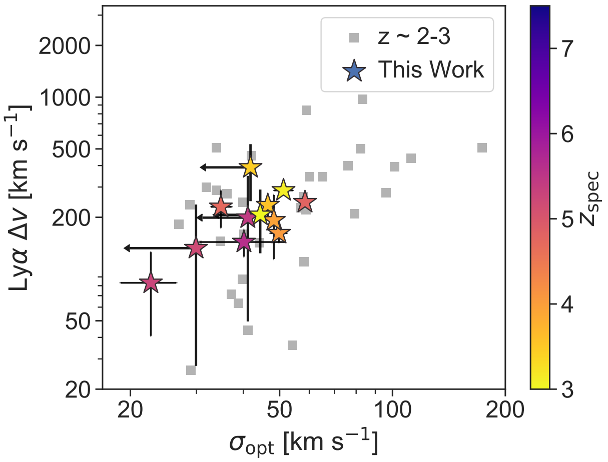

Figure 3.3: $\Delta v_{\mathrm{Ly}\alpha}$ vs velocity dispersion of the optical lines. We present our data as stars color-coded by redshift. In gray squares are $z \sim 2-3$ sources from Erb et al. (2014). We show upperlimits for measurements below $\sigma_{res} = 47$ km s^{-1} . Uncertainties are dominated by MUSE Lyα centroid measurements. Both samples suggest a correlation between optical line velocity dispersion and $\Delta v_{\mathrm{Ly}\alpha}$.

tal broadening due to the resolution of our NIRSpec data, as $\sigma_{\mathrm{opt,intr}} = \sqrt{\sigma^2_{\mathrm{obs}} - \sigma^2_{\mathrm{res}}}$, with $\sigma_{\mathrm{res}} \approx 47$ km s^{-1} .

In Figure 3.3 we plot $\Delta v_{\mathrm{Ly}\alpha}$ and σ_{opt} for our sample and compare with the Erb et al. (2014) sample. The majority of our sample have very low intrinsic velocity dispersion, $\lesssim 50$ km s^{-1} , implying low dynamical masses. The literature sample shows a positive correlation between $\Delta v_{\mathrm{Ly}\alpha}$ and σ_{opt} and our new sample extends it to higher redshift, showing no strong evolution.

3.4.3 $\Delta v_{\mathrm{Ly}\alpha}$ AND EQUIVALENT WIDTH

Previous works have found an anti-correlation between $\Delta v_{\mathrm{Ly}\alpha}$ and the Lyα EW (e.g., Erb et al., 2014; Tang et al., 2021). Both of these quantities are correlated with the neutral gas column density and scattering events (Verhamme et al., 2006, 2008; Yang et al., 2017a). Higher N_{HI}, or a high covering fraction of neutral gas, makes it less likely for a Lyα photon to escape at its central wavelength, increasing $\Delta v_{\mathrm{Ly}\alpha}$, and can also imply higher dust content (Santini et al., 2014) – decreasing Lyα EW (Charlot & Fall, 1993).

In Figure 3.4 we can see these effects for sources in the literature: $z \sim 2-3$ (Erb et al., 2014; Steidel et al., 2014), $3 < z < 7.5$ (Stark et al., 2015; Willott et al., 2015; Bradač et al., 2017; Inoue et al., 2016; Mainali et al., 2018; Pentericci et al., 2016; Stark et al., 2017; Endsley et al., 2022b; Cassata et al., 2020; Tang et al., 2021), $z > 7.5$ (Stark et al., 2017; Tang et al., 2023) where galaxies with low EW Lyα more commonly have high Lyα offsets. In general we find our sources lie in the same region as the literature. However, the bulk of galaxies in our sample have $\Delta v_{\mathrm{Ly}\alpha} < 300$ km s^{-1}, considerably lower than many sources in the literature. This is not surprising, since our sample only covers a small and less massive range of halo masses, where high $\Delta v_{\mathrm{Ly}\alpha}$ is less common. For Lyα EW < 20Å all of our sample have Lyα velocity offsets below 300 km s^{-1}, lower than the sources in the high-redshift literature (z> 7.5).

One source, 70018, has both low Lyα EW$= 8 \pm 2$ Åand low $\Delta v_{\mathrm{Ly}\alpha} = 88 \pm 42$, which is rare compared to the literature and physically unexpected, albeit the $\Delta v_{\mathrm{Ly}\alpha}$ error is high, and the source is only ∼2.5σ away from galaxies at similar EW. We find that the galaxy is formed of two clumps in UV and optical continuum, but only the main clump has Hα and Lyα emissions, likely indicating a younger stellar population. Low Lyα EW and velocity offsets can be explained by dust absorption (Laursen et al., 2009). However, the galaxy does not appear to be particularly reddened (β=-2.1) and Roy et al. (2023) measures a low Balmer decrement Hα /H_β=2.89. Nevertheless, Roy et al. (2023) measures a low Lyα escape fraction of 3% implying significant Lyα absorption in the ISM. The lack of emission lines in the second clump is not enough to result in low EW due to it being fainter in the UV than the emitting clump. We find no evidence of a strong magnification gradient in the galaxy when using the lens models from (Bergamini et al., 2022), which could cause differential magnification and strongly effect Lyα flux measurements.

3.5 Discussion

The results described in Section 3.4 provide a qualitative framework for understanding the transmission of Lyα through the ISM and through the reionizing IGM. We discuss the phys-

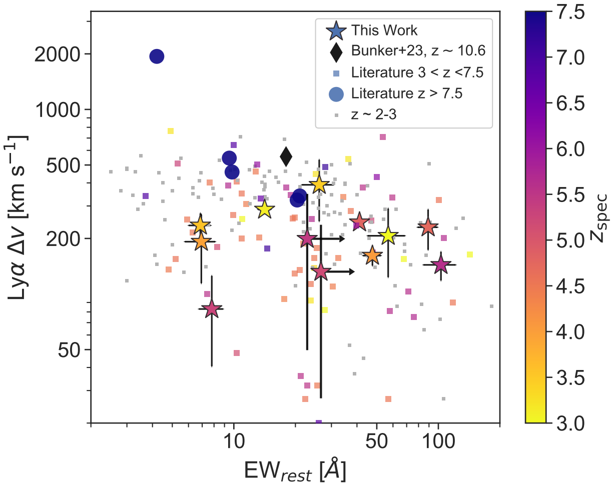

Figure 3.4: $\Delta v_{\mathrm{Ly}\alpha}$ against rest-frame equivalent width of Lyα . Our data is shown as stars color-coded by redshift. We present values from the literature at $z \sim 2-3$ (Erb et al., 2014; Steidel et al., 2014, gray squares), at $3 < z < 7.5$ (Stark et al., 2015; Willott et al., 2015; Bradač et al., 2017; Inoue et al., 2016; Mainali et al., 2018; Pentericci et al., 2016; Stark et al., 2017; Endsley et al., 2022b; Cassata et al., 2020; Tang et al., 2021, colored squares), $z > 7.5$ (Stark et al., 2017; Tang et al., 2023, blue circles), and GN-z11 (Bunker et al., 2023, black diamond). Both the literature data and our sample show low $\Delta v_{\mathrm{Ly}\alpha}$ at higher EW.

ical picture of Lyα scattering in the ISM emerging from our results in Section 3.5.1 and the implications of our results for Lyα visibility from UV faint galaxies in the Epoch of Reionization in Section 3.5.2.

3.5.1 PHYSICAL DRIVERS OF LYα VELOCITY OFFSETS

The shift of Lyα photons to wavelengths redward and/or blueward of central wavelength is due to resonant scattering with neutral hydrogen in the ISM and absorption by dust (e.g., Neufeld, 1991; Verhamme et al., 2006). The amplitude of the velocity shift will be linked to the number of scattering events: set by the column density of neutral gas, $N_{\rm HI}$ (e.g., Neufeld, 1990; Verhamme et al., 2006; Hashimoto et al., 2015; Henry et al., 2015; Kakiichi & Gronke, 2021), and its covering fraction (e.g., Shibuya et al., 2014; Jaskot et al., 2019) and the velocity of HI gas and any outflows (e.g., Pettini et al., 2001; Shapley et al., 2003).

In Figure 3.2 we demonstrate data at a range of redshifts imply a correlation between $\Delta v_{\rm Ly\alpha}$ and UV luminosity, and therefore halo mass. This correlation is likely due to both to higher $\rm N_{HI}$ in more massive galaxies and increased velocity of HI gas in the ISM and higher outflow velocities (e.g., Heckman et al., 2015; Xu et al., 2022). We also find that several of our UV-faint galaxies show double-peaked Lyα , implying a line of sight with lower $\rm N_{HI}$ and thus may be Lyman continuum leaker candidates (Roy et al., 2023).

While our results demonstrate a decrease in Lyα velocity offset with decreasing UV luminosity our results appear to lie above the Mason et al. (2018a) model predictions, especially at the lowest $\rm M_{UV}$. We note that the model is semi-empirical and was made using observations of $z \sim 2$ galaxies brighter than $\rm M_{UV} \sim$-19, thus the model lines fainter than this point in Figure 3.2 are an extrapolation both in redshift and UV luminosity (we also note the model predicts a large intrinsic scatter in $\Delta v_{\rm Ly\alpha}$ – see Figure 2 by Mason et al. 2018a). Below we discuss a couple of physical factors which could cause our $z \sim 3-6$ sample to have higher velocity offsets than the model predictions.

It is possible that our $z \sim 3-5.6$ sample is biased towards higher $\Delta v_{\rm Ly\alpha}$, compared to the

$z \sim 2$ samples the model is based on, due to the increasing Gunn & Peterson (1965) optical depth in the IGM with increasing redshift (e.g., Faucher-Giguère et al., 2008; Becker et al., 2015). In particular, the infall of dense gas around dark matter halos may lower the transmission of Lyα emitted redward of systemic, as red photons are blue-shifted into the Lyα resonant frequency in the frame of the infalling gas (e.g., Santos, 2004; Dijkstra et al., 2007; Laursen et al., 2011). We test the expected impact of this scenario by using Lyα transmission curves extracted from the *IllustrisTNG-100* simulations (Nelson et al., 2019) by Byrohl et al. (2019). We use 5000 randomly selected mass halos and lines-of-sight. At z$\sim$5 we find Lyα transmission rises above 30% at a median $\Delta v_{\mathrm{Ly}\alpha}$ of 90 km s^{-1} (with a standard deviation of 50 km s^{-1}), making detections of Lyα with velocity offset lower than this rare. By contrast, at z$\sim$2, where the model by Mason et al. (2018a) was calibrated, the median $\Delta v_{\mathrm{Ly}\alpha}$ where $>$ 30% Lyα is transmitted decreases to 60 km s^{-1} , making it easier to detect low $\Delta v_{\mathrm{Ly}\alpha}$. The impact of resonant absorption in the IGM could be tested by seeing how both the velocity offset and spectral shape of Lyα evolves with redshift, as resonant absorption due to infalling will cause a sharp cut-off on the 'blue side' of a Lyα line redward of systemic (e.g., Park et al., 2021).

Observing higher $\Delta v_{\mathrm{Ly}\alpha}$ than the models could also be achieved with an increasing presence of outflows with increasing redshift, for example due to increased star formation rates at fixed UV luminosity with increasing redshift. Lyα photons scatter in outflowing gas, making it preferentially easier to detect photons which are 'backscattered' on the far side of the source to the observer. These photons are Doppler shifted to a velocity offset $\sim 2\times$ the outflow velocity and thus the photons fall out of resonance and transmit through the gas more easily, making redshifted Lyα line profiles ubiquitous in galaxies with strong outflows (e.g., Shapley et al., 2003; Verhamme et al., 2006; Erb et al., 2014). The incidence and velocity of outflows at $z > 2$ can now be measured more easily with JWST (see e.g., Carniani et al., 2023).

In Figure 3.3, we see a correlation between $\Delta v_{\mathrm{Ly}\alpha}$ and the velocity dispersion of optical lines, finding that our sample of galaxies with low $\Delta v_{\mathrm{Ly}\alpha}$ also have low optical line velocity dispersion. This suggests that Lyα scattering is correlated to the velocity dispersion of gas close to the line center, as suggested by Erb et al. (2014). Since the nebular emission lines we observed, Hα and [OIII], are produced in the same HII regions around massive stars as Lyα , and are not affected by resonant scattering, but broadened by the velocity distribution of the ionized gas, their line profiles should contain information about the velocity dispersion of the HII regions. At the same time, $\Delta v_{\mathrm{Ly}\alpha}$ and Lyα broadening is produced by a combination of the column density and kinematics of HI (resonant scattering). All of the aforementioned processes are correlated to galaxy mass, shown in the analysis by Hayes et al. (2023) for $z \sim 0 - 0.4$ LAEs, finding that the correlation of optical line dispersion with $\Delta v_{\mathrm{Ly}\alpha}$ is mostly driven by the correlation of both quantities with mass. This is consistent with the picture proposed by Henry et al. (2015) that HI column density dominates Lyα escape in low mass galaxies.

3.5.2 IMPLICATIONS FOR LYα OBSERVATIONS IN THE EPOCH OF REIONIZATION

One of the main results we can conclude from Figure 3.2, is that UV-faint galaxies ($M_{\mathrm{UV}} < -20$) at $z \sim 3 - 6$ tend to have low $\Delta v_{\mathrm{Ly}\alpha}$ ($\lesssim 300$ km s^{-1}). As the galaxy population shifts to faint luminosities at high redshift (e.g., Bouwens et al., 2021) we expect that a large fraction of galaxies at $z \gtrsim 6$ may be UV-faint galaxies with emitting Lyα with low velocity offsets and intrinsically high Lyα EW ($\gtrsim 25$ Åe.g., Stark et al., 2011; Cassata et al., 2015; De Barros et al., 2017; Fuller et al., 2020). When the IGM was still significantly neutral, as during and before the epoch of reionization ($z \sim 6 - 10$, e.g., Mason et al., 2019), we expect the Lyα damping wing to strongly or completely attenuate Lyα photons that escape the galaxies near their central wavelength (e.g., Dijkstra et al., 2011; Mason & Gronke, 2020).

In this case it would be possible for Lyα to propagate through the IGM to the observer only if it has high enough $\Delta v_{\mathrm{Ly}\alpha}$ such that the photons do not experience the strong damping wing. Assuming that the line is not broadened and weakened out of the detection limit of the observations, this should then produce a bias, where we will be more likely to see galaxies with very high $\Delta v_{\mathrm{Ly}\alpha}$ ($\gtrsim 500$ km s^{-1}) during the epoch of reionization, even if such sources are less common in the population. We can see hints of this in the results of Stark et al. (2017); Tang et al. (2023): they report Lyα emission from UV-bright ($M_{\mathrm{UV}} \lesssim -21$) galaxies at $z > 7.5$, well within the epoch of reionization. All of these galaxies have $\Delta v_{\mathrm{Ly}\alpha} > 300$ km s^{-1}, higher than most of our sample, and higher than the predictions by Mason et al. (2018a). The results from Bunker et al. (2023) show that this trend continues at higher redshift in a detected Lyα galaxy at z ∼10.6, with $\Delta v_{\rm Ly\alpha}$ = 555 km s^{-1} .

This is in contrast to the low detection rates of Lyα in UV-faint galaxies at $z \gtrsim 7$ (Hoag et al., 2019b; Mason et al., 2019), including the case of A2744-z7p9OD, a $z = 7.88$ spectroscopically confirmed overdensity where none of the seven UV-faint ($\rm M_{UV} > -20$) galaxies in a 60 proper kpc radius have observed Lyα emission $> 16 - 28$ Å (Morishita et al., 2022). Our results imply that the low Lyα velocity offsets in UV-faint galaxies likely contribute to the preferential attenuation of Lyα from these galaxies during reionization, in addition to these galaxies likely tracing less overdense and late reionized regions of the IGM compared to UV bright galaxies (Mason et al., 2018b; Lu et al., 2023).

The detection of Lyα with low $\Delta v_{\rm Ly\alpha}$ in reionization epoch galaxies can be an important indicator of the presence and size of large ionized bubbles: Lyα emitted from galaxies inside large ionized bubbles does not need to have have been scattered far from its central wavelength in order to transmit through the IGM. In Figure 3.5 we illustrate this by showing the fraction of Lyα flux transmitted through the IGM, assuming a single ionized bubble in a neutral IGM, following Mason & Gronke (2020), as a function of ionized bubble size and emitted $\Delta v_{\rm Ly\alpha}$. Here we make mock Lyα emission lines with FWHM $= \Delta v_{\rm Ly\alpha}$ (Verhamme et al., 2015; Mason et al., 2018a, fixing FWHM $= 50$ km s^{-1} for lines with $\Delta v_{\rm Ly\alpha} < 50$ km s^{-1}) and calculate the transmission fraction as the ratio of total observed flux to total emitted flux. This shows that the detection of Lyα at $\lesssim 200$ km s^{-1} with high Lyα escape fraction, implying significant transmitted flux close to line center, provides strong evidence of $\gtrsim 1$ pMpc ionized bubbles (see Saxena et al., 2023, for a recent candidate), but that Lyα with $\Delta v_{\rm Ly\alpha} \gtrsim 400$ km s^{-1} can still transmit $\gtrsim 10\%$ flux through the IGM even if the source is inside a very small ionized bubble (or even in a fully neutral IGM, see also, Dijkstra et al., 2011; Mason & Gronke, 2020; Endsley et al., 2022b). UV-faint galaxies around UV-bright Lyα-emitting galaxies are thus ideal targets for deep spectroscopic follow-up to confirm and estimate the size of ionized bubbles, as they have high number densities and are likely to emit their Lyα at low velocity offset from systemic. In the case where we detect no Lyα from the surrounding faint galaxies then the reionization bubble is likely not sufficiently large to allow

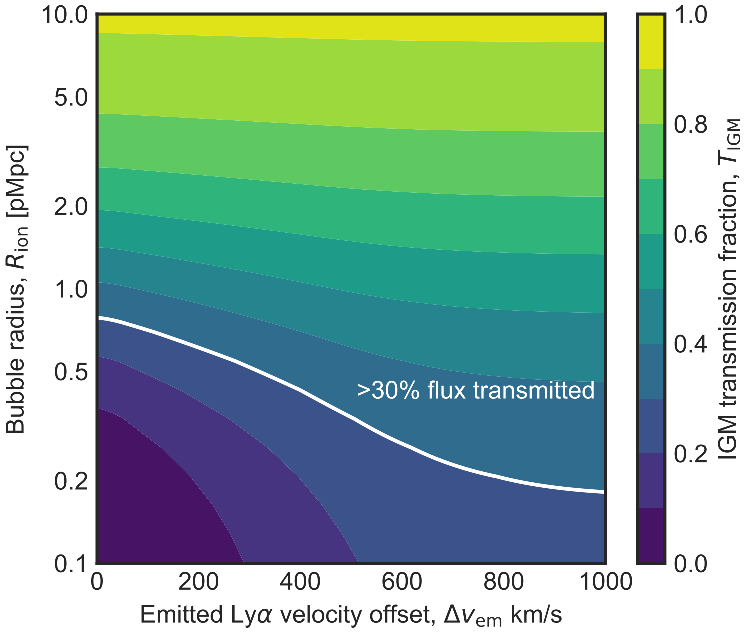

Figure 3.5: Fraction of Lyα flux transmitted through the IGM as a function of the radius of ionized bubble and emitted $\Delta v_{\mathrm{Ly}\alpha}$, color coded by transmission through the IGM. We show the contour of 30% transmission as a white curve. The IGM transmission values are calculated assuming a Lyα emitting galaxy is in the center of a single ionized bubble in a neutral IGM, as described in Section 3.5.2. This figure shows that Lyα emission lines with $\Delta v_{\mathrm{Ly}\alpha} \lesssim 200$ km s^{-1} must reside at least $\gtrsim 1$ proper Mpc from the neutral IGM in order to transmit a significant fraction of their flux through the IGM.

Lyα transmission close to the line center.

Furthermore, it may prove useful to use the properties of optical emission lines, such as the correlation between $\Delta v_{\mathrm{Ly}\alpha}$ and σ_{opt} to estimate the *emitted* Lyα line profile (before attenuation in the IGM) and thus infer the attenuation of Lyα during the epoch of reionization. While we observe a large scatter in the correlation between $\Delta v_{\mathrm{Ly}\alpha}$ and σ_{opt}, JWST enables optical line spectroscopy for large samples of $z \sim 3-6$ LAEs and thus opens the door to finding good estimators of emitted Lyα line profiles (e.g. Hayes et al., 2023).

3.6 Conclusions

We have measured the velocity offset of Lyα emission from systemic in 12 galaxies at $z \sim 3-6$, as well as the velocity dispersion of their optical emission lines, Hα and [OIII]5007. Thanks to JWST and the lensed cluster Abell 2744, we were able to measure $\Delta v_{\mathrm{Ly}\alpha}$ in at UV magnitudes not previously possible ($-19 \lesssim \mathrm{M_{UV}} \lesssim -16$). Our conclusions are as follows:

1. Our sample has a median $\mathrm{M_{UV}}$ of -17.8 ± 1.4 and we find a median and 1σ dispersion $\Delta v_{\mathrm{Ly}\alpha} = 205 \pm 75$ km s^{-1} . Combined with observations from previous work targeting more luminous galaxies we find a positive correlation between UV luminosity and $\Delta v_{\mathrm{Ly}\alpha}$, consistent with a theoretical model where $\Delta v_{\mathrm{Ly}\alpha}$ depends on halo mass.
2. We observe that our sample follows the previously reported correlation between $\Delta v_{\mathrm{Ly}\alpha}$ and the velocity dispersion of optical lines, though with a large scatter. With upcoming large samples with JWST, properties of optical emission lines could prove to be a useful predictor of Lyα line properties during the epoch of reionization.
3. We find agreement with the literature when comparing $\Delta v_{\mathrm{Ly}\alpha}$ and Lyα EW, with the majority of sources falling on a trend of increasing EW with decreasing $\Delta v_{\mathrm{Ly}\alpha}$.
4. Our results are consistent with, and extend towards fainter magnitudes, the framework explored by previous studies that Lyα velocity offsets are driven by the abundance and velocity of neutral hydrogen close to the HII regions where Lyα is produced. Our results are thus consistent with the assumption that Lyα emission from UV-faint galaxies

during the Epoch of Reionization may be preferentially attenuated compared to that from UV-bright galaxies because of the strong damping wing optical depth close to line center produced by intergalactic neutral hydrogen.

We have demonstrated JWST/NIRSpec is a powerful tool to understand the properties of high redshift galaxies and to help in our understanding of the reionization era. An exciting prospect for the JWST era is the robust confirmation of ionized bubbles at $z \gtrsim 6$. Observations of UV-faint galaxies with low Lyα velocity offsets should indicate the presence of large ionized bubbles, as to observe Lyα close to systemic velocity during reionization implies a low optical depth at line center. The demonstrated low Lyα velocity offsets in our sample motivate deep, high resolution spectroscopy of reionization era galaxies with JWST/NIRSpec, to obtain Lyα and optical line measurements to enable such studies.

Acknowledgments

This work is based on observations on observations made with the NASA/ESA/CSA James Webb Space Telescope. The JWST data were obtained from the Mikulski Archive for Space Telescopes at the Space Telescope Science Institute, which is operated by the Association of Universities for Research in Astronomy, Inc., under NASA contract NAS 5-03127 for JWST. These observations are associated with program JWST-ERS-1324. The specific observations analyzed can be accessed via [doi:10.17909/9a2g-sj78]doi:10.17909/9a2g-sj78. GPL and CM acknowledge support by the VILLUM FONDEN under grant 37459. The Cosmic Dawn Center (DAWN) is funded by the Danish National Research Foundation under grant DNRF140. We acknowledge financial support from NASA through grant JWST-ERS-1324. MB acknowledges support from the Slovenian national research agency ARRS through grant N1-0238. We thank Dawn Erb and Dan Stark for sharing velocity offset measurements.

LYMAN-ALPHA EMISSION AT THE END OF REIONIZATION

4

This chapter contains the unpublished upcoming article written by me as the main author:

"Lyman-alpha emission at the end of reionization: line strengths and profiles from MMT and JWST observations at** $z \sim 5-6$**"

Authors: ***Gonzalo Prieto-Lyon****, Charlotte Mason, Victoria Strait, Gabriel Brammer*

Abstract

With JWST, it is now possible to use Lyman-Alpha (Lyα) emission from galaxies beyond $z > 8$ to trace neutral hydrogen in the intergalactic medium (IGM) as the Universe became reionized. However, observed Lyα emission lines are affected by scattering by neutral hydrogen in both the IGM and the interstellar and circum-galactic medium, necessitating 'baseline' models of Lyα properties in the ionized IGM to disentangle their impacts. In this work, we characterize Lyα properties at the end of reionization, $z \sim 5-6$, providing a baseline that can be applied to $z > 6$ observations.

We targeted GOODS-N with MMT/Binospec, obtaining R$\sim$4360 rest-frame UV spectra of 236 galaxies at $z \sim 5-6$, finding 65 Lyα detections. We use overlapping JWST observations from JADES and FRESCO for a subset of our sources to characterize Lyα properties as a function of UV continuum and rest-frame optical emission line properties. We present the first statistical measurements of the Lyα FWHM distribution at $z \sim 5-6$, and produce empirical baseline models of Lyα equivalent width (EW$_{\mathrm{Ly}\alpha}$) and escape fraction (f_{esc}) based on UV magnitude.

We find a strong dependence of our EW$_{\mathrm{Ly}\alpha}$ and f_{esc} models on UV magnitude, and infer that 45$\pm$5% and $< 62 \pm 8\%$ of M$_{\mathrm{UV}}$ = -19.5 galaxies have EW$_{\mathrm{Ly}\alpha} > 25$Å and $f_{\mathrm{esc}} > 0.2$, respectively. We find a mean FWHM$_{\mathrm{Ly}\alpha}$ of 120 km s^{-1} and median Lyα velocity offset of 258 km s^{-1} , finding positive correlation of these properties with UV luminosity and optical line broadness. Compared to models based on $z \sim 2$ Lyα emission lines, our median observed line profile is narrower with significantly higher velocity offset, enhancing Lyα transmission in a fully neutral IGM by up to 5 ×, providing insight into recent detections of Lyα emission at $z > 10$.

4.1 Introduction

The epoch of reionization (EoR) was the last phase transition of the Universe, when the majority of the neutral hydrogen in the intergalactic medium (IGM) became ionized due to the injection of ionizing photons from the first galaxies (e.g., Stark, 2016). The rate and morphology of this transition is determined by the galaxies' ionizing properties and thus constraining the reionization process offers unique insights into early galaxies, even those below our direct detection limits. Multiple independent studies have reached consensus that the Universe was fully reionized at z$\sim$ 5 - 6 (e.g. Fan et al., 2006; Gaikwad et al., 2023; Qin et al., 2021; Bosman et al., 2022), but likely predominantly neutral at $z \sim 7-8$ (e.g., Stark et al., 2010; Treu et al., 2012; Pentericci et al., 2014; Schenker et al., 2014; Mason et al., 2018a; Davies et al., 2018; Yang et al., 2020; Wang et al., 2020; Jung et al., 2020; Whitler et al., 2020; Bolan et al., 2022; Umeda et al., 2024; Nakane et al., 2024; Tang et al., 2024c; Jones et al., 2024a). The earliest stages of reionization at $z > 9$ are still very poorly constrained, but will be crucial for understanding the build up of the first galaxies and the higher than expected UV luminosity density detected by JWST (Gelli et al., 2024; Muñoz et al., 2024).

Lyman-alpha (Lyα) emission from galaxies is one of our best probes of the early stages of the EoR. Its high cross-section for damping wing scattering by neutral hydrogen means Lyα flux traces the IGM opacity (e.g., Miralda-Escude, 1998; Mesinger & Furlanetto, 2008) and we are now detecting 1000s of $z > 8$ galaxies with JWST (e.g. Donnan et al., 2024; Witstok et al., 2024b; Tang et al., 2024b; Jones et al., 2024b), providing large samples to comprehensively trace the IGM at high redshift. By contrast, the number density of quasars, the typical IGM probes at lower redshifts (e.g., Fan et al., 2006; Eilers et al., 2019; Bosman et al., 2022), decreases at $z > 7$ (Euclid Collaboration et al., 2019). The visibility of Lyα from galaxies drops considerably at $z > 6$, implying an increasing neutral IGM (e.g., first seen in the declining fraction of galaxies detected with strong (EW$>$ 25 Å) Lyα , Stark et al., 2010; Pentericci et al., 2014; De Barros et al., 2017; Fuller et al., 2020; Tang et al., 2024a).JWST has opened a new window on reionization studies – enabling Lyα observations in faint galaxies at $z \gtrsim 6$ without the atmospheric and sensitivity limitations of ground-based telescopes. Early JWST results have confirmed the downturn in Lyα emission at $z \gtrsim 6$ seen from the ground and demonstrated strong Lyα is extremely rare at $z > 8$ in current samples (Nakane et al., 2024; Chen et al., 2024; Tang et al., 2024a; Jones et al., 2024a), and have also provided the first detections of Lyα at $z > 10$ (Bunker et al., 2023; Witstok et al., 2024b). These observations demonstrate JWST will be a key tool to understand the earliest stages of reionization.

However, the interpretation of Lyα observations during the Epoch of Reionization rests on understanding the transmission of Lyα on multiple spatial scales. Lyα photons are subject to scattering not only by neutral hydrogen in the IGM, but also in the interstellar and circumgalactic media (ISM and CGM). To use Lyα to track the reionization history, an understanding of Lyα emerging from the ISM/CGM is necessary. In particular, because of the strong wavelength dependence of the IGM Lyα damping wing (Miralda-Escude, 1998), both an understanding of the Lyα line strength and *spectral shape* emerging from the ISM/CGM is important to disentangle the impact of the IGM (Dijkstra et al., 2011; Mason et al., 2018b; Endsley et al., 2022b).

To this end, samples of galaxies at the end of the EoR, z ∼ 5 - 6 have been commonly used as a baseline for interpreting higher redshift observations (Stark et al., 2011; De Barros et al., 2017). These galaxies are expected to be physically similar to those at earlier epochs, but suffer minimal damping wing attenuation by the neutral IGM. Therefore, these galaxies provide a window into the emergent Lyα emission from the ISM & CGM, and have been used to infer the additional impact of the IGM on $z > 6$ galaxies' Lyα (e.g., Mason et al., 2018a; Whitler et al., 2020; Jung et al., 2020; Bolan et al., 2022). However, these baseline samples had been limited to the most readily available observables pre-JWST – Lyα EW and UV photometry, and, with only a handful of systemic redshifts known from strong rest-UV or FIR lines (e.g., Stark et al., 2017; Bradač et al., 2017), our knowledge of the emerging Lyα line profile had been severely limited. These and other limitations, such as the unknown Lyα profile broadness distribution at z∼6, have led previous models (Mason et al., 2019) to rely on empirical relations based on $z \sim 2$ galaxy samples. However, it is unclear whether $z \sim 2$ samples are good analogs of reionization-era sources. For example, recent works have shown the Lyα velocity offsets of z∼6 galaxies appear systematically higher than models derived from $z \sim 2$ galaxies (Prieto-Lyon et al., 2023b; Tang et al., 2024a). JWST's ability to observe the rest-frame optical is transforming our ability to understand galaxies in this era. We now have systemic redshifts for 1000s of $z > 5$ galaxies (e.g., Roberts-Borsani et al., 2024) and measurements of Lyα escape fractions ($f_{\rm esc}$), relative to Balmer lines, and velocity offsets ($\Delta v_{\rm Ly\alpha}$) are now routinely being measured for $z \sim 5 - 9$ galaxies (e.g., Lin et al., 2024; Chen et al., 2024; Tang et al., 2023, 2024a; Saxena et al., 2024). Tang et al. (2024a) recently presented constraints on the emergent Lyα EW and escape fraction distributions in bins of $M_{\rm UV}$, UV β slope and [OIII]+Hβ EW, and velocity offset distributions in $z \sim 5-6$ galaxies. These observations are providing a more detailed baseline for understanding emergent Lyα during reionization (Tang et al., 2024c).

However, these works have mostly focused on measuring Lyα emission distributions in bins of galaxies properties, limiting the information used in the conditional distributions, and much less attention has focused on the shape of the Lyα line profile at $z \sim 5-6$. Accurately measuring the emergent lineshape is critical for understanding the transmission of Lyα through the IGM (Dijkstra & Wyithe, 2010; Mason et al., 2018a, 2019; Endsley et al., 2022b; Tang et al., 2024b; Mukherjee et al., 2024). High resolution spectroscopy is required to accurately measure both the asymmetric shape of Lyα, and its offset from the systemic redshift ($\Delta v_{\mathrm{Ly}\alpha}$). Resolution below $\sim$ 100 km s^{-1} ($R \gtrsim 4000$) is optimal, as typical full-width half-max (FWHM) in local Lyα -emitters range from $\sim 100-400$ km s^{-1} (Verhamme et al., 2018) and values of $\Delta v_{\mathrm{Ly}\alpha}$ range from 150 km s^{-1} to 500 km s^{-1} (e.g., Prieto-Lyon et al., 2023b; Tang et al., 2024a). Tang et al. (2024a) demonstrated that $z \sim 5-6$ Lyα lineprofiles appear more offset from systemic than profiles for comparable sources at $z \sim 2-3$, implying residual neutral gas in the ionized IGM is resonantly scattering Lyα close to linecenter. But we currently have no statistical information about the broadness and asymmetry of Lyα line profiles at these redshifts, primarily due to the moderate resolution of Lyα spectroscopy in fields overlapping with deep JWST spectroscopy (i.e. VLT/MUSE $R \sim 3000$).

To that end, we have carried out a deep, high-resolution ($R \sim 4400$) near-infrared spectroscopic survey of 236 $z \sim 5-6.5$ Lyman-break galaxies in the GOODS North field (Giavalisco et al., 2004), selected from deep HST imaging, with MMT/Binospec (Fabricant et al., 2019), with the aim of constraining the Lyα strength, and line profiles emerging from the ISM/CGM of galaxies in the post-reionization era. Our sample includes 65 Lyα detections. Thanks to the excellent ancillary datasets in GOODS-N, we supplement our Lyα spectroscopy with JWST/NIRCam slitless spectra from FRESCO (Oesch et al., 2023), and deep HST and JWST photometry from the CANDELS (Giavalisco et al., 2004; Grogin et al., 2011; Koekemoer et al., 2011) catalog by Barro et al. (2019) and JADES (Eisenstein et al., 2023a) to obtain precise measurements of galaxy properties (UV magnitudes, UV β slopes, systemic velocities, Lyα escape fractions: $f_{\rm esc}$). With these data we build two new empirical models for $\rm EW_{Ly\alpha}$ and $f_{\rm esc}$ conditional on UV observables, $\rm M_{UV}$ and β, which can be used as a baseline for constraining the reionization history. We also explore the properties of Lyα lineprofiles ($\Delta v_{\rm Ly\alpha}$, FWHM, asymmetry) in our sample.

The paper is structured as follows. In Section 3.2 we describe our target selection, the MMT/Binospec spectroscopy and ancillary datasets. In Section 4.3 we describe our Lyα and rest-optical emission lines measurements. We describe our Lyα measurements in the context of other galaxy properties in Section 4.4. We present our new empirical model for emergent $\rm EW_{Ly\alpha}$ and $f_{\rm esc}$ in Section 4.5. We discuss our results in 3.5 and present our conclusions in Section 4.7. We assume a flat ΛCDM cosmology with $\Omega_m = 0.3$, $\Omega_\Lambda = 0.7$, $h = 0.7$. All magnitudes are in the AB system.

4.2 DATA

Here we describe the observational dataset used in this work. First, we describe our target selection (Section 4.2.1) and the MMT/Binospec spectroscopic observations of z ∼ 5 - 7 Lyman Break Galaxies in the GOODS-N field (Section 4.2.2). Second, we describe the JWST/NIRCam slitless spectroscopy from the FRESCO survey[*] which provides rest-frame optical spectroscopy of a subset of our targets (Section 4.2.3). Finally we describe the JWST and HST photometric datasets from the DJA [†] (The DAWN JWST Archive) photometric catalog of JADES[‡] (Eisenstein et al., 2023b), the CANDELS/SHARDS (Giavalisco et al., 2004; Grogin et al., 2011; Koekemoer et al., 2011) catalog by Barro et al. (2019) and 3D-HST[§](Skelton et al., 2014; Brammer et al., 2012) imaging in Section 4.2.4.

4.2.1 TARGET SELECTION

Our primary targets are 236 $z_{\rm phot} \sim 5-7$ candidates in GOODS-N (Giavalisco et al., 2004) selected by Lyman-Break color criteria from Bouwens et al. (2015). All candidates are de-

---

[*] https://jwst-fresco.astro.unige.ch

[†] https://dawn-cph.github.io/dja/

[‡] https://jades-survey.github.io

[§] https://archive.stsci.edu/prepds/3d-hst/

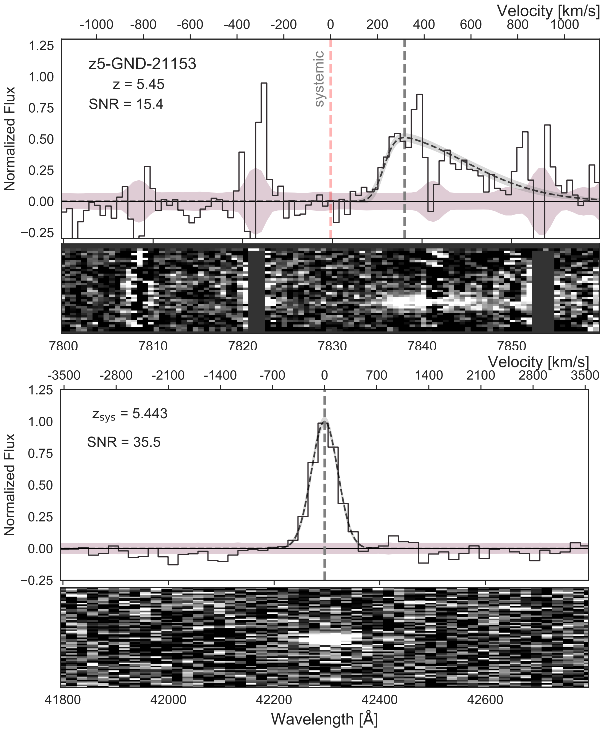

Figure 4.1: Spectra of z5-GND-21153. Top: MMT/Binospec spectra of Lyα . Bottom: Hα counterpart from JWST/NIRCam of the same source. Dashed line and shaded area show the emission line fit and the corresponding 1σ uncertainty of the fit. On the left, the vertical red line shows the systemic/Hα redshift, in this example there is a $315\,\mathrm{km\,s^{-1}}$ velocity offset between Lyα and Hα . The upper axis shows velocity centered at the peak of the systemic line. In the bottom are the 2D spectra.

tected with a magF160W< 27.5. ACS/WFC & WFC3/IR filters from the deep GOODS imaging were used for tracing the Lyman-Break and the rest-frame UV continuum, and two low wavelength Spitzer/IRAC bands break the degeneracy between the Lyman-Break and 4000Å break. The 236 sources include 24 spectroscopically confirmed Lyα -detected galaxies previously reported by Hu et al. (2010), Stark et al. (2011), and Jung et al. (2018), in order to obtain higher resolution, higher S/N observations of their Lyα lineshapes.

4.2.2 MMT / Binospec

We performed observations of our targets in GOODS-N with MMT/Binospec (Fabricant et al., 2019). The observations are divided into 4 masks with two detectors of 8'x15' field of view, covering a total footprint of 0.27 deg^2, with exposure times between 10 - 16 hours per mask. We used the 600 lines/mm grating, providing R$\sim$4360 and a wavelength range between 7255 - 9750 , enabling Lyα detections between z = 4.9 to 7.0. Thanks to the high resolution per pixel, 0.61 /pix and instrumental resolution of ≈ 70 km s^{-1} , we are able to accurately retrieve the profile shape of the observed Lyα lines, improving on e.g., JWST NIRSpec and VLT/MUSE Lyα observations ($R \sim 3000$) by a factor of 45%. In Figure 4.1 we show an example of our Lyα spectra. Properties of each mask are described in Table 4.1.

4.2.3 JWST / NIRCam - Slitless Spectra

We include NIRCAM/grism observations from FRESCO (Oesch et al., 2023) which targeted 62 arcmin^2 in GOODS-N, covering 82/236 of our MMT/Binospec targets. The wavelength range with the F444W filter covers 3.8-5μm, allowing the observation of the most luminous optical lines, Hα and the [OIII] doublet, from z$\sim$4.8-6.6 and z$\sim$6.6-9 respectively, with R$\sim$1600≈ 180 km s^{-1} . This provides systemic redshift for a subset of our targets, with lines fluxes above the FRESCO average 5σ flux limit of 2$\cdot$10^{-18}erg s^{-1} cm^{-2}. Hα flux measurements also provide an estimate of the intrinsic Lyα flux, enabling us to estimate Lyα escape fractions. The reduction and spectral extraction of FRESCO data reported by Oesch et al. (2023). The accuracy of the wavelength calibrations is crucial due for Lyα velocity offsets near the instrumental resolutions (See Figure 4.1). To verify the calibration, we compare the systemic redshift of FRESCO sources with known ground-based spectra, and find no substantial systematic differences, with a scatter in the order the wavelength pixel resolution. We show the spectra of all galaxies with a Lyα and optical line detection in Appendix 4.9.

4.2.4 Photometric Data

Deep HST and JWST photometry of our candidates is provided by JADES (Eisenstein et al., 2023a), CANDELS (Giavalisco et al., 2004; Grogin et al., 2011; Koekemoer et al., 2011), and 3D-HST (Skelton et al., 2014) imaging in GOODS-N. These data provide rest-frame UV coverage of our targets. JADES JWST/NIRCam imaging covers 128/236 of our targets, and provides imaging in F090W, F115W, F150W, F200W, F277W, F335M, F356W, F410M, and F444W.

We use the data reduction from DJA processed with *grizli* (Brammer, 2023) which includes both NIRCam imaging from JADES and legacy HST ACS/WFC & WFC3/IR bands reduced self-consistently (Valentino et al., 2023) (JADES-DJA). For sources outside of the FoV of JADES, we use ACS/WFC & WFC3/IR photometry catalogs from Barro et al. (2019), which provide consistent photometry to the Valentino et al. (2023) catalogs. In cases where we do not find a match in either catalog, we use photometry from 3D-HST (Skelton et al., 2014). For all catalogs we use aperture corrected fluxes.

4.2.5 Data Reduction

We use the synthetic models that best fits the spectrum of our standard stars. We extract and normalize the spectra to obtain the telluric transmission $T(\lambda)$ by dividing the data by the model (both continuum normalized). We apply the transmission function to all spectra in each exposure:

$$f_{corr}(\lambda) = \frac{f_{obs}(\lambda)}{T(\lambda - \alpha)^{\beta}} \tag{4.1}$$

The constant α accounts for any wavelength shifts between the spectra and transmission and β is used as a scaling factor of the transmission. To calculate α and β we minimize the RMS in the two most important telluric regions, O2 A& B bands in $f_{corr}(\lambda)$ for every exposure for every slit containing a high redshift target.

We perform flux calibration for each exposure by calibrating our standard stars with magnitudes obtained in the *SDSS* (Abdurro'uf et al., 2022). We use the i filter of *Sloan* since it covers a similar wavelength range as the MMT/Binospec data. We convolve our standard star spectra with the corresponding i_{sdss} filter using SEDPy.

We perform additional sky subtraction of the exposures for each mask, to improve on the pipeline sky subtraction. We make a global 1D sky spectrum for each individual exposure, $S(\lambda)$, using the standard deviation of flux in all slits containing $z > 5$ targets with no clear emission lines (as our targets are faint, we do not expect to detect the continuum, so the 'empty' slits should measure the sky), using sigma clipping to remove any cosmic rays. We

	Exposure Time [hr]	Median Seeing†	Flux Limit (5σ) [erg s^{-1} cm^{-2}]	Targets	Lyα detections
Mask 1	15.5	0.90″	1.26×10^{-17}	93	30
Mask 2	13.0	0.85″	1.26×10^{-17}	80	17
Mask 3	13.3	0.92″	1.35×10^{-17}	60	12
Mask 4	7.8	0.97″	1.63×10^{-17}	50	7

Table 4.1: Overview of Binospec masks and $z \sim 5 - 7$ targets (Section 4.2.2). † After excluding exposures with seeing $> 1.2''$.

perform additional sky subtraction to each spectrum per exposure as:

$$f_{\text{skysub}}(\lambda) = f_{\text{obs}}(\lambda) - A \cdot S(\lambda) \tag{4.2}$$

We find A by minimizing the RMS of $f_{\text{skysub}}(\lambda)$ per slit's exposure given the S(λ) measured in each mask, so that the distribution of signal in an empty region of the slit is centered around $\frac{S}{N} \sim 0$. For this we use *LMFIT: non-linear least-squares minimization*[¶].

We finally merge the telluric corrected, flux calibrated and sky subtracted exposures into the final science spectra, using sigma clipping to remove cosmic rays. Exposures with seeing above $1.2''$ are excluded. Table 4.1 provides an overview of the exposure times, average seeing and targets for each of our four masks.

4.3 Lyman-Alpha and rest-frame optical line identification

In the following section we describe our search for Lyα emission in our MMT/Binospec spectra (Section 4.3.1), and Hα and/ or [OIII] emission in the FRESCO JWST/NIRCam slitless spectra (Section 4.3.2).

[¶] https://lmfit.github.io/lmfit-py/

4.3.1 Lyman-alpha emission line detection

For the case of spectroscopically confirmed galaxies (either from rest-optical lines or existing Lyα spectroscopy), extracting the Lyα profile is straightforward since the redshift is already known. For sources without spectroscopic confirmation we perform a systematic search for the emission line given the photometric redshift.

We first collapse the 2D spectra into 1D spectra for each target by extracting within the median spatial extension of our Lyα detections (= 1.7″ = 7 pixels). We maximize the signal captured in the extraction, with more extended extractions the SNR plateaus adding mostly noise. Starting at the position of the UV continuum, we repeat this process for every spatial position of the slit within 2.4″ of the UV coordinates to account for any spatial offset between the UV continuum and Lyα emission (Hoag et al., 2019a; Lemaux et al., 2021). We then scan through the 1D spectra to search for high SNR peaks, scanning all wavelengths. We flag line candidates where SNR$\geq$3 is found in 3 consecutive wavelength pixels, essentially an integrated SNR$\geq$ 5 detection. Finally, we manually inspect the candidate lines in the 1D and 2D spectra to remove any false positives near the sky lines or from randomly high peaked background. For galaxies where we have a systemic redshift from the restframe-optical lines, we do a manual search of Lyα within $\sim$ 2000 km s^{-1} of the systemic redshift. For detected emission lines we measure Lyα fluxes from a fitted asymmetric Gaussian (Section 4.3.1.3) as this allows for more accurate measurements in the case of strong skylines near the emission line than obtaining the flux directly from the 1D spectra.

4.3.1.1 Completeness

To evaluate the completeness of our emission line search we perform Monte Carlo simulations. We add simulated Gaussian Lyα profiles at random wavelengths into the slits of non-detected targets and then attempt to recover them with the method described above. We vary the line flux and FWHM as these are the most important factors in determining the detection of a line, and show the resulting completeness in Figure 4.2. The asymmetry of the profile is sub-dominant to the flux and FWHM so we use a Gaussian profile for simplicity. The presence of sky lines plays an important role, retrieval is unlikely if an emission line falls at the same wavelength, leading to high redshift line recovery to be even harder due to the increased

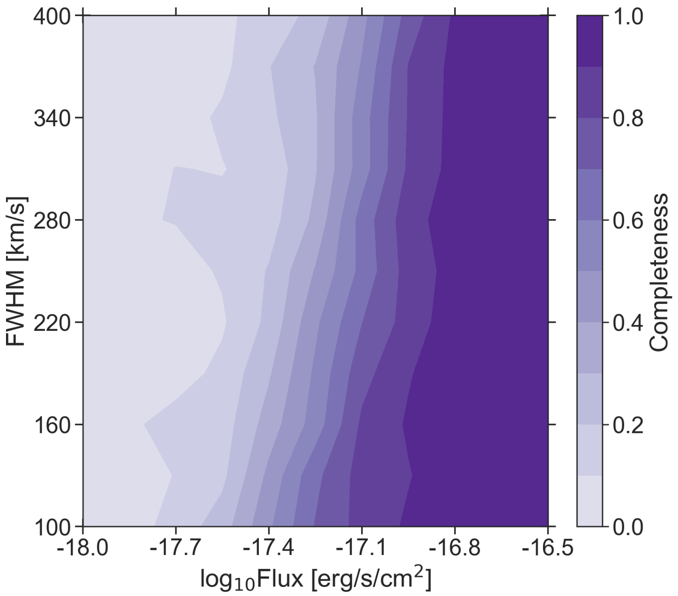

Figure 4.2: Here we show the completeness of our Lyα search as a function of observed FWHM and flux. The fraction of recovered detections drops with increased line broadness.

sky line emission at longer wavelengths.

Figure 4.2 shows the line flux is the most significant factor in completeness. We achieve $>$ 80% completeness for fluxes $\gtrsim 10^{-17}$ erg s cm^{-2}. The FWHM of the line impacts completeness by 10% at fixed line flux across the range we considered: $100 - 400$ km s^{-1} .

4.3.1.2 SLIT LOSSES

As Lyα can be spatially extended beyond the width of our extraction window (1.7") we correct our Lyα fluxes for slit losses following the approach of Tang et al. (2024a). We first produce a 2D Lyα surface brightness profile following for typical z∼5-6 galaxies as measured by MUSE (Leclercq et al., 2017): consisting of two declining exponential functions to describe a Lyα core and an extended Lyα halo, with 0.3 kpc and 3.8 kpc exponential decay constants respectively. We allocate 35% and 65% of the total flux to the core and halo respectively. We convolve the resulting model with the PSF of each mask, and quantify the flux that would be obtained following the Lyα extraction (7pix $\sim 1.7''$).

For all sources, we estimate $65 - 70\%$ of the total Lyα flux is captured by our extractions in the Binospec slits. We take this into account for any calculations involving these quantities. We calculate the slit loss directly for individual sources, and use the median of 67% slit loss for our non-detection upper limits. We note that we assume each galaxy has the same surface brightness profile, therefore the only difference between galaxies will be the redshift and following angular size conversion.

4.3.1.3 Lyα FLUXES AND UPPER LIMITS

For galaxies with Lyα detections we obtain line fluxes by fitting the lines with an asymmetric Gaussian profile, this enables us to account for the presence of sky lines. Thanks to the $R \sim 4000$ resolution of our spectra, we are able to observe detailed Lyα line profiles for our detections. We fit a skewed Gaussian model to our Lyα lines:

$$f(x; A, \xi, \omega, \alpha) = \frac{A}{\omega\sqrt{2\pi}} e^{[-(x-\xi)^2/2\omega^2]} \Big\{ 1 + \mathrm{erf}\big[\frac{\alpha(x-\xi)}{\omega\sqrt{2}}\big] \Big\} \tag{4.3}$$

The location is represented by ξ. The skewness is parameterised by α. The scale is ω and it describes the standard deviation with a factor of skewness. For example, a symmetrical Gaussian profile will have $\alpha = 0$, while for a completely red-sided asymmetric profile $\alpha \rightarrow +\infty$. When fitting we fix $\alpha \geq 0$ as we expect only profiles which are truncated on the blue side due to the resonant scattering of Lyα photons (Laursen et al., 2011). The flux of the line is then obtained by integrating the resulting line profile. To be consistent with the literature, we extract the FWHM by its definition, by measuring the width of the profile at half its maximum and subtract the instrumental resolution in quadrature.

We fit the line profiles using an MCMC with the python library *emcee*[‖] (Foreman-Mackey et al., 2013). As the skewness, is most sensitive to $\alpha \sim 0-3$ we set a log uniform prior on the skewness between $\alpha \varepsilon$ [0,15], allowing perfectly Gaussian to completely asymmetric profiles. For all other parameters of the fit, amplitude,location and scale, we use uniform priors with positive values. By setting 30 walkers with 2000 steps, with a burn-in of 750 steps, we obtain converged distributions for our parameters. We use the chains of the MCMC to measure the FWHM posterior distribution. In Appendix 4.9 we show some examples of the spectra and

---

[‖] https://emcee.readthedocs.io/

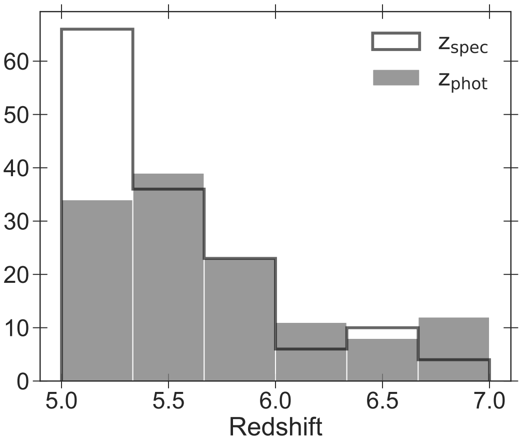

Figure 4.3: The final sample consists of 236 galaxies. It consists of 131 galaxies which have neither Lyα or Hα (gray), the lack of emission might comes from a non-detection of Lyα , and Hα not being observed or detectable. The other 105 sources have a spectroscopic redshift, from either Lyα and/or Hα or [OIII] (black).

the resulting fits.

For the galaxies which do not show a Lyα emission feature, we calculate flux upper limits using the following procedure. We add simulated emission lines to the 2D spectra of our sources, considering a grid of flux, FWHM and redshift. We take uniformly distributed values of flux between $0.1 - 3.2 \times 10^{-17}$ erg/s/cm^2, and FWHM values between $100 - 400$ km/s, which span the range we find most of our detections (see Section 4.4). To account for the presence of skylines and the photometric redshift we take uniformly distributed values of redshift within $z_{phot} \pm 0.5$. We generate fully asymmetric Gaussian profiles and run the line selection code (Section 4.3.1) to detect SNR$>$ 5 simulated lines.

We simulated 500,000 lines for each galaxy across the above grid of parameters. We calculate the minimum detectable line flux for every sampled FWHM and redshift. We take the median of the resulting flux distribution as the Lyα flux limit for the galaxy.

4.3.2 REST-FRAME OPTICAL EMISSION LINE DETECTION

82/236 of our Binospec targets fall into the footprint of JWST/NIRCam grism slitless spectroscopy from FRESCO (Section 4.2.3), providing rest-frame optical emission line coverage. We perform an initial search for emission lines based on the *grizli* extractions (Brammer & Matharu, 2021) and refine the search around the Lyα redshift for Lyα detections or photometric redshift for Lyα non-detections. We require a total SNR>5 extracted over the median FWHM of the detections ($385\,\mathrm{km\,s^{-1}}$) as a detection limit for rest-frame optical lines. Due to the nature of the slitless spectra, contamination from emission lines of overlapping galaxies is present in some of our sources, this effect is mostly taken into account by the extraction as described by Oesch et al. (2023). In cases where there is a misidentification between the Lyα of our target and emission lines of a foreground source, we look for extra emission lines to discard the foreground source, as these do not match with the z_{spec}.

For the 25 galaxies with detected Lyα emission which fall in the FRESCO footprint, we do a manual search for SNR>5 rest-optical emission lines within $\sim 2000\,\mathrm{km\,s^{-1}}$ of the Lyα redshift**. We detect either Hα or [OIII] for 11/25 galaxies. For the remaining 57 targets with no Lyα detection in Binospec we search over the complete FRESCO wavelength range 3.835 - 5.084 micron for any optical emission lines, focusing mostly within $z_{\mathrm{phot}} \pm 0.5$. We detect H$\alpha$ or [OIII] for 51/82 galaxies. Overall, 62% of our targets with overlapping FRESCO data were spectroscopically confirmed. Using the systemic redshifts obtained from JWST/FRESCO, we go back to the rest-frame UV data of MMT/Binospec. We replace the photometric redshifts for systemic redshifts and perform a new search for Lyα, and find 2 new detections that we failed to recover in our previous searches.

In Figure 4.3 we show the redshift distribution of the sample. We have a final number of 236 galaxies. We are able to obtain a spectroscopic redshift for 105 galaxies via three approaches: Lyα, Hα and [OIII]. Out of the 105 sources, 65 have Lyα emission, 50 have Hα emission and 1 has [OIII]. Out of these, 10 have Lyα + Hα and 1 has Lyα + [OIII]. For 131 targets no emission line was found. We find a median redshift of 5.6 in both the spectroscopic and photometric redshift samples.

** Lyα velocity offsets are typically $\sim 100-500\,\mathrm{km\,s^{-1}}$, with rare instances of offsets up to $1000-2000\,\mathrm{km\,s^{-1}}$ (e.g. Erb et al., 2014; Steidel et al., 2014; Tang et al., 2023; Bunker et al., 2023; Prieto-Lyon et al., 2023b)

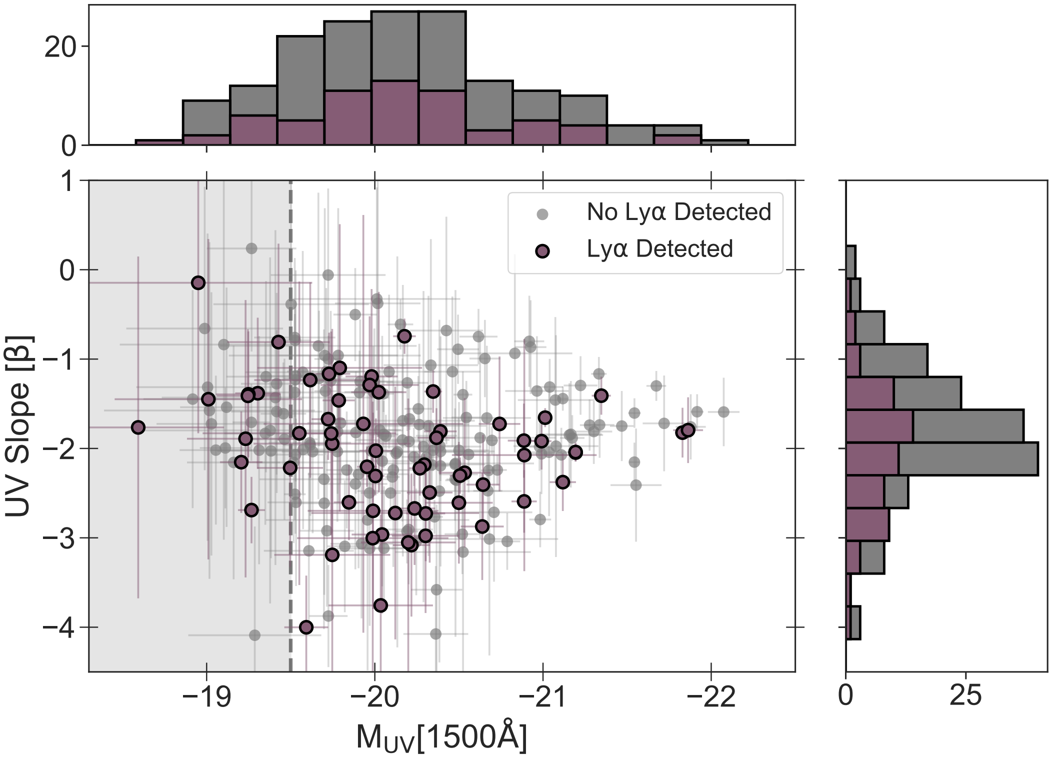

Figure 4.4: M_{UV} and β slope. We show galaxies with Lyα detected (purple) and galaxies without detected Lyα (gray). These observations are the input into our two empirical models and other results. On top we show the M_{UV} distribution, there is no substantial difference between Lyα galaxies and Lyα non detections, with median M_{UV} of -20.0 and -20.1 respectively. On the right, the UV slope distribution, both populations show small difference, with median β of -2.0 and -1.8 respectively. The shaded area highlights the range where our sample becomes incomplete due to our target selection (see Section 4.6.1 for discussion).

To obtain line fluxes, centroids and intrinsic FWHM we fit a Gaussian line profile to the detected rest-optical emission lines. We show the resulting 1D and 2D spectra for the rest-frame optical lines and the fitted models in Appendix 4.9. We calculate the flux limits for non-detections with a SNR=5 limit, given the 1D noise array with an extraction the size of the median Hα FWHM ($= 375\,\mathrm{km\,s^{-1}}$) at $z_{Ly\alpha}$ or z_{phot}.

4.4 Lyman Alpha and Galaxy Properties

The combination of high resolution Lyα spectroscopy, deep HST and JWST photometry, and rest-frame optical JWST spectroscopy allows us to characterize Lyα emission in our

$z \sim 5-6$ sample via measurements of Lyα EW, line profiles and velocity offsets, and escape fractions. In the following section we describe these properties in our sample and investigate trends between Lyα properties and galaxy properties to better understand Lyα transmission in the ISM and CGM in our sample.

4.4.1 UV Continuum properties

We calculate the UV absolute magnitude (M_{UV}) and UV slope (β) for our targets using HST and JWST photometry as described in Section 4.2.4. We include only filters that have their effective width (W_{eff}) within the rest-frame UV between $1250-2600$ Å so as to not include bands containing Lyα flux. We obtain all filter information from Rodrigo & Solano (2020). For the redshift, we use $z_{Ly\alpha}$ when Lyα is detected, and z_{phot} when it is not detected.

We fit a power law, $f_\lambda \propto \lambda^\beta$, to the selected photometric filters that capture the UV continuum. We retrieve M_{UV} by evaluating the fit at 1500Å. For sources with JWST NIRCam data, the M_{UV} and β estimates are consistent with the HST estimates, but we obtain lower uncertainties. We fit the continuum using an MCMC method assuming a Gaussian likelihood for the flux densities.

We plot the resulting M_{UV} and β for our sample in Figure 4.4, showing the median and 1σ uncertainties. Similarly to previously reported trends in the literature (e.g. Bouwens et al., 2012, 2014) we see β increase as galaxies are brighter in UV magnitude, but this correlation becomes unclear for fainter sources. We find our F160W selection is incomplete for $M_{UV} > -19.5$ sources with blue ($\beta < -2$) UV slopes, which we discuss later in Section 4.6.1.

Overall we see no significant difference in the M_{UV} distributions between galaxies with and without Lyα detection, with median values of $M_{UV} = -20.0$ and -20.1 respectively. We find a slight difference in the β slope distributions for galaxies that had a Lyα detection and galaxies that do not: galaxies with Lyα detection show bluer β slopes, with a median value of β = -2.0 , compared to β = -1.8 for galaxies without Lyα detections. Performing a *Kolmogorov-Smirnov* (KS) test shows a p-value$>$ 0.1, implying a weak difference between the β slope distribution of galaxies with and without detected Lyα .

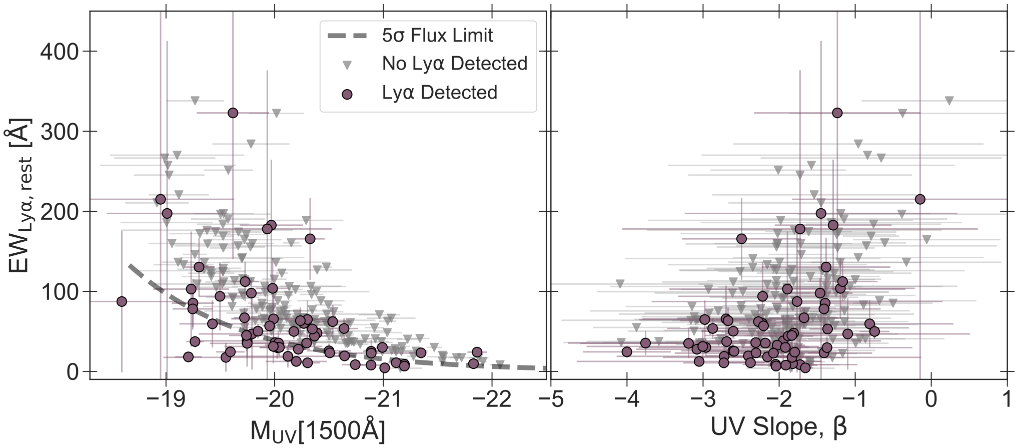

Figure 4.5: Left: M_{UV} and rest-frame $EW_{Ly\alpha}$. Right: β slope and rest-frame $EW_{Ly\alpha}$. We show galaxies with Lyα detection (purple) and galaxies without Lyα detection (gray) as upper-limits. We find increased $EW_{Ly\alpha}$ at fainter M_{UV} , similar to previous works (e.g. Shapley et al., 2003; Stark et al., 2011; Oyarzún et al., 2017; Tang et al., 2024a), and an unclear correlation with UV-slope. We show the median 5σ flux limit of the survey in dashed line.

4.4.2 Lyα Equivalent Widths

To calculate Lyα rest-frame equivalent widths (EW), we compare the Lyα flux, or upper limit, with the flux density of the UV continuum. We estimate the continuum flux density, $f_{\lambda,UV}$, at the Lyα wavelength, 1215.6 Å, using our power-law fit to the UV continuum (Section 4.4.1). The rest-frame EW is:

$$\mathrm{EW_{rest}} = \frac{\mathrm{F_{Ly\alpha}}}{\mathrm{f_{\lambda,UV}}(1+z)} \tag{4.4}$$

Where $F_{Ly\alpha}$ is the total flux of the Lyα line in erg s^{-1} cm^{-2} (or upper limit) and $f_{\lambda,UV}$ the flux density [erg s^{-1} cm^{-2} $^{-1}$] of the UV continuum at 1215.6. As our sources are faint and the continuum is not detected in the spectra, we do not perform continuum subtraction. For sources with only photometric redshifts we use z_{phot} as the redshift.

In Figure 4.5 we show our $EW_{Ly\alpha}$ measurements against the 2 UV observables. We mainly find enhanced $EW_{Ly\alpha}$ in UV faint galaxies, while a trend with UV slope is not evidently present. We also show the average 5σ flux limit of our observations. Since the line flux limit is related to Lyα broadness, it is possible to observe lines below this limit if they are narrower than the median $FWHM_{Ly\alpha}$ of our sample.

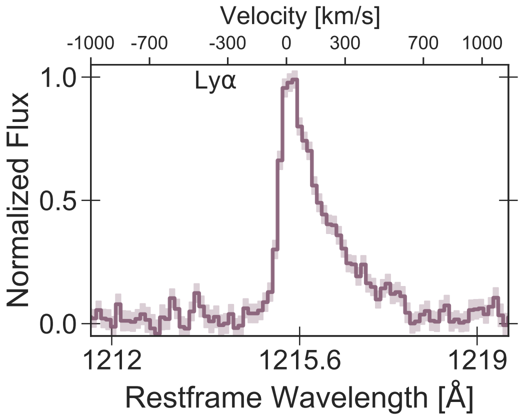

Figure 4.6: Stacked spectra of Lyα detections. Lines are stacked at their Lyα peak and shown in restframe wavelength given their $z_{\mathrm{Ly}\alpha}$. 70% of the profiles have a strong emergent asymmetric shape.

4.4.3 Lyα LINE PROFILES

Thanks to the $R \sim 4000$ ($\approx 70\,\mathrm{km\,s^{-1}}$) resolution of the Binospec spectra and high S/N of many of our detections, we are able to observe detailed Lyα line profile shapes, which offer insights into the scattering of Lyα in the ISM and CGM (e.g., Neufeld, 1991; Verhamme et al., 2006; Gronke et al., 2015). At $z \sim 0.2-2$, the strongest Lyα emitters tend to show narrow Lyα emission lines with flux close to the systemic velocity, implying Lyα is scattering in low column density neutral gas and thus not diffusing significantly in frequency space (e.g., Erb et al., 2014; Hashimoto et al., 2015; Henry et al., 2015; Yang et al., 2017b; Tang et al., 2024c). At low redshifts ($z = 0.05-0.44$), Lyα line widths and velocity offsets are seen to correlate with properties, e.g. M_{UV}, FWHM of rest-frame optical lines, which likely trace gas mass (Hayes et al., 2023). The sample of published spectra with sufficient S/N and resolution to measure Lyα lineshapes at $z \sim 5-6$ is small (e.g. MUSE resolution is $\sim 100\,\mathrm{km\,s^{-1}}$). Our sample thus provides new insights into the lineprofiles at $z \sim 5-6$. We are particularly interested in understanding if Lyα lineshapes at $z \sim 5-6$ are significantly different from lower-z samples in ways which may impact the transmission of Lyα through the IGM.

As discussed in Section 4.3.1.3 we fit our 65 detected Lyα lines with an asymmetric Gaussian profile, enabling us to measure the broadness and skewness of the lines, which we discuss in more detail below. To show our general findings on Lyα lineshapes, we produce a compos-

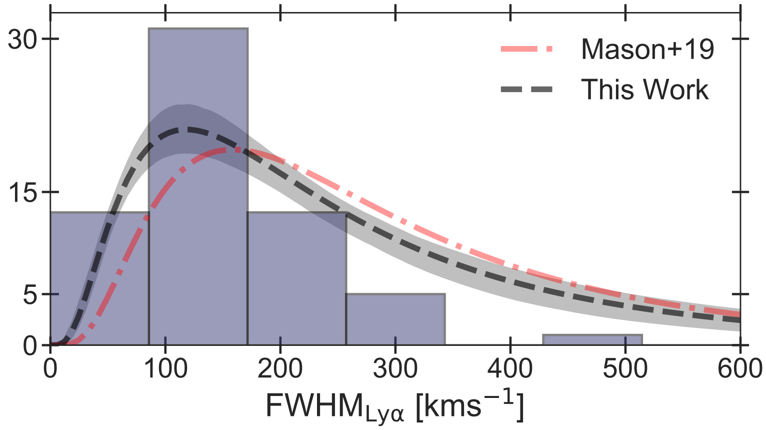

Figure 4.7: FWHM$_{\mathrm{Ly}\alpha}$ distribution of our sample. We also plot our fitted log-normal distribution: median as a black dashed line, and the 16th and 84th percentile range in a yellow region. Our log-normal distribution is similar but lower than the prediction of Mason et al. (2019) (green dashed line) evaluated at the same median M$_{\mathrm{UV}}$ and redshift as our sample.

ite spectrum (Figure 4.6). We create this by stacking each of the 65 detections at the Lyα peak (i.e. assuming $z_{\mathrm{sys}} = z_{\mathrm{Ly}\alpha}$). The stacked spectrum show a clear asymmetric shape.

A strong asymmetric shape is expected at $z \gtrsim 5$ due to resonant scattering by residual neutral gas in the ionized IGM (e.g., Laursen et al., 2011; Mason & Gronke, 2020). To explore the asymmetry in our data, we choose a binary classification of asymmetric and symmetric. We set profiles with $\alpha > 3$ in our asymmetric Gaussian model (see Equation 4.3) as asymmetric profiles and sample from our posteriors in our error analysis. We find that 69±7% of our Lyα sample have asymmetric line profiles.

The shape of the profile emerging from the ISM/CGM affects the fraction of Lyα transmitted through the IGM (e.g., Dijkstra et al., 2011; Tang et al., 2024a), but can also reveal the impact of the IGM at $z \gtrsim 6$ as the IGM damping wing should produce smooth attenuation as a function of wavelength (Miralda-Escude, 1998), making profiles more symmetric. To test this, we explore the redshift evolution of asymmetry splitting our samples in two bins. We find the asymmetric fraction is 72±6% between $z = 5.2 - 5.8$, and 60±9% at $z = 5.8 - 6.4$. This is tentative evidence that profiles become more symmetric at $z > 5.8$, potentially due to the impact of the IGM damping wing, though the uncertainties are still large. Larger samples of Lyα line profiles would provide more insight into this effect.

In additional to the asymmetry, the distribution of $\mathrm{FWHM}_{\mathrm{Ly}\alpha}$ is a key uncertainty in reionization inferences (Mason et al., 2019), as it is an important factor in understanding non-detections: i.e. are Lyα detection rates lower at $z > 6$ because Lyα is intrinsically broader and thus more difficult to detect? (Section 4.3.1.1). We can address this in our sample by inferring the distribution of $\mathrm{FWHM}_{\mathrm{Ly}\alpha}$ at $z \sim 5-6$. In Figure 4.7 we show the distribution of $\mathrm{FWHM}_{\mathrm{Ly}\alpha}$ our sample. As the observed distribution looks log-normal, we fit the $\mathrm{FWHM}_{\mathrm{Ly}\alpha}$ sample with a log-normal distribution. The resulting distribution is shown in Figure 4.7, and is described by:

$$P(\log_{10}\mathrm{FWHM}_{\mathrm{Ly}\alpha}) = \mathcal{N}(\mu = 2.07^{+0.04}_{-0.04}, \sigma = 0.34^{+0.04}_{-0.03}) \tag{4.5}$$

Where μ is the mean and σ the standard deviation of the normal distribution of $\log_{10}(\mathrm{FWHM}_{\mathrm{Ly}\alpha})$. The mean of the log-normal distribution is 120 km s^{-1} on a linear scale. For comparison, we plot the model FWHM distribution predicted by Mason et al. (2019), based on a model for Lyα velocity offsets as a function of M_{UV}, and an empirical relation between $\mathrm{FWHM}_{\mathrm{Ly}\alpha}$ and $\Delta v_{\mathrm{Ly}\alpha}$ derived by Verhamme et al. (2018). We evaluate this model at the median M_{UV} and redshift of our Lyα detected galaxies. We find reasonable agreement with this model, although their median is slightly higher, with a peak at 155 km s^{-1}, we discuss the implications of this in Section 3.5.

To better understand what drives Lyα line shapes in our sample we compare $\mathrm{FWHM}_{\mathrm{Ly}\alpha}$ with galaxy properties. In Figure 4.8, we plot $\mathrm{FWHM}_{\mathrm{Ly}\alpha}$ versus M_{UV}, and $\mathrm{FWHM}_{\mathrm{H}\alpha}$ when available. Using the Pearson correlation coefficient we find a mild correlation (p-value ~ 0.1) of increasing $\mathrm{FWHM}_{\mathrm{Ly}\alpha}$ with M_{UV}, which we expect if M_{UV} traces galaxy mass and/or size (e.g., Shibuya et al., 2015; Roper et al., 2022; Allen et al., 2024; Morishita et al., 2024). $\mathrm{FWHM}_{\mathrm{Ly}\alpha}$ and $\mathrm{FWHM}_{\mathrm{H}\alpha}$ also shows a mild increasing correlation (p-value ~ 0.1). As the broadness of optical lines is correlated to galaxies dynamical mass (Binney, 2004; Erb et al., 2014), this may indicate enhanced resonant scattering of Lyα due to higher N_{HI}.

4.4.4 Lyα VELOCITY OFFSETS

For the 11 galaxies in our sample with both Lyα and systemic redshifts we can measure the velocity offset of Lyα from systemic, $\Delta v_{\mathrm{Ly}\alpha}$, which provides additional insight into the scat-

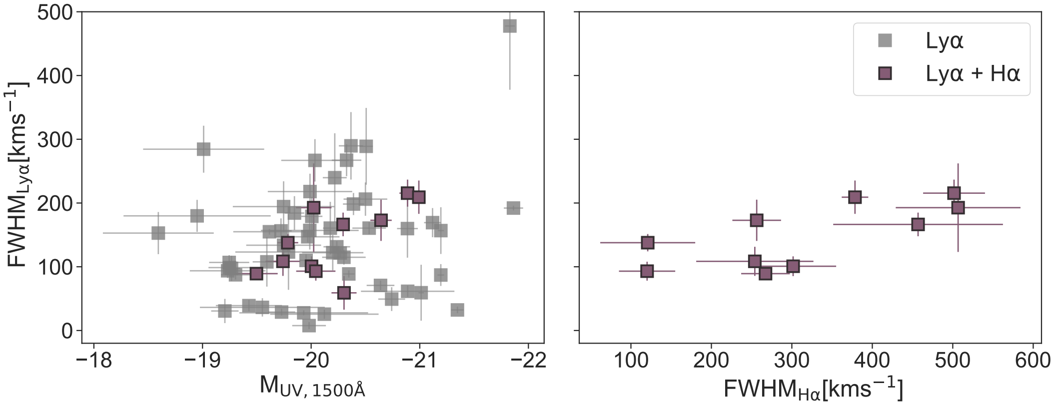

Figure 4.8: Left: FWHM$_{Ly\alpha}$ and M$_{UV}$. Right: FWHM$_{Ly\alpha}$ and FWHM$_{H\alpha}$. We show galaxies with only a Lyα emission (gray) and with Lyα +Hα emission (purple). We find a mild (p-value ∼ 0.1) correlations between FWHM$_{Ly\alpha}$ and M$_{UV}$, and between FWHM$_{Ly\alpha}$ and FWHM$_{H\alpha}$.

tering of Lyα in the ISM and CGM (Neufeld, 1991; Verhamme et al., 2008; Erb et al., 2014; Yang et al., 2017b):

$$\Delta v_{\mathrm{Ly}\alpha} = \mathrm{c}(\frac{z_{\mathrm{Ly}\alpha} - z_{\mathrm{sys}}}{1 + z_{\mathrm{sys}}}) \tag{4.6}$$

We measure $\mathrm{z_{lya}}$ from the peak of the Skewed Gaussian profile. To measure $\mathrm{z_{sys}}$, we follow the procedure described in Section 4.4.5. The uncertainty in $\Delta v_{\mathrm{Ly}\alpha}$ is mostly dominated by the uncertainties of the Lyα profile caused by the presence of strong sky-lines, though a few cases of weak Hα also add to the $\Delta v_{\mathrm{Ly}\alpha}$ uncertainty. For most measurements the error bars remain small, but nonetheless, we are limited by the spectral resolution of both Binospec and the NIRCam grism ($\sim 100\,\mathrm{km\,s^{-1}}$).

We show $\Delta v_{\mathrm{Ly}\alpha}$ as a function of UV magnitude for our sample in Figure 4.9. We compare our results to those in the reionization era (i.e., Bunker et al., 2023; Tang et al., 2023, 2024a, $z > 7.5$), mid redshift (i.e., Bradač et al., 2017; Stark et al., 2015; Willott et al., 2015; Inoue et al., 2016; Pentericci et al., 2016; Stark, 2016; Mainali et al., 2018; Cassata et al., 2020; Endsley et al., 2022b; Prieto-Lyon et al., 2023b, $4 < z < 7.5$), and low redshift (i.e., Steidel et al., 2014; Erb et al., 2014, $2 < z < 3$). We find a median and standard deviation (σ) $\Delta v_{\mathrm{Ly}\alpha}$ of $258 \pm 144\,\mathrm{km\,s^{-1}}$. By excluding $\Delta v_{\mathrm{Ly}\alpha} < 50\,\mathrm{km\,s^{-1}}$ results, we find a median and σ $\Delta v_{\mathrm{Ly}\alpha}$ of $315 \pm 125\ \mathrm{km\,s^{-1}}$. Both results are higher than the 205±75 measured in

$\mathrm{M_{UV}} > -19$ galaxies in Prieto-Lyon et al. (2023b) at $z \sim 3-5$. Our results are consistent with similar measurements at $z \sim 5-6$ by Tang et al. (2024a), who find a median and σ $\Delta v_{\mathrm{Ly}\alpha}$ =250 ± 156 km s^{-1} for galaxies in our same $\mathrm{M_{UV}}$ range ($\mathrm{M_{UV}} < -19.5$). Our new data spans a relatively narrow $\mathrm{M_{UV}}$ range, but combining with other samples at $z > 3$ referenced in the previous paragraph, we see a strong correlation of increasing $\Delta v_{\mathrm{Ly}\alpha}$ for higher UV luminosities (p-value«0.01). We also compare with the semi-empirical model from Mason et al. (2018a). We see most of the $z > 5$ data lie above the model, which was derived from a sample of $\mathrm{M_{UV}} < -19$ and $z \sim 2$ galaxies (Steidel et al., 2014; Erb et al., 2014).

Our sample includes two galaxies with extremely low $\Delta v_{\mathrm{Ly}\alpha} < 50$ km s^{-1} , z5-GND-17752 ($z = 5.77$) and z5-GND-39445 ($z = 5.50$), implying only minimal scattering in the ISM/CGM. We find that z5-GND-17752, our lowest $\Delta v_{\mathrm{Ly}\alpha}$ (20 km s^{-1}) measurement, also shows low $\mathrm{FWHM_{H\alpha}}$ (120 km s^{-1}). Looking at their Lyα line profiles (Appendix 4.9) we find significant emission bluewards of the Lyα peak, implying a highly ionized and/or low density sightline through the IGM enabling Lyα transmission around systemic velocity (Mason & Gronke, 2020). However, such low $\Delta v_{\mathrm{Ly}\alpha}$ is at the limit of the spectral resolution, making them susceptible to systematic errors.

We find no strong correlation between $\Delta v_{\mathrm{Ly}\alpha}$ and optical emission line broadness (Figure 4.9, p-value> 0.5). We further discuss implications of our $\Delta v_{\mathrm{Ly}\alpha}$ results on Lyα transmission in Section 3.5.

4.4.5 Lyα ESCAPE FRACTION

Lyα and Hα are both emitted predominantly in photoionized nebulae in a series of Hydrogen line transitions, or recombination cascades, therefore linking the production of both types of photons. The ratio of products of the recombination cascade depends on the electron temperature ($\mathrm{T_e}$) and electron number density ($\mathrm{n_e}$), but most importantly the optical depth of the medium (Dijkstra, 2014). In this work, we assume a Case-B recombination scenario, where the surrounding medium is optical thick to the Lyman series, as expected of HII regions, with $\mathrm{n_e} = 250\mathrm{cm}^{-3}$, $\mathrm{T_e} = 10^4$ (Dijkstra, 2014). This yields an intrinsic Lyα flux of $8.7\times$ the dust-corrected Hα flux.

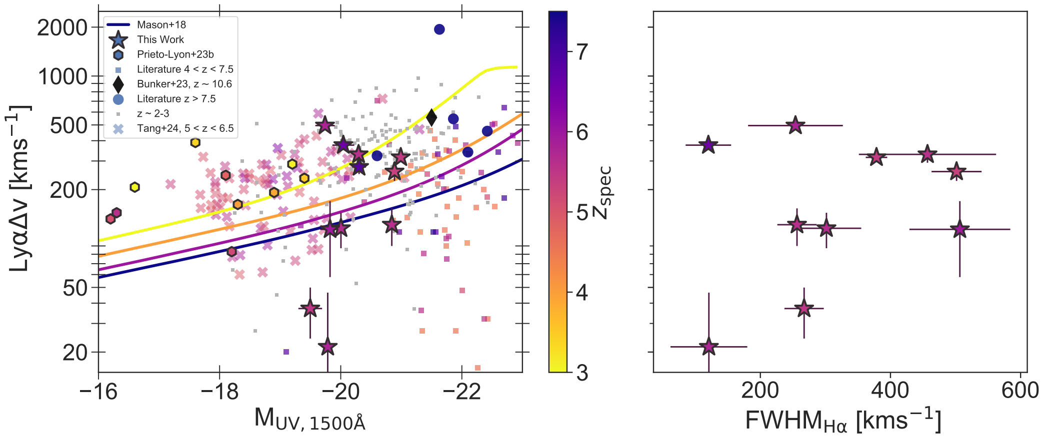

Figure 4.9: Left: Lyα velocity offset versus UV magnitude, with redshift as a color bar. Right: Lyα velocity offset and $\text{FWHM}_{\text{H}\alpha}$ in our sample. We show the data from this work as stars, and the UV-faint (z∼3-5) sample of Prieto-Lyon et al. (2023b) as circles. For reference we show a high redshift sample (i.e., Bunker et al., 2023; Tang et al., 2023, $z > 7.5$), mid redshift (i.e. (i.e., Bradač et al., 2017; Stark et al., 2015; Willott et al., 2015; Inoue et al., 2016; Pentericci et al., 2016; Stark, 2016; Mainali et al., 2018; Cassata et al., 2020; Endsley et al., 2022b; Tang et al., 2024a, $4 < z < 7.5$), and low redshift (i.e., Steidel et al., 2014; Erb et al., 2014, $2 < z < 3$). We add the semi-empirical model from Mason et al. (2018a). We see a slight increase of $\Delta v_{\text{Ly}\alpha}$ as UV luminosity increases, but we also find galaxies with low $\Delta v_{\text{Ly}\alpha}$. By joining our data with other works above $z > 3$ we find a strong increasing correlation (p-value$<< 0.01$). We see do not find a significant trend between Lyα velocity offset and $\text{FWHM}_{\text{H}\alpha}$.

The Lyα escape fraction is the ratio of the observed to intrinsic Lyα flux:

$$f_{\text{esc,ly}\alpha} = \frac{F_{\text{Ly}\alpha}}{8.7 F_{\text{dust corrected,H}\alpha}} \tag{4.7}$$

With both terms referring to the total flux of the emission lines (observed in the case of Lyα , dust-corrected in the case of Hα), and the 8.7 is the factor derived from case-B recombination. Recovering $f_{\text{esc}} < 1$ implies not all Lyα escapes from the galaxy, due to dust absorption or scattering by high column densities of neutral hydrogen, effectively removing Lyα from the line-of-sight.

We correct all Hα fluxes for dust attenuation following Lam et al. (2019b). We assume an SMC (Small Magellanic Cloud) dust curve (Prevot et al., 1984), which is expected to be similar to that in $z \sim 4 - 6$ galaxies based on the infrared excess (IRx) - β slope relationship (Bouwens et al., 2016a). The dust correction increases Hα fluxes by $\sim 1 - 10\%$. We propagate the uncertainty of β into the dust correction, though we find the error bars of f_{esc} are dominated by the uncertainty of the line fluxes in all cases.

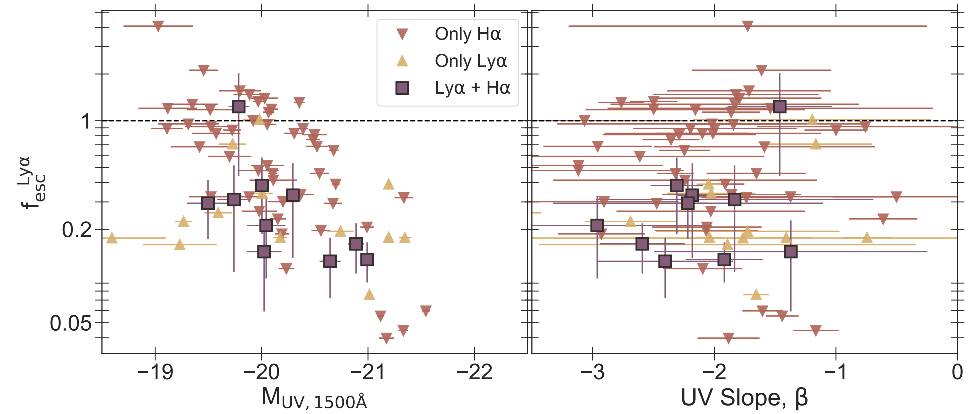

Figure 4.10: Left: M_{UV} and f_{esc} . Right : β and f_{esc} . We separate the sample into three types of measurements; galaxies with Lyα and Hα detections (purple), galaxies with only Hα detection as upper-limits (red) and galaxies with only Lyα detection as lower-limits (yellow). We find a strong trend (p-value$<$ 0.01) where galaxies have an increased f_{esc} the more UV-faint they are. For UV-slope, as in Figure 4.5, we do not find any clear trends.

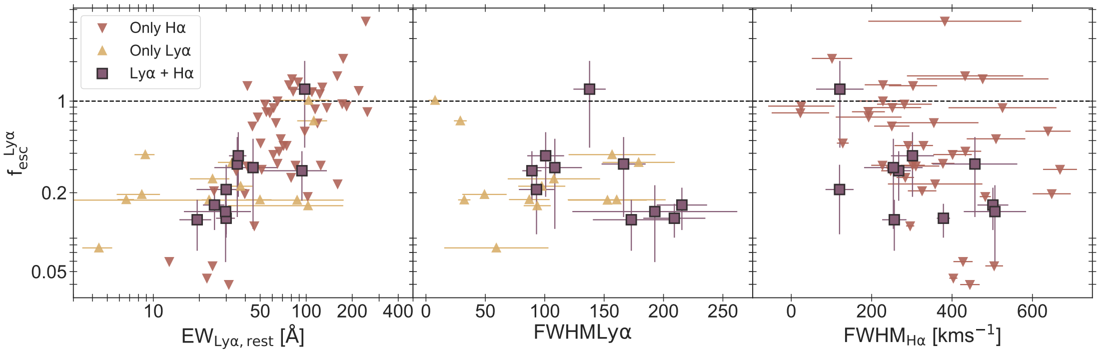

Figure 4.11: Escape fraction of Lyα against other Lyα properties. Left: f_{esc} and $EW_{Ly\alpha}$. Middle: f_{esc} and $FWHM_{Ly\alpha}$. Right f_{esc} and $FWHM_{H\alpha}$. The data shows an increase in $EW_{Ly\alpha}$ with higher f_{esc} , and an interesting population of weak Lyα with relatively high leakage ($f_{esc} > 0.2$). We find mild correlations (p-value$<$ 0.05) of higher f_{esc} with low $FWHM_{Ly\alpha}$ and low $FWHM_{H\alpha}$.

In Figure 4.10 we show the resulting Lyα escape fractions as a function of M_{UV} and β. We have three classes of measurements, galaxies with Hα emission only, galaxies with Lyα emission only, and galaxies with both Lyα and Hα . These classes produce upper limits, lower limits and measurements of $f_{\rm esc}$, respectively. For galaxies with only Hα , we use the Lyα flux limit as presented in Section 4.3.1.3 to obtain an upper limit on $f_{\rm esc}$. When only Lyα is present, we calculate Hα upper limits as the 5σ flux limit at the expected location of Hα , assuming $z_{\rm Ly\alpha}$, integrated in a width randomly drawn from our observed $\rm FWHM_{H\alpha}$ distribution. We use the median flux limit of 10,000 realizations for this method. Uncertainties in $f_{\rm esc}$ resulting from unknown Lyα velocity offsets are negligible. Our results in Figure 4.10 are dominated by upper-limits and lower-limits, to measure any correlations, we use a Pearson correlation coefficient, and do random draws from a uniform distribution between [0,upper-limit] and [lower-limit,1]. With 1000 iterations we find a strong increasing correlation between $f_{\rm esc}$ and $M_{\rm UV}$ (p-value< 0.01), while $f_{\rm esc}$ and UV slope show no trend.

In Figure 4.11 we compare $f_{\rm esc}$ with $\rm EW_{Ly\alpha}$, $\rm FWHM_{Ly\alpha}$, and $\rm FWHM_{H\alpha}$, using the same classification explained in the previous paragraph. Applying the random sampling method outlined in the previous paragraph, we identify mild correlations and anti-correlations (p-value < 0.05): $f_{\rm esc}$ increases with higher $\rm EW_{Ly\alpha}$ but decreases with both larger $\rm FWHM_{Ly\alpha}$ and $\rm FWHM_{H\alpha}$. Beyond the positive correlation between $f_{\rm esc}$ and $\rm EW_{Ly\alpha}$, we find a small population of sources with weak $\rm EW_{Ly\alpha} < 10$Å and $f_{\rm esc} > 0.1$, indicating a possible ISM configuration that allows weak Lyα to still escape from the galaxy. For Lyα broadness, we find a mild correlation of high $f_{\rm esc}$ in sources with narrow Lyα profiles, including two of the narrowest profiles in our sample, which exhibit $f_{\rm esc} \sim 1$. Similarly, comparing $f_{\rm esc}$ with $\rm FWHM_{H\alpha}$, we find that detections and upper limits generally show higher $f_{\rm esc}$ with narrower Hα profiles. We further discuss the implications of these correlations and anti-correlations in Section 3.5.

4.5 An empirical model for emergent Lyα

We now seek to build an empirical model to predict emergent Lyα properties based on easily observable galaxy properties, $M_{\rm UV}$ and UV slope β. In the following section we describe the approach we used to produce model distributions for both Lyα EW and $f_{\rm esc}$.

To estimate the Lyα EW and $f_{\rm esc}$ distributions we use a Bayesian approach (e.g., Treu et al., 2012; Schenker et al., 2014; Oyarzún et al., 2017; Mason et al., 2018a; Tang et al., 2024a) which allows to obtain the posterior distribution of the parameters that describe the $\mathrm{EW}_{\mathrm{Ly}\alpha}$ and f_{esc} distributions. We follow Mason et al. (2018a) and assume the distributions for EW and f_{esc} are described by an exponential with a potential peak at zero for non-emitters, with two parameters $\theta = (A, X_0)$. We note that previous work has shown the exact form of the distributions (exponential, log-normal etc.) does not significantly impact results (Schenker et al., 2014; Oyarzún et al., 2017; Tang et al., 2024a). In the following we use X to denote the 'data' EW or f_{esc} as we model both distributions in the same way. The model distribution is:

$$p(X|\theta = \{A, X_0\}) = B\frac{A}{X_0}e^{-X/X_0}\mathrm{H}(X) + (1-A)\delta(X) \tag{4.8}$$

The parameter X_0 represents the scale length of the exponential, and A is a normalization term which represents the fraction of Lyα emitters (i.e. the fraction of galaxies which have EW or $f_{\mathrm{esc}} > 0$). B is a normalization term for the distribution given the limits of EW and f_{esc} ($B = 1$ for EW, and $B = 1/(1-\exp(-1/X_0))$ for f_{esc}). $H(X)$ is the Heaviside function and $\delta(X)$ is the Dirac-delta function.

We assume Gaussian measurement uncertainties with standard deviation σ on our data X_{obs} for each galaxy such that:

$$p(X_{\mathrm{obs}}|X) = \frac{1}{\sqrt{2\pi}\sigma}\exp\left[-\frac{(X - X_{\mathrm{obs}})^2}{2\sigma^2}\right] \tag{4.9}$$

Thus the likelihood for an individual observation is:

$$p(X_{\mathrm{obs}}|\theta) = \int dX p(X_{\mathrm{obs}}|X)p(X|\theta) \tag{4.10}$$

Where the limits of integration are $[0, \infty]$ for $\mathrm{EW}_{\mathrm{Ly}\alpha}$ and [0,1] for f_{esc} .

Convolving our likelihood with the Gaussian distribution and solving the integral, we obtain the likelihood for our observations:

$$\begin{aligned} p(X_{\rm obs}|\theta) = B\frac{A}{2X_0}e^{\frac{\sigma^2-2X_0X_{\rm obs}}{2X_0^2}}\left[\mathrm{erf}\left(Z+\frac{X_{\rm max}}{\sqrt{2}\sigma}\right)-\mathrm{erf}(Z)\right] \\ +\frac{(1-A)}{\sqrt{2\pi}\sigma}e^{-\frac{X_{\rm obs}^2}{2\sigma^2}}. \\ \text{Where } Z = \frac{1}{\sqrt{2}\sigma}\left(\frac{\sigma^2}{X_0}-X_{\rm obs}\right) \end{aligned} \tag{4.11}$$

Where *erf* is the error function, and $X_{\rm max}=\infty$ for EW and 1 for $f_{\rm esc}$.

For galaxies with Lyα non-detections (i.e. upper limits in $\mathrm{EW}_{\mathrm{Ly}\alpha}$ and $f_{\rm esc}$) the likelihood is:

$$p(X_{i,\rm obs}|\theta) = p(X_{i,\rm obs} < X_{\rm uplim}|\theta) \tag{4.12}$$

Where the cumulative distribution function is obtained by integrating $p(X_{i,\rm obs}|\theta)$ (Equation 4.10) from $x_{i,\rm obs}=-\infty$ to $x_{\rm uplim}$.

For galaxies with no Hα detection we have only a lower limit on $f_{\rm esc}$, thus in those cases the likelihood is:

$$p(X_{i,\rm obs}|\theta) = p(X_{i,\rm obs} > X_{\rm lowlim}|\theta) \tag{4.13}$$

Where we integrate $p(X_{i,\rm obs}|\theta)$ from $X_{\rm lowlim}$ to 1.

The final posterior is the product of all individual galaxy posteriors: $p(\theta|\{X_{\rm obs}\} \propto p(\theta)\prod_i p(X_{i,\rm obs}|\theta)$. We assume flat priors on A and X_0: $A\in[0,1]$, $W_0\in[0,500]$ and $f^{\mathrm{Ly}\alpha}_{\rm esc,o}\in[0,1]$.

4.5.1 Dependence of the distributions on galaxy properties

To better understand the dependence of Lyα emission on galaxy properties we parameterise our model as a function of $\mathrm{M_{UV}}$ and β. Previous work, and our results in Section 4.4, have demonstrated that Lyα EW and escape may be enhanced in UV-faint, bluer, galaxies (e.g., Tang et al., 2024a; Oyarzún et al., 2017).

We follow the approach done by Oyarzún et al. (2017) and parameterise our model parameters A and X_0 as a linear combination of $\mathrm{M_{UV}}$ and β.

$$\begin{aligned} A &= A_{\mathrm{M_{UV}}}\mathrm{M_{UV}} + A_\beta \beta + A_c \\ X_0 &= X_{\mathrm{M_{UV}}}\mathrm{M_{UV}} + X_\beta \beta + X_c \end{aligned} \tag{4.14}$$

To compute the posterior distributions, we follow the same method as before, assuming the same priors on A and X_0.

We perform tests to mock dataset to assess whether our sample size is sufficient to robustly recover these parameters. We find that our Lyα EW sample (236 galaxies, including 65 Lyα detections) is large enough that we expect to recover the parameters in Equation 4.14 within 5-30% of the *true* parameters. We find our f_{esc} sample (72 galaxies, including 10 Lyα +Hα detections) is not large enough to fit the linear model robustly, so we assume constant A and X_0, and find we can recover these robustly when splitting our sample into two bins. Both A and X_0 are recovered with similar accuracy and precision in our tests.

4.5.2 Lyman Alpha Equivalent Width Model

As described above we will fit for the Lyα EW distribution assuming an exponential model with parameters described by a linear model in $\mathrm{M_{UV}}$ and β (Equation 4.14). We use the measured EW, uncertainties and 5σ upper limits, as described in Section 4.4.2, in our likelihood (Equation 4.11), accounting for uncertainties in $\mathrm{M_{UV}}$ and β for each galaxy by sampling from their posteriors (Section 4.4.1). We perform the fitting using an MCMC with `emcee` (Foreman-Mackey et al., 2013) with 10,000 steps and 25 walkers, enough to reach convergence. We find that our model clearly returns $A \approx 1$, i.e. a purely exponential distribution with no peak at EW$= 0$ Å. Thus we fit only for the scale-length $X_0 \equiv EW_0$.

We show the resulting corner plots for the EW_0 parameters in Figure 4.12. We find that our model is completely described by $\mathrm{M_{UV}}$, with the UV slope having a weak dependence within 1σ of 0. This lack of correlation with the UV slope is likely due to our source selection, as discussed further in 4.6.1. Consequently, we opt to re-run the model excluding the UV

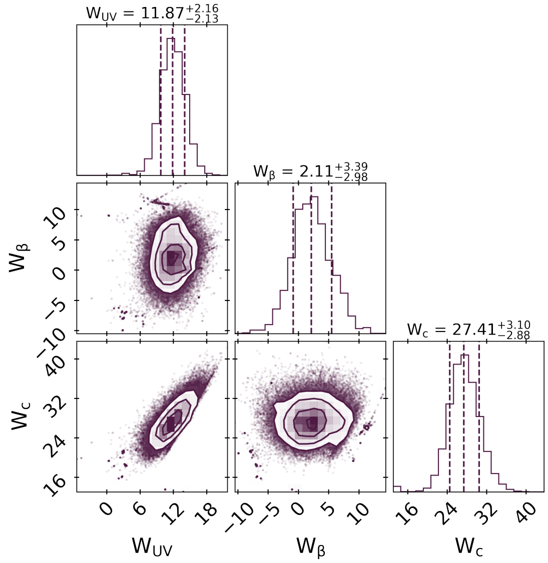

Figure 4.12: Corner plot for the MCMC run explained in our methods. The three posterior distributions shown correspond to W_o dependence on M_{UV} , UV-slope, and a constant value that encapsulates other possible sources of correlation. Posterior distributions shows correlation between W_{UV} and W_c.

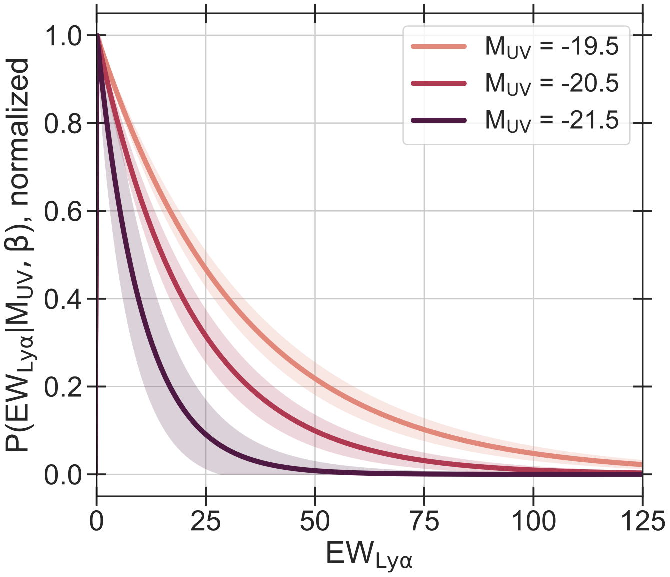

Figure 4.13: Probability distribution of $EW_{Ly\alpha}$. We plot 3 distributions for different M_{UV} within our data range. The Lyα emitter fraction $p(EW_{Ly\alpha} > 25Å)$ is low for UV bright (M_{UV} = -21.5) galaxies (8%), while for UV-faint (M_{UV} = -19.5) sources it reaches 45%.

slope. The inferred scale-length is:

$$EW_0 = 11.2^{+2.0}_{-2.0} \cdot (\mathrm{M_{UV}} + 20) + 27.2^{+3.1}_{-2.8} \tag{4.15}$$

Where we give the median and 68% credibile intervals for each parameter given their posterior distributions.

In Figure 4.13 we visualize the normalized $\mathrm{EW_{Ly\alpha}}$ distribution. We show the resulting distribution for 3 examples with $\mathrm{M_{UV}} = -19.5, -20.5, -21.5$. We plot the median and 68% credible interval of the distributions obtained by sampling from the posterior predictive distributions for the EW_0 parameters. We see that faint galaxies have a broader EW distribution than bright galaxies, and therefore much higher likelihood of having a strong $\mathrm{EW_{Ly\alpha}}$ as discussed in the next paragraph.

Using our EW distribution model we can also calculate the 'Lyα fraction': the fraction of Lyman-break galaxies with EW> 25 Å (e.g., Stark et al., 2010). We obtain this by integrating Equation 4.8 given our inferred parameters in Equation 4.15. For the three cases shown in Figure 4.13 the Lyα fraction ranges from 8 to 45% (±5%) for $\mathrm{M_{UV}} = -21.5$ to $\mathrm{M_{UV}} = -19.5$. Assuming the most commonly used UV magnitude range in the literature ($-18.75 < \mathrm{M_{UV}} < -20.25$, i.e. median $\mathrm{M_{UV}} = -19.5$) we find a Lyα fraction of 45%$\pm$5%, consistent with recent findings by Tang et al. (2024a) of 35±7%. Based on our distributions, we expect 21 ± 3% of $\mathrm{M_{UV}} = -19.5$ galaxies to show $\mathrm{EW_{Ly\alpha}} > 50$Å, consistent with Tang et al. (2024a), and 5 ± 2% to show $\mathrm{EW_{Ly\alpha}} > 100$Å, 2σ lower than Tang et al. (2024a). Overall, we should expect a non-negligible fraction of very strong emitters as we move deep into the reionization era where $\mathrm{M_{UV}} > -19.5$ galaxies become more common.

4.5.3 Lyman Alpha Escape Fraction Model

As our sample of sources with f_{esc} measurements is not large enough to fit the linear model (Equation 4.14), we fit the f_{esc} distribution assuming constant parameters A and X_0 in two bins. We create two UV magnitude bins: UV-faint ($\mathrm{M_{UV}} > -20.1$), UV-bright ($\mathrm{M_{UV}} < -20.1$); and two UV slope bins: red ($\beta > -2.0$) and blue ($\beta < 2.0$). These bins are defined so each contains the same number of sources.

We infer the parameters A and X_0 in our 4 sub-samples and give the resulting inferred pa-

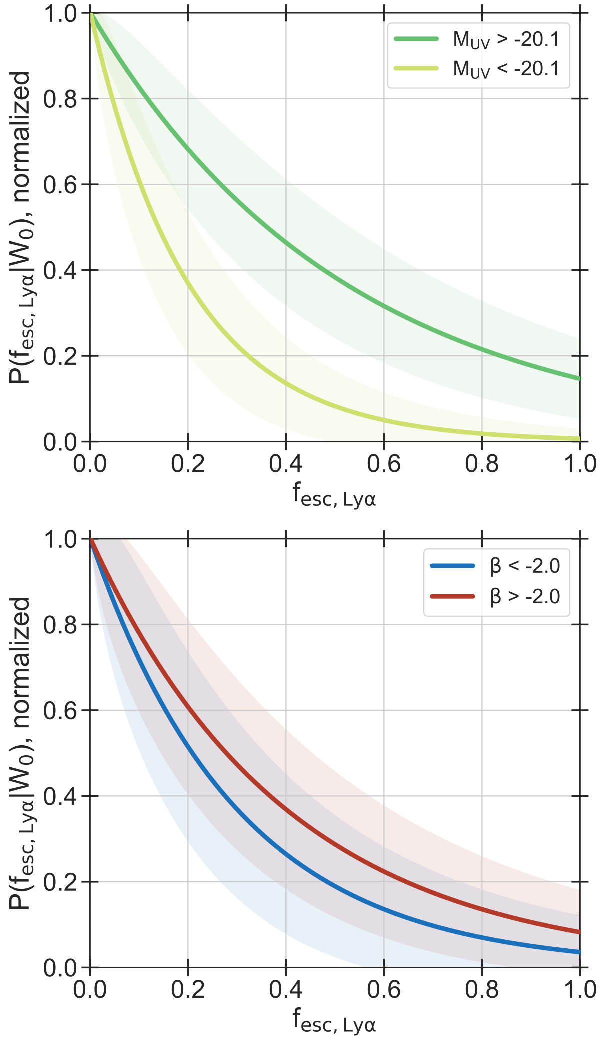

Figure 4.14: Probability distributions of observed f_{esc} . Results are obtained by binning the dataset in M_{UV} and UV slope separately. As in our $EW_{Ly\alpha}$ results, we find that the model is dominated by M_{UV} , while the two UV slope scenarios are not statistically different.

Sub-sample	X_0	A
All	$0.27^{+0.16}_{-0.08}$	$> 0.99^*$
$M_{UV} >$ -20.1	$0.52^{+0.23}_{-0.22}$	$> 0.98^*$
$M_{UV} <$ -20.1	$0.20^{+0.09}_{-0.05}$	$> 0.98^*$
$\beta >$ -2.0	$0.40^{+0.27}_{-0.17}$	$> 0.97^*$
$\beta <$ -2.0	$0.28^{+0.16}_{-0.08}$	$> 0.99^*$

Table 4.2: Results for exponential (X_0) and delta (A) parameters for the four f_{esc} bins. Results shown are the posterior's median, 16th and 84th percentile values. *For lower limits we give the 68% limit.

rameters in Table 4.2. We show the inferred distributions in Figure 4.14. We recover median f_{esc} =0.18 ± 0.6 in the full sample. Again, we find a delta function at f_{esc} = 0 is disfavored.

We find the probability of high f_{esc} increases dramatically from UV bright to UV faint galaxies. Between the two M_{UV} samples, we find median f_{esc} goes from 0.13 ± 0.05 in UV-bright galaxies to 0.28 ± 0.8 in UV-faint galaxies. From our UV-faint bin we obtain that $62 \pm 8\%$ of $M_{UV} > -20.1$ galaxies have $f_{esc} > 0.2$. This is considerably higher than the $30 \pm 6\%$ found by Tang et al. (2024a) for $M_{UV} \sim -19.5$. We attribute this difference to our high upper limits on f_{esc} which do not significantly constrain our models and the use of a uniform prior on f_{esc} . If we decrease our Lyα flux limits by a factor $2(4)$, we obtain $50 \pm 12\%$ ($35 \pm 10\%$) of $M_{UV} > -20.1$ galaxies have $f_{esc} > 0.2$, demonstrating the sensitivity of the inference to upper limits. Thus we consider our reported distribution an upper limit on the underlying distribution.

We do not find significant difference between the f_{esc} distributions binned by UV slope. Previous works (Tang et al., 2024a; Chen et al., 2024) have shown that f_{esc} strongly correlates with UV slope, but we do not see this effect in our sample (see also Figure 4.10). This is likely due to our target selection which is incomplete for blue ($\beta \lesssim -2$) $M_{UV} < -19.5$ galaxies (see discussion in Section 4.6.1).

4.6 Discussion

In this paper we have presented new measurements and models of Lyα for Lyman-Break selected galaxies at $z \sim 5-6$. In Sections 4.4 and 4.5 we have connected the shape and strength of the Lyα line with other physical properties such as $\mathrm{M_{UV}}$ and optical line broadness. In the following discussion, we explore the implications of our findings for predicting Lyα emission emerging from the ISM/CGM, as well as the impact of this transmission on its observability during the epoch of reionization.

4.6.1 Predicting Lyα transmission from the ISM/CGM at $z \sim 5-6$

The main goal of this paper was to build a predictive model for Lyα at the end of reionization, providing a basis to better interpret Lyα observations at $z > 6$. These baseline observations are important due to the degeneracy between scattering of Lyα by neutral hydrogen in the IGM and ISM/CGM during the EoR. In particular, we focused on Lyα line shape and strength properties, including $\mathrm{FWHM_{Ly\alpha}}$, $\Delta v_{\mathrm{Ly}\alpha}$, $\mathrm{EW_{Ly\alpha}}$ and f_{esc} . In this section we discuss their trends with physical galaxy properties, $\mathrm{M_{UV}}$, UV slope and optical emission line broadness. Finally, we explore the possible physical drivers behind these trends and how they can be used to better predict Lyα at $z > 6$.

In Section 4.4.3 we showed that Lyα lineshape properties: $\Delta v_{\mathrm{Ly}\alpha}$ and $\mathrm{FWHM_{Ly\alpha}}$, have tentative correlations with $\mathrm{M_{UV}}$ and optical line FWHM. In Figure 4.9, when adding our $\Delta v_{\mathrm{Ly}\alpha}$ results with similar works at $z > 3$ (i.e. Bradač et al., 2017; Stark et al., 2015; Willott et al., 2015; Inoue et al., 2016; Pentericci et al., 2016; Stark, 2016; Mainali et al., 2018; Cassata et al., 2020; Endsley et al., 2022b; Bunker et al., 2023; Tang et al., 2023; Prieto-Lyon et al., 2023b; Tang et al., 2024a) they show a strong correlation of increasing $\Delta v_{\mathrm{Ly}\alpha}$ with higher UV luminosity. We have also found mild correlations of increased $\mathrm{FWHM_{Ly\alpha}}$ in UV bright galaxies and in galaxies with broader optical emission lines. It has been shown in previous works (e.g. Neufeld, 1991; Verhamme et al., 2006) that broader Lyα profiles and higher $\Delta v_{\mathrm{Ly}\alpha}$ are byproducts of increased Lyα resonant scattering events. The trends we find of increasing $\Delta v_{\mathrm{Ly}\alpha}$ and $\mathrm{FWHM_{Ly\alpha}}$ with UV luminosity and/or high optical line FWHM are consistent with the physical picture of more massive, and spatially extended galaxies, having increased resonant scattering events. This scenario is supported by observations and simulations, which show that a galaxy's size and effective radius is strongly correlated with increasing UV luminosity (e.g., Shibuya et al., 2015; Roper et al., 2022; Morishita et al., 2024). Additionally, optical line broadness has been shown to increase with galaxy dynamical mass (Binney, 2004; Erb et al., 2014). Together, larger sizes and masses of galaxies should lead to higher HI column densities (N_{HI}), where N_{HI} is the main driver of increased resonant scattering of Lyα in the ISM/CGM (Dijkstra, 2014; Verhamme et al., 2015). Our results have made another step toward using UV properties and optical line properties to better predict emergent Lyα in galaxies at $z > 6$. We have shown optical line FWHM, for which samples are steadily increasing with JWST, could be a promising way to predict Lyα lineshapes during the reionization era. Furthermore, the higher velocity offsets compared to $z \sim 2$ samples can boost Lyα transmission through the IGM, which we will further discuss in Section 4.6.2 (see also, Tang et al., 2024c).

In Section 4.5.2, we showed that $EW_{Ly\alpha}$ and f_{esc} strongly correlate with increasing UV luminosity. Additionally, we identified a strong correlation between increasing f_{esc} and $EW_{Ly\alpha}$. We also showed that f_{esc} increases as Lyα and optical lines become narrower. These findings are consistent with previous studies, where $EW_{Ly\alpha}$ and f_{esc} have an enhanced probability of being stronger in galaxies that are UV faint and bluer (Oyarzún et al., 2017; Tang et al., 2024a). However we find no strong trends with UV slope in our sample. As discussed by Tang et al. (2024a), the strong correlation of increasing $EW_{Ly\alpha}$ and f_{esc} suggests that strong $EW_{Ly\alpha}$ requires an environment capable of high f_{esc} . This is consistent with the same scenario as in the previous paragraph, where increased resonant scattering events are more common in UV bright galaxies that tend to have larger sizes and masses. We then expect UV bright galaxies to have a shorter mean-free path between scattering events, leading to higher probability of Lyα being destroyed by dust (Dijkstra, 2014) and therefore reduced f_{esc} . The aforementioned link between Lyα strength and the properties of the ISM/CGM suggest that $EW_{Ly\alpha}$ and f_{esc} can be predicted using non-Lyα observables at $z > 6$. This implication is supported by our results, which, consistent with previous studies (Tang et al., 2024a; Chen et al., 2024; Lin et al., 2024), show that Lyα strength can be inferred from UV observables, and tentatively also through optical line broadness. Both M_{UV} and optical line broadness are detectable through JWST, even at the highest redshifts ([OIII] up to z$\sim$9). Our measurements and models have shown their potential as a powerful tool for estimating emergent

Lyα strength for galaxies during the EoR.

Our measurements in Figures 4.5 and 4.10 show no robust trends of $EW_{Ly\alpha}$ and f_{esc} with UV slope. The same is true when retrieving the posterior distributions of our $EW_{Ly\alpha}$ and f_{esc} empirical models in Section 4.5.2 and 4.5.3. Overall, we find no significant dependencies of the two models with UV slope. Nonetheless, previous works have found that Lyα is strongly enhanced in galaxies with bluer UV continuum (Oyarzún et al., 2017; Tang et al., 2024a; Lin et al., 2024). We attribute this missing trend to a lack of galaxies that are UV faint, high $EW_{Ly\alpha}$ and blue ($\beta < -2$), arising from our target selection, magF160W < 27.5 (see Section 4.2.1) which results in a lack of $M_{UV} > -19.5$, blue galaxies. We tested this by comparing our sample in M_{UV} and UV slope against the JADES-DJA photometric catalogs. We find that imposing a magF160W < 27.5 cut for galaxies within $5 < z_{phot} < 6.5$ in the JADES-DJA catalog does biases against blue UV slopes for $M_{UV} \gtrsim -19.5$ galaxies. At $M_{UV} > -19.5$ we find median $\beta = -1.6$ in our data, while the full JADES-DJA sample finds $\beta = -2.2$. If we apply the magF160W < 27.5 cut to JADES-DJA, the median UV slopes also becomes $\beta = -1.6$. As the faintest, bluest galaxies typically have strongest Lyα emission (Oyarzún et al., 2017; Tang et al., 2024a; Lin et al., 2024) we attribute our lack of trends of $EW_{Ly\alpha}$ and f_{esc} with UV slope to our sample incompleteness. Omitting sources with $M_{UV} > -19.5$ from our $EW_{Ly\alpha}$ and f_{esc} models does not significantly impact our results.

4.6.2 IMPLICATIONS FOR LYα OBSERVABILITY DURING REIONIZATION

Our primary goal was to better understand the typical emergent Lyα emission as it leaves the ISM/CGM in high-redshift galaxies. As the effects of HI in the IGM and ISM/CGM over Lyα are entangled at the EoR, we must separate between the emergence of Lyα from galaxies and its absorption caused by the damping wing of the IGM (Miralda-Escude, 1998; Dijkstra et al., 2007, 2011; Mason et al., 2018a). With this goal, we have produced baseline measurements with observations at $z \sim 5-6$. Our observations at the end of EoR, allow us to isolate the effects of the ISM/CGM over Lyα , and to better infer the reionization timeline in the future.

With $R \sim 4000$ resolution and observations of up to 15 hours, we have made the first statistical measurement of the $\mathrm{FWHM}_{\mathrm{Ly}\alpha}$ distribution at $z \sim 5-6$, previously limited to bright sources and stacked profiles (e.g., Pentericci et al., 2018). We found in Section 4.4.3 that our $\mathrm{FWHM}_{\mathrm{Ly}\alpha}$ distribution is comparable, indeed slightly lower, than the predictions of Mason et al. (2019). $\mathrm{FWHM}_{\mathrm{Ly}\alpha}$ and $\Delta v_{\mathrm{Ly}\alpha}$ play a key role on the Lyα detection rate once the IGM becomes sufficiently neutral at $z \gtrsim 6$, as both properties shift Lyα closer or further from its resonant wavelength. Therefore, we must understand to what extent the Lyα transmission drop past $z \gtrsim 6$ is purely due to the IGM damping wing, or to the emergent line properties of Lyα . The $\mathrm{FWHM}_{\mathrm{Ly}\alpha}$ has two opposing effects over the observability of Lyα : First, a broader line profile will more easily transmit through the IGM due to more flux being redwards of Lyα at lower optical depths (Prieto-Lyon et al., 2023b; Mukherjee et al., 2024; Yuan et al., 2024). For the second effect, a broader profile will lead to the same flux being spread over a longer wavelength range, hindering its detection in flux-limited observations. In contrast to $\mathrm{FWHM}_{\mathrm{Ly}\alpha}$, increased $\Delta v_{\mathrm{Ly}\alpha}$ will always boost Lyα transmission through the IGM by shifting Lyα to redder wavelengths with lower optical depths. The mild correlation of smaller $\mathrm{FWHM}_{\mathrm{Ly}\alpha}$ in UV faint galaxies found in Figure 4.8 implies that: UV faint galaxies which are prevalent at higher redshifts, should have narrow profiles and thus be more easily detectable for lower Lyα fluxes.

To assess the impact of the lineshape on reionization analyses we compare our lineshape with the assumptions by Mason et al. (2018a, 2019) in their neutral fraction inference. Given our median $\mathrm{FWHM}_{\mathrm{Ly}\alpha}$, we find $\sim 1.4\times$ tighter lower limits on the IGM neutral fraction at $z \sim 8$ by Mason et al. (2019) which assumed a higher $\mathrm{FWHM}_{\mathrm{Ly}\alpha}$ (see their Figure C1), as non-detections become more significant, implying a higher IGM attenuation. We further compare the IGM Lyα transmission for an $\mathrm{M}_{\mathrm{UV}} = -20$ galaxy at $z = 9$ using our median line profile and the model by Mason et al. (2018a). We assume a completely neutral IGM, in a region without ionized bubbles (using the approximation by Dijkstra, 2014). The transmitted Lyα using our line shape median values (Gaussian, with $\mathrm{FWHM}_{\mathrm{Ly}\alpha} = 120\,\mathrm{km\,s^{-1}}$, $\Delta v_{\mathrm{Ly}\alpha} = 258\,\mathrm{km\,s^{-1}}$) is $5\times$ higher than that predicted by Mason et al. (2019) (Gaussian $\mathrm{FWHM}_{\mathrm{Ly}\alpha} = 160\,\mathrm{km\,s^{-1}}$ $\Delta v_{\mathrm{Ly}\alpha} = 150\,\mathrm{km\,s^{-1}}$, and truncated at 80 km/s due to infalling IGM) – finding 0.6% vs 0.1% transmission respectively, though the difference in transmission is negligible for bubbles $R \gtrsim 1$ pMpc.

We also examine how the strongly asymmetric shape of Lyα should facilitate Lyα transmission in a mostly neutral IGM. For the 11 sources in our sample with measured velocity offsets we calculate the fraction of flux at $\Delta v_{\mathrm{Ly}\alpha} > 400$ km/s, which can be transmitted even in a neutral IGM (Dijkstra et al., 2011; Mason et al., 2018b; Yuan et al., 2024). We obtain a median and standard deviation of 22$\pm$18% from this sample, agreeing closely with recent results from hydrodynamical radiative transfer simulations by Yuan et al. (2024).

The higher transmission for Lyα which is both more offset from systemic and has extended red wings implies Lyα can be visible even in a very neutral IGM (Dijkstra et al., 2011; Witstok et al., 2024c). These results suggest we may require a higher neutral fraction at $z \gtrsim 8$ to explain the Lyα decline compared to analyses which use $z \sim 2$ lineshapes as a baseline, demonstrating $z \sim 5-6$ samples such as these will be important to include in future reionization inferences (see also, Tang et al., 2024a,c; Yuan et al., 2024).

4.7 CONCLUSIONS

A detailed understanding of Lyα as it emerges from galaxies in the first billion years is critical for interpreting Lyα observations during the reionization era. Our main goal was to produce empirical baseline models and correlations of Lyα to better constraint reionization history. We have presented an analysis of Lyman-break galaxies at $z \sim 5-6$, in a mostly ionized IGM. With our new ground-based Lyα spectra, supplemented by JWST imaging and spectra, we have studied the correlations between Lyα shape and strength with other physical properties, such as UV luminosity and optical line broadness. We conclude the following:

1. We present high-resolution MMT/Binospec restframe-UV spectroscopy for 236 targets. We detect Lyα at S/N$>$ 5 for 65 of these, with a median 5σ flux limit of $1.34x10^{-17}$ erg s^{-1} cm^{-2}. Overlapping ancilliary NIR spectra from JWST/NIRCam - FRESCO allows us to measure z$_{\mathrm{sys}}$ for 51 of our targets.

2. With $R \sim 4600$ we measure Lyα line profiles with a high-resolution of $\sim$ 70 km s^{-1} . We measured for the first time the FWHM$_{\mathrm{Ly}\alpha}$ distribution at $z \sim 5-6$, a key unknown quantity in interpreting the decline of Lyα at $z > 6$. Our modeled distribution shows mean FWHM$_{\mathrm{Ly}\alpha}$ =120 km s^{-1} , slightly lower, but consistent, with models based on

$z \sim 2$ Lyα observations (Mason et al., 2019).

3. We obtain 11 new measurements of Lyα velocity offsets at $z > 5$ through systemic redshifts from Hα or [OIII] from FRESCO NIRCam slitless spectra. We reported correlations between physical properties and Lyα lineshape: $\Delta v_{\mathrm{Ly}\alpha}$ and FWHM$_{\mathrm{Ly}\alpha}$. We find that he majority of galaxies show $\Delta v_{\mathrm{Ly}\alpha} \gtrsim 100$ km s^{-1}, with a median 258 km s^{-1}. Combined with $z > 3$ data from the literature, we find a very strong correlation for increased $\Delta v_{\mathrm{Ly}\alpha}$ in UV bright galaxies. We found mild correlations of higher FWHM$_{\mathrm{Ly}\alpha}$ in galaxies that are UV-bright and/or have broad optical lines. Our lineshape trends are consistent with an scenario of high Lyα optical depth, with numerous scattering events in the ISM/CGM. Overall, we find that our median $\Delta v_{\mathrm{Ly}\alpha}$ and FWHM$_{\mathrm{Ly}\alpha}$ are respectively higher and lower than those used by reionization models calibrated with Lyα observations at $z \sim 2$ (Mason et al., 2018a, 2019). The higher observed velocity offsets result in higher Lyα transmission: given our median $\Delta v_{\mathrm{Ly}\alpha}$ and FWHM$_{\mathrm{Ly}\alpha}$ measurements, Lyα can boosted up to $5\times$ in a neutral IGM relative to $z \sim 2$ lineprofiles. This could imply a more neutral IGM at $z > 8$ than inferred from models using $z \sim 2$ lineprofiles.

4. We measured line strength properties: EW$_{\mathrm{Ly}\alpha}$ and f_{esc}. We found strong correlations of EW$_{\mathrm{Ly}\alpha}$ and f_{esc} with increasing UV luminosity, and mild correlations of increasing f_{esc} with higher FWHM$_{\mathrm{Ly}\alpha}$ and optical line FWHM. The decline of f_{esc} with line broadness and UV luminosity is consistent with an scenario of higher Lyα optical depth in UV bright galaxies.

5. We created an empirical model for the probability distribution of EW$_{\mathrm{Ly}\alpha}$ and f_{esc} at the end of EoR, as a function of M$_{\mathrm{UV}}$ and UV slope. Our EW$_{\mathrm{Ly}\alpha}$ and f_{esc} models strongly depend on M$_{\mathrm{UV}}$. We find strong EW$_{\mathrm{Ly}\alpha}$ ($>$ 25 Å) and f_{esc} ($>$ 0.2) are common at $z \sim 5-6$: Our models predict that 45±5% and $< 62 \pm 8$% of$\mathrm{M}_{\mathrm{UV}} = -19.5$ galaxies have EW$_{\mathrm{Ly}\alpha} > 25$ Å and $f_{\mathrm{esc}} > 0.2$.

The NIR capabilities of JWST have enabled us to unlock new information about emergent Lyα through rest-frame optical emission lines (Hα and [OIII]): $\Delta v_{\mathrm{Ly}\alpha}$, f_{esc} and optical line broadness. With our high-resolution Lyα observations, we have made the first steps on studying trends of Lyα shape and strength with optical observables. As optical line samples at $z \sim 5-9$ grow steadily by the 100s (e.g. Covelo-Paz et al., 2024; Meyer et al., 2024), we will be able to better constrain the emergent trends of Lyα and optical line broadness at $z \sim 5-6$, and predict Lyα shape and strength for Lyα non-detections at the EoR. Additionally, the unprecedented detections of Lyα at $z \sim 9-13$ (Bunker et al., 2023; Witstok et al., 2024b,c) will offer completely new constraints on reionization. Baseline Lyα empirical correlations and models, like the ones we have presented, combined with observations of Lyα and optical emission lines at the EoR, will be crucial for constraining the reionization process.

We thank Igor Chilingarian, Sean Moran for their initial reductions and advice regarding the Binospec pipeline, and Dan Fabricant and Ben Weiner for their advice in planning Binospec observations. GPL and CAM acknowledge support by the VILLUM FONDEN under grant 37459. CAM acknowledges support from the Carlsberg Foundation under grant CF22-1322. The Cosmic Dawn Center (DAWN) is funded by the Danish National Research Foundation under grant DNRF140.

4.8 Lyα Detections

ID	RA	DEC	$z_{\mathrm{Ly}\alpha}$	z_{sys}	M_{UV}	β	$\mathrm{EW}_{\mathrm{Ly}\alpha}$ [Å]	$\mathrm{FWHM}_{\mathrm{Ly}\alpha}$ [km s^{-1}]	$\mathrm{FWHM}_{\mathrm{H}\alpha}$ [km s^{-1}]	f_{esc}	$\Delta v_{\mathrm{Ly}\alpha}$ [km s^{-1}]
z5-GNW-1503	189.139303	62.111230	5.0508	–	-20.9 ± 0.1	-1.9 ± 0.4	8 ± 3	160 ± 46	–	–	–
z5-GNW-12024	189.142960	62.179790	5.1661	–	-18.6 ± 0.5	-1.8 ± 1.9	87 ± 89	153 ± 33	–	> 0.18	–
z5-GND-3052	189.288742	62.173836	5.1796	–	-20.3 ± 0.1	-1.4 ± 0.2	53 ± 6	89 ± 6	–	–	–
z5-GNW-11071	188.972424	62.173125	5.1848	–	-19.3 ± 0.1	-1.4 ± 0.8	130 ± 37	87 ± 7	–	–	–
z5-GND-32413	189.357854	62.211445	5.2326	–	-19.2 ± 0.1	-2.2 ± 0.6	18 ± 5	31 ± 19	–	–	–
z5-GNW-20906	189.437681	62.318150	5.2911	–	-21.8 ± 0.0	-1.8 ± 0.3	10 ± 1	478 ± 7	–	–	–
z5-GNW-11014	189.073073	62.172883	5.2946	–	-20.4 ± 0.1	-1.9 ± 0.3	44 ± 7	290 ± 53	–	–	–
z5-GNW-21219	189.310135	62.330258	5.2946	–	-20.3 ± 0.1	-2.2 ± 0.3	60 ± 7	122 ± 7	–	–	–
z5-GNW-22490	189.394847	62.308059	5.3211	–	-20.2 ± 0.1	-3.1 ± 0.8	28 ± 7	240 ± 70	–	–	–
z6-GND-35647	189.329865	62.200844	5.3496	–	-19.4 ± 0.3	-0.8 ± 1.1	59 ± 30	39 ± 9	–	–	–
z5-GND-27819	189.110337	62.225441	5.3510	5.3465	-20.9 ± 0.1	-2.6 ± 0.3	25 ± 4	215 ± 21	502 ± 38	0.16 ± 0.06	258 ± 32
z5-GNW-12482	189.079256	62.182873	5.3543	–	-20.5 ± 0.1	-2.3 ± 0.2	23 ± 3	289 ± 60	–	–	–
z5-GNW-2438	189.106533	62.118483	5.3569	–	-19.8 ± 0.1	-2.6 ± 0.4	50 ± 9	184 ± 27	–	–	–
z5-GNW-1663	189.147548	62.112511	5.3697	–	-19.7 ± 0.1	-1.7 ± 0.5	67 ± 13	156 ± 20	–	–	–
z5-GNW-32760	189.451265	62.241037	5.4033	–	-19.7 ± 0.3	-3.2 ± 1.4	35 ± 19	134 ± 15	–	–	–
z5-GNW-21283	189.403559	62.315688	5.4046	–	-20.0 ± 0.3	-3.8 ± 1.0	35 ± 15	267 ± 33	–	–	–
z5-GNW-7098	189.214160	62.149048	5.4338	–	-20.5 ± 0.2	-2.3 ± 0.8	62 ± 21	161 ± 9	–	–	–
z5-GNW-29609	189.436412	62.265038	5.4455	–	-20.4 ± 0.1	-1.8 ± 0.5	48 ± 8	198 ± 17	–	–	–
z5-GND-21153	189.049628	62.244033	5.4483	5.4430	-21.0 ± 0.1	-1.9 ± 0.3	30 ± 4	209 ± 26	378 ± 17	0.13 ± 0.04	316 ± 20
z5-GNW-13514	188.967311	62.189120	5.4623	–	-20.3 ± 0.2	-3.0 ± 0.9	65 ± 24	115 ± 11	–	–	–
z6-GNW-23350	189.414474	62.333523	5.4633	–	–*	–	–	171 ± 20	–	–	–
z5-GNW-23042	189.415009	62.333538	5.4635	–	-20.0 ± 0.3	-1.3 ± 0.8	183 ± 82	147 ± 9	–	–	–
z5-GND-39445	189.178643	62.187234	5.5048	5.5043	-19.5 ± 0.2	-2.2 ± 1.1	94 ± 43	89 ± 8	267 ± 30	0.29 ± 0.12	37 ± 13
z6-GNW-14478	189.001450	62.194984	5.5546	–	-19.0 ± 0.7	-0.1 ± 1.7	215 ± 447	180 ± 25	–	–	–
z5-GND-7766	189.139984	62.291809	5.5913	–	-20.2 ± 0.1	-0.7 ± 0.2	50 ± 10	161 ± 41	–	> 0.18	–

ID	RA	DEC	$z_{\mathrm{Ly}\alpha}$	z_{sys}	$M_{\mathrm{UV},1500}$	β	$\mathrm{EW}_{\mathrm{Ly}\alpha}$ [Å]	$\mathrm{FWHM}_{\mathrm{Ly}\alpha}$ [km s^{-1}]	$\mathrm{FWHM}_{\mathrm{H}\alpha}$ [km s^{-1}]	f_{esc}	$\Delta v_{\mathrm{Ly}\alpha}$ [km s^{-1}]
z6-GND-36100	189.191274	62.199519	5.6029	5.5975	-20.3 ± 0.0	-2.2 ± 0.1	35 ± 3	166 ± 19	457 ± 105	0.33 ± 0.20	329 ± 37
z6-GND-36553	189.156387	62.197773	5.6109	–	-21.2 ± 0.0	-2.0 ± 0.1	9 ± 1	157 ± 37	–	> 0.39	–
Stark11-13066	189.156399	62.197716	5.6115	–	-21.2 ± 0.0	-2.0 ± 0.1	7 ± 1	87 ± 17	–	> 0.18	–
z6-GNW-14511	189.100538	62.195344	5.6155	5.6117	-20.6 ± 0.1	-2.4 ± 0.6	19 ± 5	173 ± 32	256 ± 30	0.12 ± 0.05	122 ± 32
Hu10-3	189.055939	62.129990	5.6328	–	-20.6± 0.2	–**	–	161 ± 8	–	–	–
Hu10-7	189.032780	62.143962	5.6389	–	-19.6 ± 0.3	-1.2 ± 1.1	323 ± 183	155 ± 4	–	–	–
z6-GND-43125	189.189137	62.300659	5.6585	5.6569	-20.0 ± 0.1	-2.3 ± 0.2	36 ± 5	101 ± 16	302 ± 53	0.38 ± 0.20	116 ± 28
Hu10-6	189.324563	62.299734	5.6611	–	-20.2 ± 0.1	-2.7 ± 0.6	63 ± 17	131 ± 9	–	–	–
z6-GNW-10822	188.995306	62.171460	5.6657	–	-20.5 ± 0.2	-2.6 ± 0.7	26 ± 9	206 ± 26	–	–	–
Hu10-5	189.399713	62.239490	5.6713	–	-21.1 ± 0.1	-2.4 ± 0.3	11 ± 2	169 ± 23	–	–	–
Hu10-11	189.366007	62.196189	5.6719	–	-19.2 ± 0.2	-1.4 ± 0.7	78 ± 26	107 ± 11	–	–	–
z5-GND-37006	189.366007	62.196189	5.6720	–	-19.2 ± 0.2	-1.4 ± 0.7	85 ± 30	99 ± 11	–	–	–
Stark11-22381	189.255389	62.357754	5.6920	–	-20.2 ± 0.3	-3.1 ± 1.6	12 ± 6	122 ± 28	–	–	–
Stark11-3982	189.039261	62.247654	5.7080	–	-19.6 ± 0.1	-4.0 ± 0.6	24 ± 7	108 ± 39	–	> 0.26	–
z6-GNW-11543	189.157441	62.176502	5.7696	–	-20.7 ± 0.1	-1.7 ± 0.8	8 ± 3	49 ± 19	–	> 0.19	–
z7-GNW-22375	189.342596	62.308518	5.7718	–	-20.1 ± 0.5	-2.7 ± 1.4	19 ± 14	26 ± 7	–	–	–
z5-GND-17752	189.091798	62.253735	5.7744	5.7750	-19.8 ± 0.1	-1.5 ± 0.4	98 ± 19	138 ± 14	121 ± 59	1.23 ± 0.79	22 ± 25
Stark11-17705	189.208207	62.232128	5.8027	5.7925	-19.7 ± 0.2	-1.8 ± 1.1	45 ± 20	109 ± 23	254 ± 73	0.31 ± 0.21	496 ± 31
z6-GND-30340	189.388906	62.217840	5.8079	–	-20.0 ± 0.4	-2.7 ± 1.1	66 ± 42	218 ± 28	–	–	–
z6-GNW-21823	189.355591	62.312592	5.8228	–	-20.9 ± 0.4	-2.1 ± 1.3	23 ± 16	62 ± 9	–	–	–
z5-GNW-11701	189.055409	62.177498	5.8364	–	-19.6 ± 0.6	-1.8 ± 1.7	18 ± 18	36 ± 14	–	–	–
z5-GND-464	189.270721	62.148424	5.8745	–	-20.0 ± 0.1	-2.2 ± 0.2	57 ± 6	110 ± 9	–	–	–
Stark11-24923	189.284538	62.287491	5.9498	5.9483	-20.0 ± 0.2	-1.4 ± 1.1	30 ± 14	193 ± 69	507 ± 78	0.14 ± 0.08	114 ± 56
Stark11-26902	189.307610	62.323443	5.9547	–	-19.0 ± 0.6	-1.4 ± 1.8	197 ± 215	284 ± 37	–	–	–
z6-GNW-25971	189.334732	62.286125	5.9549	–	-19.7 ± 0.5	-1.9 ± 1.3	38 ± 32	194 ± 40	–	–	–

ID	RA	DEC	$z_{\mathrm{Ly}\alpha}$	z_{sys}	$M_{\mathrm{UV},1500}$	β	$\mathrm{EW}_{\mathrm{Ly}\alpha}$ [Å]	$\mathrm{FWHM}_{\mathrm{Ly}\alpha}$ [$\mathrm{km\,s^{-1}}$]	$\mathrm{FWHM}_{\mathrm{H}\alpha}$ [$\mathrm{km\,s^{-1}}$]	f_{esc}	$\Delta v_{\mathrm{Ly}\alpha}$ [$\mathrm{km\,s^{-1}}$]
z6-GND-14309	189.334047	62.263058	5.9676	–	-20.0 ± 0.2	-1.2 ± 1.0	104 ± 38	8 ± 6	–	> 1.01	–
Stark11-6706	189.079712	62.141884	5.9719	–	-20.0 ± 0.5	-3.0 ± 1.5	31 ± 21	157 ± 30	–	–	–
Stark11-16773	189.197796	62.199983	5.9731	–	-19.3 ± 0.1	-2.7 ± 0.4	37 ± 7	98 ± 20	–	> 0.22	–
z5-GND-10047	189.296277	62.277386	6.0108	–	-21.0 ± 0.0	-1.7 ± 0.1	4 ± 1	59 ± 44	–	> 0.08	–
z6-GND-19165	189.347733	62.249866	6.0471	–	-20.0 ± 0.1	-2.0 ± 0.4	33 ± 6	179 ± 30	–	> 0.34	–
z7-GND-43678	189.235201	62.295597	6.1212	–	-19.7 ± 0.1	-1.2 ± 0.5	112 ± 25	29 ± 5	–	> 0.71	–
z6-GNW-2993	189.127197	62.122612	6.1357	–	-19.8 ± 0.5	-1.1 ± 1.6	47 ± 45	123 ± 59	–	–	–
Jung18-28438	189.178023	62.223718	6.5518	6.5442	-20.0 ± 0.2	-3.0 ± 0.9	30 ± 11	93 ± 15	120 ± 35	0.21 ± 0.12	376 ± 25
Hu10-1	189.358260	62.207637	6.5604	–	-20.3 ± 0.1	-2.5 ± 0.8	166 ± 51	267 ± 25	–	–	–
Hu10-2	189.356888	62.295321	6.5760	–	-21.9 ± 0.1	-1.8 ± 0.4	24 ± 4	192 ± 4	–	–	–
z5-GND-23860	189.314385	62.236461	6.5847	–	-21.3 ± 0.1	-1.4 ± 0.2	23 ± 2	32 ± 5	–	> 0.18	–
Jung18-5752	189.199585	62.320965	6.5867	–	-19.2 ± 0.3	-1.9 ± 1.6	103 ± 72	94 ± 11	–	> 0.16	–
z6-GND-44831	189.175135	62.282267	6.7365	–	-20.6 ± 0.1	-2.9 ± 0.6	54 ± 13	71 ± 7	–	–	–
z7-GND-8358	189.155310	62.286461	6.8135	6.8072	-20.3 ± 0.1	-2.7 ± 0.5	11 ± 5	59 ± 26	–	–	276 ± 26
z8-GND-35384	189.231989	62.202333	6.8743	–	-19.9 ± 0.6	-1.7 ± 2.3	178 ± 198	28 ± 4	–	–	–

4.9 Spectra, MMT/Binospec and NIRCam/JWST

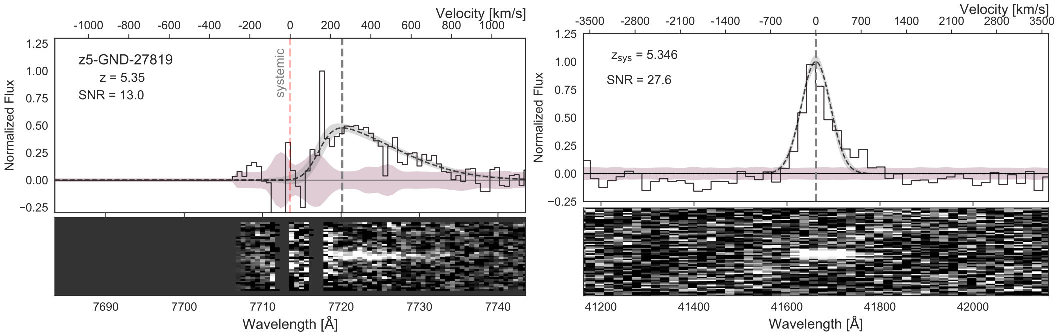

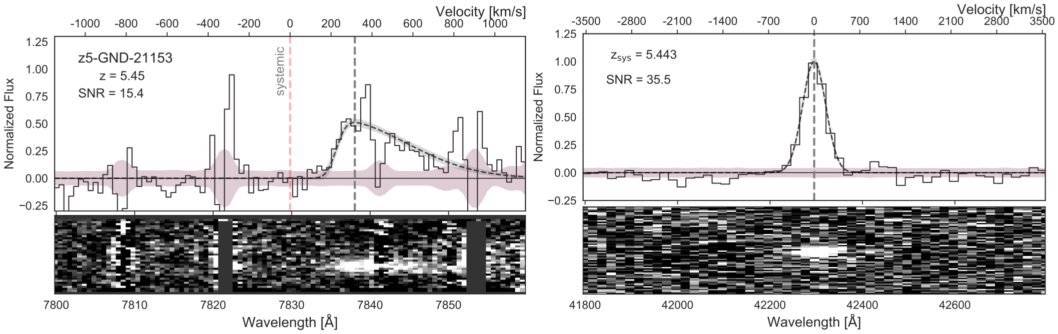

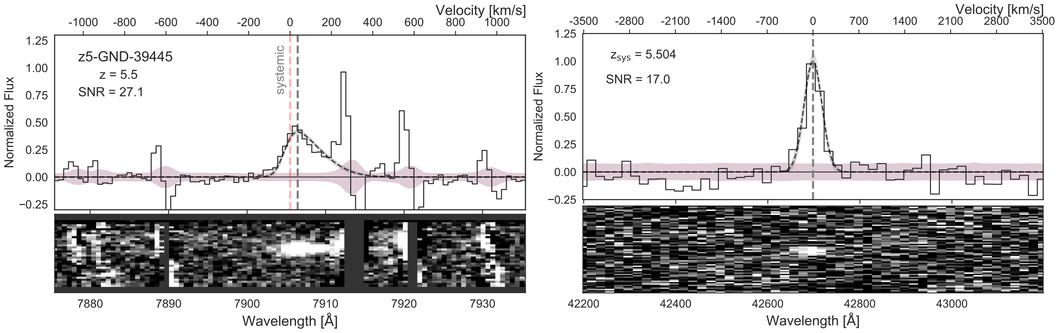

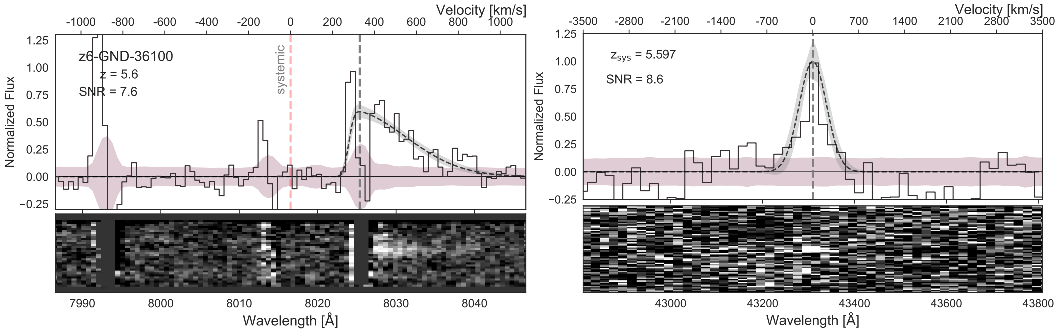
z6-GND-36100
z = 5.6
SNR = 7.6
systemic
Velocity [km/s]
Normalized Flux
Wavelength [Å]
z_{sys} = 5.597
SNR = 8.6

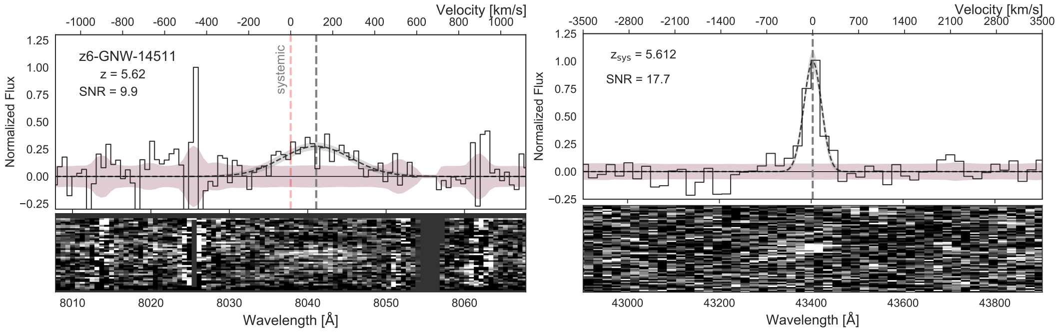
z6-GNW-14511
z = 5.62
SNR = 9.9
systemic
Velocity [km/s]
Normalized Flux
Wavelength [Å]
z_{sys} = 5.612
SNR = 17.7

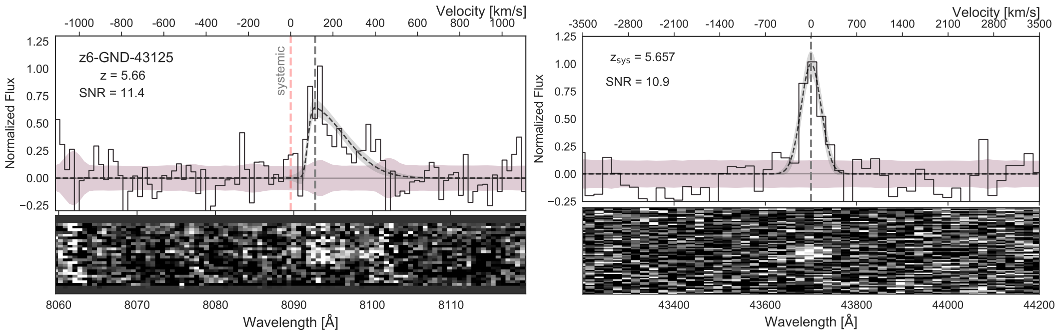
z6-GND-43125
z = 5.66
SNR = 11.4
systemic
Velocity [km/s]
Normalized Flux
Wavelength [Å]
z_{sys} = 5.657
SNR = 10.9

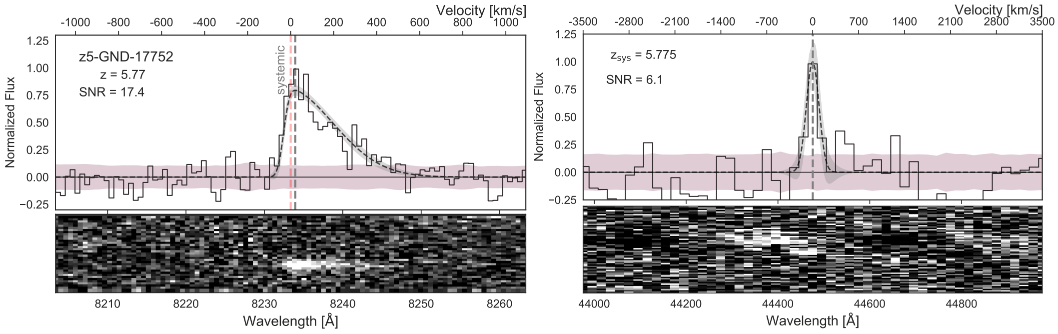
z5-GND-17752
z = 5.77
SNR = 17.4
systemic
Velocity [km/s]
Normalized Flux
Wavelength [Å]
z_{sys} = 5.775
SNR = 6.1

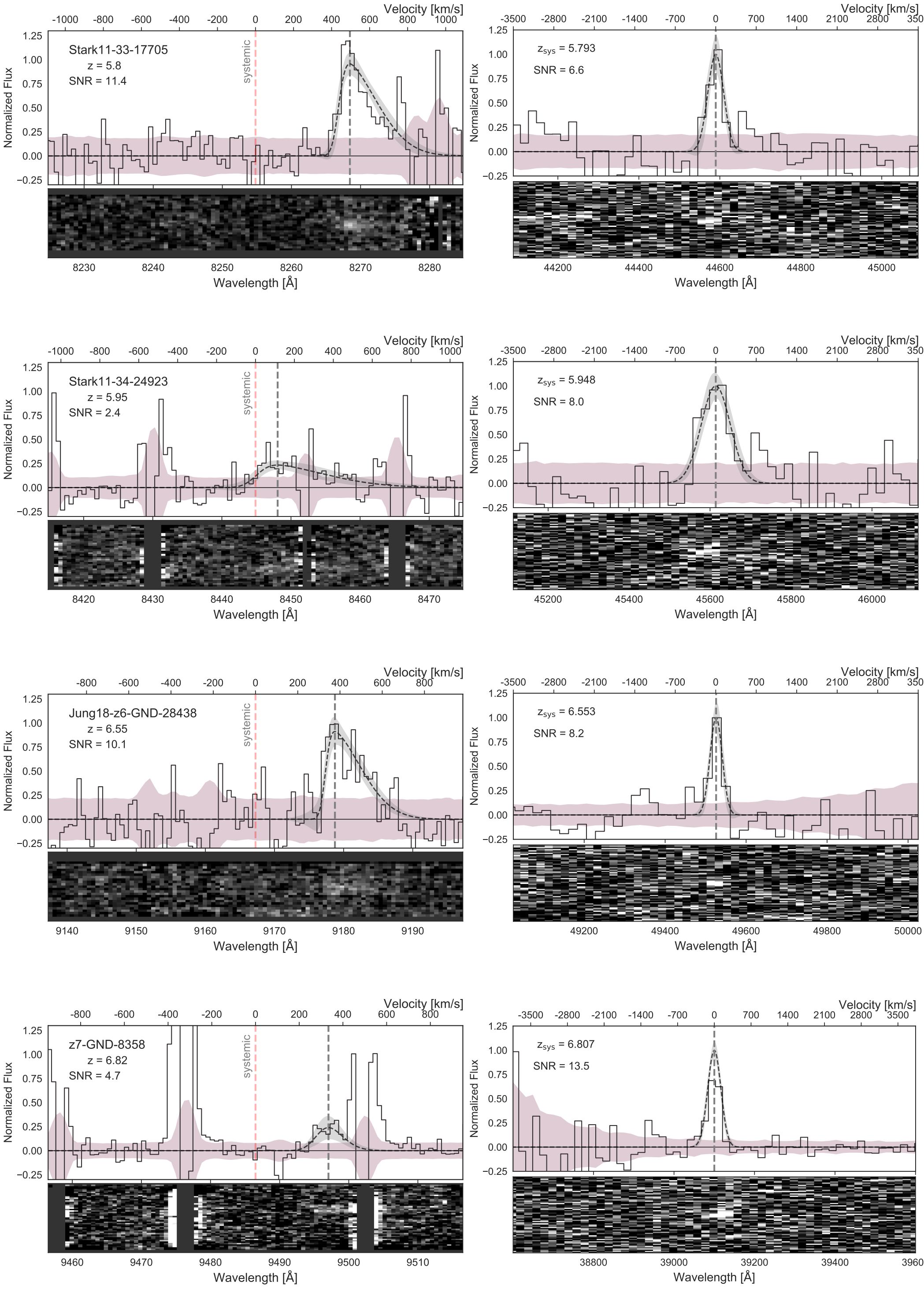
Stark11-33-17705
z = 5.8
SNR = 11.4
z_sys = 5.793
SNR = 6.6
Stark11-34-24923
z = 5.95
SNR = 2.4
z_sys = 5.948
SNR = 8.0
Jung18-z6-GND-28438
z = 6.55
SNR = 10.1
z_sys = 6.553
SNR = 8.2
z7-GND-8358
z = 6.82
SNR = 4.7
z_sys = 6.807
SNR = 13.5
systemic
Velocity [km/s]
Normalized Flux
Wavelength [Å]

A BRIGHT FUTURE FOR THE EPOCH OF REIONIZATION

5

5.1 Conclusions

The evolution of neutral hydrogen in the EoR and the galaxies that inhabit the early Universe are linked to each other. Galaxies will change the structure of the IGM, while at the same time, the IGM changes their observed emission. In this thesis, I have attempted to understand the emission of these galaxies as it emerges from their ISM/CGM through the use of analogs at the end of the EoR z$\sim$ 3 - 6.5. I have approached this problem from their ionizing photon production rate and their Lyman Alpha emission line.

In the previous chapters I have measured for the first time the $\xi_{\rm ion}$ distribution of individual UV-faint ($M_{\rm UV}$ >-20) galaxies (Chapter 2), and shown the first measurements of Lyα velocity offsets in galaxies as faint as $M_{\rm UV}$ >-16 (Chapter 3). Finally we have developed an empirical Bayesian model for inferring $EW_{\rm Ly\alpha}$ and $f_{\rm esc}$ based on a galaxies $M_{\rm UV}$, as well as given for the first high-resolution measurements of $FWHM_{\rm Ly\alpha}$ at z $\sim$ 5 - 6 (Chapter 4).

Our key results, and questions that remain open are :

- We showed for the first time the distribution of $\log_{10}\xi_{\rm ion}$ (1-$f_{\rm esc}$) up to $M_{\rm UV}$ $\sim$ -15 and how it evolves with different galaxy properties. With an overall median of 25.33 and an intrinsic scatter of 0.42, tge broad distribution brings the question : What are the physical processes that produce such varied $\xi_{\rm ion}$ values for galaxies with the same UV luminosity? And can we reasonably constraint $f_{\rm esc}$ in order to know the true budget that galaxies release at the EoR?

- We gave the first view into the Lyα velocity offset of the faintest galaxies. Our results reveal that they do not differ much from the systemic redshift, implying an almost direct escape from the ISM/CGM. We expect sources like this to be only detectable in massive ionized bubbles, but it remains to be seen how well they may help predicting their presence.

- The high-resolution of our observations allowed us to tightly constraint the $FWHM_{\rm Ly\alpha}$ distribution for the first time in galaxies at z $\sim$ 5 - 6.5. The new Lyα line shape measurements imply that the transmission might be boosted 5 times more than what previous models made from low-redshift observations show. Leading to the possibility of the IGM being even more neutral than what we currently think. With our new Lyα observations we produced a new model for inferring $\mathrm{EW}_{\mathrm{Ly}\alpha}$ based on M_{UV} . This emergent properties of Lyα , next to our simple f_{esc} model, and other results such as $\Delta v_{\mathrm{Ly}\alpha}$, take us one step closer to solving the biggest questions of the EoR: When did reionization occur, and what sources dominated the process?

With the lower number of quasars expected in the high-z Universe, the best tool to answer these questions is through observations of Lyα . As of now, great results have been achieved at $z > 8$ with JWST, finding thousands of galaxies (e.g. Donnan et al., 2024; Tang et al., 2024b; Jones et al., 2024b), but likely 100s of Lyα detections from new surveys across the sky will be needed to properly constraint xHI. New surveys have shown promising results on Lyα detection in the early Universe (e.g. Witstok et al., 2024,b; Nakane et al., 2024), probing that indeed it is indeed possible to observe Lyα up to redshift 14.

New high redshift Lyα observations, next to empirical models and observational correlations built from galaxies outside of the EoR, such as the ones presented here, will be key assets for constraining the epoch of reionization. Hopefully within the next decade of JWST as high redshift Lyα surveys and spectroscopic datasets increase in number, we will finally answer the question “When did reionization occur?”.

REFERENCES

Abdurro'uf, Accetta, K., Aerts, C., et al. 2022, , 259, 35, doi: 10.3847/1538-4365/ac4414

Allen, N., Oesch, P. A., Toft, S., et al. 2024, arXiv e-prints, arXiv:2410.16354, doi: 10.48550/arXiv.2410.16354

Anders, P., & Fritze-v. Alvensleben, U. 2003, , 401, 1063, doi: 10.1051/0004-6361:20030151

Barbary, K. 2018, SEP: Source Extraction and Photometry, Astrophysics Source Code Library, record ascl:1811.004. http://ascl.net/1811.004

Barro, G., Pérez-González, P. G., Cava, A., et al. 2019, , 243, 22, doi: 10.3847/1538-4365/ab23f2

Becker, G. D., Bolton, J. S., Madau, P., et al. 2015, , 447, 3402, doi: 10.1093/mnras/stu2646

Becker, G. D., D'Aloisio, A., Christenson, H. M., et al. 2021, , 508, 1853, doi: 10.1093/mnras/stab2696

Begley, R., Cullen, F., McLure, R. J., et al. 2022, , 513, 3510, doi: 10.1093/mnras/stac1067

Bergamini, P., Acebron, A., Grillo, C., et al. 2022, arXiv e-prints, arXiv:2207.09416. https://arxiv.org/abs/2207.09416

Bezanson, R., Labbe, I., Whitaker, K. E., et al. 2022, arXiv e-prints, arXiv:2212.04026, doi: 10.48550/arXiv.2212.04026

Binney, J. 2004, , 347, 1093, doi: 10.1111/j.1365-2966.2004.07277.x

Bolan, P., Lemaux, B. C., Mason, C., et al. 2022, , 517, 3263, doi: 10.1093/mnras/stac1963

Bosman, S. E. I., Davies, F. B., Becker, G. D., et al. 2022, , 514, 55, doi: 10.1093/mnras/stac1046

Bouwens, R. J., Illingworth, G. D., a. Oesch, P., et al. 2015, , 811, 140, doi: 10.1088/0004-637X/811/2/140

Bouwens, R. J., Smit, R., Labbé, I., et al. 2016a, , 831, 176, doi: 10.3847/0004-637X/831/2/176

Bouwens, R. J., Illingworth, G. D., Oesch, P., et al. 2012, , 754, 83, doi: 10.1088/0004-637X/754/2/83

Bouwens, R. J., Illingworth, G. D., Oesch, P. A., et al. 2014, , 793, 115, doi: 10.1088/0004-637X/793/2/115

Bouwens, R. J., Aravena, M., Decarli, R., et al. 2016b, , 833, 72, doi: 10.3847/1538-4357/833/1/72

Bouwens, R. J., Oesch, P. A., Stefanon, M., et al. 2021, , 162, 47, doi: 10.3847/1538-3881/abf83e

Boyett, K., Mascia, S., Pentericci, L., et al. 2022a, arXiv e-prints, arXiv:2207.13459. https://arxiv.org/abs/2207.13459

Boyett, K. N. K., Stark, D. P., Bunker, A. J., Tang, M., & Maseda, M. V. 2022b, , 513, 4451, doi: 10.1093/mnras/stac1109

Bradač, M., Garcia-Appadoo, D., Huang, K.-H., et al. 2017, , 836, L2, doi: 10.3847/2041-8213/836/1/L2

Brammer, G. 2023, grizli, 1.9.11, Zenodo, doi: 10.5281/zenodo.8370018

Brammer, G., & Matharu, J. 2021, gbrammer/grizli: Release 2021, 1.3.2, Zenodo, doi: 10.5281/zenodo.5012699

Brammer, G., Strait, V., Matharu, J., & Momcheva, I. 2022, grizli, 1.5.0, Zenodo, Zenodo, doi: 10.5281/zenodo.6672538

Brammer, G. B., van Dokkum, P. G., & Coppi, P. 2008, , 686, 1503, doi: 10.1086/591786

Brammer, G. B., van Dokkum, P. G., Franx, M., et al. 2012, , 200, 13, doi: 10.1088/0067-0049/200/2/13

Bruzual, G., & Charlot, S. 2003, , 344, 1000, doi: 10.1046/j.1365-8711.2003.06897.x

Bunker, A. J., Saxena, A., Cameron, A. J., et al. 2023, arXiv e-prints, arXiv:2302.07256. https://arxiv.org/abs/2302.07256

Byrohl, C., Saito, S., & Behrens, C. 2019, arXiv:1906.02173 [astro-ph]. https://arxiv.org/abs/1906.02173

Caminha, G. B., Grillo, C., Rosati, P., et al. 2017, , 600, A90, doi: 10.1051/0004-6361/201629297

Caminha, G. B., Rosati, P., Grillo, C., et al. 2019, , 632, A36, doi: 10.1051/0004-6361/201935454

Carnall, A. C., McLure, R. J., Dunlop, J. S., & Davé, R. 2018, , 480, 4379, doi: 10.1093/mnras/sty2169

Carniani, S., Venturi, G., Parlanti, E., et al. 2023, arXiv e-prints, arXiv:2306.11801, doi: 10.48550/arXiv.2306.11801

Cassata, P., Tasca, L. A. M., Le Fèvre, O., et al. 2015, , 573, A24, doi: 10.1051/0004-6361/201423824

Cassata, P., Morselli, L., Faisst, A., et al. 2020, , 643, A6, doi: 10.1051/0004-6361/202037517

Chabrier, G. 2003, Publ. Astron. Soc. Pacific, 115, 763, doi: 10.1086/376392

Charlot, S., & Fall, S. M. 1993, , 415, 580, doi: 10.1086/173187

Chen, Z., Stark, D. P., Mason, C., et al. 2024, , 528, 7052, doi: 10.1093/mnras/stae455

Chevallard, J., Charlot, S., Senchyna, P., et al. 2018, , 479, 3264, doi: 10.1093/mnras/sty1461

Covelo-Paz, A., Giovinazzo, E., Oesch, P. A., et al. 2024, arXiv e-prints, arXiv:2409.17241, doi: 10.48550/arXiv.2409.17241

Cullen, F., McLure, R. J., McLeod, D. J., et al. 2023, , 520, 14, doi: 10.1093/mnras/stad073

Davies, F. B., Hennawi, J. F., Bañados, E., et al. 2018, , 864, 142, doi: 10.3847/1538-4357/aad6dc

De Barros, S., Pentericci, L., Vanzella, E., et al. 2017, , 608, A123, doi: 10.1051/0004-6361/201731476

Dijkstra, M. 2014, , 31, e040, doi: 10.1017/pasa.2014.33

Dijkstra, M., Gronke, M., & Venkatesan, A. 2016, , 828, 71, doi: 10.3847/0004-637X/828/2/71

Dijkstra, M., Lidz, A., & Wyithe, J. S. B. 2007, , 377, 1175, doi: 10.1111/j.1365-2966.2007.11666.x

Dijkstra, M., Mesinger, A., & Wyithe, J. S. B. 2011, , 414, 2139, doi: 10.1111/j.1365-2966.2011.18530.x

Dijkstra, M., & Wyithe, J. S. B. 2012, , 419, 3181, doi: 10.1111/j.1365-2966.2011.19958.x

Dijkstra, M., & Wyithe, S. 2010, , 408, 352, doi: 10.1111/j.1365-2966.2010.17112.x

Donnan, C. T., McLure, R. J., Dunlop, J. S., et al. 2024, , 533, 3222, doi: 10.1093/mnras/stae2037

Du, X., Shapley, A. E., Tang, M., et al. 2020, , 890, 65, doi: 10.3847/1538-4357/ab67b8

Eilers, A.-C., Hennawi, J. F., Davies, F. B., & Oñorbe, J. 2019, arXiv:1906.05874 [astro-ph]. https://arxiv.org/abs/1906.05874

Eisenstein, D. J., Willott, C., Alberts, S., et al. 2023a, arXiv e-prints, arXiv:2306.02465, doi: 10.48550/arXiv.2306.02465

—. 2023b, arXiv e-prints, arXiv:2306.02465, doi: 10.48550/arXiv.2306.02465

Emami, N., Siana, B., Alavi, A., et al. 2020, , 895, 116, doi: 10.3847/1538-4357/ab8f97

Endsley, R., Stark, D. P., Whitler, L., et al. 2022a, arXiv e-prints, arXiv:2208.14999, doi: 10.48550/arXiv.2208.14999

Endsley, R., Stark, D. P., Bouwens, R. J., et al. 2022b, arXiv e-prints, arXiv:2202.01219. https://arxiv.org/abs/2202.01219

Erb, D. K., Steidel, C. C., Trainor, R. F., et al. 2014, , 795, 33, doi: 10.1088/0004-637X/795/1/33

Euclid Collaboration, Barnett, R., Warren, S. J., et al. 2019, , 631, A85, doi: 10.1051/0004-6361/201936427

Fabricant, D., Fata, R., Epps, H., et al. 2019, , 131, 075004, doi: 10.1088/1538-3873/ab1d78

Fan, X., Strauss, M. A., Becker, R. H., et al. 2006, Astron. J., 132, 117, doi: 10.1086/504836

Faucher-Giguère, C.-A., Prochaska, J. X., Lidz, A., Hernquist, L., & Zaldarriaga, M. 2008, , 681, 831, doi: 10.1086/588648

Finkelstein, S. L., D'Aloisio, A., Paardekooper, J.-P., et al. 2019, arXiv:1902.02792 [astro-ph]. https://arxiv.org/abs/1902.02792

Foreman-Mackey, D., Hogg, D. W., Lang, D., & Goodman, J. 2013, Publ. Astron. Soc. Pacific, 125, 306, doi: 10.1086/670067

Fuller, S., Lemaux, B. C., Bradač, M., et al. 2020, , 896, 156, doi: 10.3847/1538-4357/ab959f

Gaikwad, P., Haehnelt, M. G., Davies, F. B., et al. 2023, , 525, 4093, doi: 10.1093/mnras/stad2566

Gelli, V., Mason, C., & Hayward, C. C. 2024, arXiv e-prints, arXiv:2405.13108, doi: 10.48550/arXiv.2405.13108

Giavalisco, M., Ferguson, H. C., Koekemoer, A. M., et al. 2004, , 600, L93, doi: 10.1086/379232

Greig, B., & Mesinger, A. 2017, , 465, 4838, doi: 10.1093/mnras/stw3026

Greig, B., Mesinger, A., Koopmans, L. V. E., et al. 2021, , 501, 1, doi: 10.1093/mnras/staa3593

Grogin, N. A., Kocevski, D. D., Faber, S. M., et al. 2011, , 197, 35, doi: 10.1088/0067-0049/197/2/35

Gronke, M., Bull, P., & Dijkstra, M. 2015, , 812, 123, doi: 10.1088/0004-637X/812/2/123

Gronke, M., Dijkstra, M., McCourt, M., & Peng Oh, S. 2016, , 833, L26, doi: 10.3847/2041-8213/833/2/L26

Gunn, J. E., & Peterson, B. A. 1965, , 142, 1633, doi: 10.1086/148444

Harikane, Y., Ouchi, M., Shibuya, T., et al. 2018, The Astrophysical Journal, 859, 84, doi: 10.3847/1538-4357/aabd80

Hashimoto, T., Ouchi, M., Shimasaku, K., et al. 2013, , 765, 70, doi: 10.1088/0004-637X/765/1/70

Hashimoto, T., Verhamme, A., Ouchi, M., et al. 2015, , 812, 157, doi: 10.1088/0004-637X/812/2/157

Hashimoto, T., Inoue, A. K., Mawatari, K., et al. 2018, arXiv:1806.00486 [astro-ph]. https://arxiv.org/abs/1806.00486

Hayes, M. J., Runnholm, A., Scarlata, C., Gronke, M., & Rivera-Thorsen, T. E. 2023, arXiv e-prints, arXiv:2302.04875. https://arxiv.org/abs/2302.04875

Heckman, T. M., Alexandroff, R. M., Borthakur, S., Overzier, R., & Leitherer, C. 2015, , 809, 147, doi: 10.1088/0004-637X/809/2/147

Henry, A., Scarlata, C., Martin, C. L., & Erb, D. 2015, , 809, 19, doi: 10.1088/0004-637X/809/1/19

HERA Collaboration, Abdurashidova, Z., Adams, T., et al. 2023, , 945, 124, doi: 10.3847/1538-4357/acaf50

Hoag, A., Treu, T., Pentericci, L., et al. 2019a, , 488, 706, doi: 10.1093/mnras/stz1768

Hoag, A., Bradač, M., Huang, K., et al. 2019b, , 878, 12, doi: 10.3847/1538-4357/ab1de7

Hu, E. M., Cowie, L. L., Barger, A. J., et al. 2010, , 725, 394, doi: 10.1088/0004-637X/725/1/394

Hutter, A., Heneka, C., Dayal, P., et al. 2023, , 525, 1664, doi: 10.1093/mnras/stad2376

Inoue, A. K., Shimizu, I., Iwata, I., & Tanaka, M. 2014, , 442, 1805, doi: 10.1093/mnras/stu936

Inoue, A. K., Tamura, Y., Matsuo, H., et al. 2016, Science, 352, 1559, doi: 10.1126/science.aaf0714

Ishigaki, M., Kawamata, R., Ouchi, M., et al. 2018, , 854, 73, doi: 10.3847/1538-4357/aaa544

Jakobsen, P., Ferruit, P., Alves de Oliveira, C., et al. 2022, , 661, A80, doi: 10.1051/0004-6361/202142663

Jaskot, A. E., Dowd, T., Oey, M. S., Scarlata, C., & McKinney, J. 2019, arXiv:1908.09763

Jones, G. C., Bunker, A. J., Saxena, A., et al. 2024a, , 683, A238, doi: 10.1051/0004-6361/202347099

—. 2024b, arXiv e-prints, arXiv:2409.06405, doi: 10.48550/arXiv.2409.06405

Jung, I., Finkelstein, S. L., Livermore, R. C., et al. 2018, , 864, 103, doi: 10.3847/1538-4357/aad686

Jung, I., Finkelstein, S. L., Dickinson, M., et al. 2020, , 904, 144, doi: 10.3847/1538-4357/abbd44

Kakiichi, K., & Gronke, M. 2021, , 908, 30, doi: 10.3847/1538-4357/abc2d9

Kelly, B. C. 2007, , 665, 1489, doi: 10.1086/519947

Koekemoer, A. M., Faber, S. M., Ferguson, H. C., et al. 2011, , 197, 36, doi: 10.1088/0067-0049/197/2/36

Kornei, K. A., Shapley, A. E., Erb, D. K., et al. 2010, , 711, 693, doi: 10.1088/0004-637X/711/2/693

Lam, D., Bouwens, R. J., Labbe, I., et al. 2019a, arXiv:1902.02786 [astro-ph]. https://arxiv.org/abs/1902.02786

Lam, D., Bouwens, R. J., Coe, D., et al. 2019b, arXiv:1903.08177 [astro-ph]. https://arxiv.org/abs/1903.08177

Larson, R. L., Finkelstein, S. L., Kocevski, D. D., et al. 2023, arXiv e-prints, arXiv:2303.08918, doi: 10.48550/arXiv.2303.08918

Laursen, P., Sommer-Larsen, J., & Andersen, A. C. 2009, , 704, 1640, doi: 10.1088/0004-637X/704/2/1640

Laursen, P., Sommer-Larsen, J., & Razoumov, A. O. 2011, , 728, 52, doi: 10.1088/0004-637X/728/1/52

Leclercq, F., Bacon, R., Wisotzki, L., et al. 2017, , 608, A8, doi: 10.1051/0004-6361/201731480

Leitherer, C., & Heckman, T. M. 1995, Supplement Series, 96, 9, doi: 10.1086/192112

Lemaux, B. C., Fuller, S., Bradač, M., et al. 2021, , 504, 3662, doi: 10.1093/mnras/stab924

Leonova, E., Oesch, P. A., Qin, Y., et al. 2022, , 515, 5790, doi: 10.1093/mnras/stac1908

Lin, X., Cai, Z., Wu, Y., et al. 2024, , 272, 33, doi: 10.3847/1538-4365/ad3e7d

Lotz, J. M., Koekemoer, A., Coe, D., et al. 2017, , 837, 97, doi: 10.3847/1538-4357/837/1/97

Lu, T.-Y., Mason, C., Hutter, A., et al. 2023, arXiv e-prints, arXiv:2304.11192, doi: 10.48550/arXiv.2304.11192

Lu, T.-Y., Mason, C. A., Hutter, A., et al. 2024, , 528, 4872, doi: 10.1093/mnras/stae266

Lu, T.-Y., Goto, T., Tang, J.-J., et al. 2020, , 893, 69, doi: 10.3847/1538-4357/ab7db7

Ma, X., Quataert, E., Wetzel, A., et al. 2020, arXiv:2003.05945 [astro-ph]. https://arxiv.org/abs/2003.05945

Madau, P., Haardt, F., & Rees, M. J. 1999, , 514, 648, doi: 10.1086/306975

Mahler, G., Richard, J., Clément, B., et al. 2018, , 473, 663, doi: 10.1093/mnras/stx1971

Mainali, R., Zitrin, A., Stark, D. P., et al. 2018, , 479, 1180, doi: 10.1093/mnras/sty1640

Maiolino, R., Nagao, T., Grazian, A., et al. 2008, , 488, 463, doi: 10.1051/0004-6361:200809678

Mármol-Queraltó, E., McLure, R. J., Cullen, F., et al. 2016, , 460, 3587, doi: 10.1093/mnras/stw1212

Marques-Chaves, R., Schaerer, D., Á lvarez-Márquez, J., et al. 2022, Monthly Notices of the Royal Astronomical Society, 517, 2972, doi: 10.1093/mnras/stac2893

Mascia, S., Pentericci, L., Calabro', A., et al. 2023, arXiv e-prints, arXiv:2301.02816, doi: 10.48550/arXiv.2301.02816

Maseda, M. V., Bacon, R., Lam, D., et al. 2020, arXiv:2002.11117 [astro-ph]. https://arxiv.org/abs/2002.11117

Mason, C. A., & Gronke, M. 2020, , 499, 1395, doi: 10.1093/mnras/staa2910

Mason, C. A., Naidu, R. P., Tacchella, S., & Leja, J. 2019, , 489, 2669, doi: 10.1093/mnras/stz2291

Mason, C. A., Trenti, M., & Treu, T. 2015, , 813, 21, doi: 10.1088/0004-637X/813/1/21

Mason, C. A., Treu, T., Dijkstra, M., et al. 2018a, , 856, 2, doi: 10.3847/1538-4357/aab0a7

Mason, C. A., Treu, T., Fontana, A., et al. 2017, , 838, 14, doi: 10.3847/1538-4357/aa60c4

Mason, C. A., Treu, T., de Barros, S., et al. 2018b, , 857, L11, doi: 10.3847/2041-8213/aabbab

Mason, C. A., Fontana, A., Treu, T., et al. 2019, , 485, 3947, doi: 10.1093/mnras/stz632

Matthee, J., Mackenzie, R., Simcoe, R. A., et al. 2022, arXiv e-prints, arXiv:2211.08255. https://arxiv.org/abs/2211.08255

McGreer, I. D., Mesinger, A., & D'Odorico, V. 2015, , 447, 499, doi: 10.1093/mnras/stu2449

McLeod, D. J., McLure, R. J., Dunlop, J. S., et al. 2021, , 503, 4413, doi: 10.1093/mnras/stab731

Mesinger, A., Aykutalp, A., Vanzella, E., et al. 2015, , 446, 566, doi: 10.1093/mnras/stu2089

Mesinger, A., & Furlanetto, S. R. 2008, , 385, 1348, doi: 10.1111/j.1365-2966.2007.12836.x

Meyer, R. A., Oesch, P. A., Giovinazzo, E., et al. 2024, , 535, 1067, doi: 10.1093/mnras/stae2353

Miralda-Escude, J. 1998, , 501, 15, doi: 10.1086/305799

Morales, A. M., Mason, C. A., Bruton, S., et al. 2021, , 919, 120, doi: 10.3847/1538-4357/ac1104

Morishita, T., Roberts-Borsani, G., Treu, T., et al. 2022, arXiv e-prints, arXiv:2211.09097, doi: 10.48550/arXiv.2211.09097

Morishita, T., Stiavelli, M., Chary, R.-R., et al. 2024, , 963, 9, doi: 10.3847/1538-4357/ad1404

Muñoz, J. B., Mirocha, J., Chisholm, J., Furlanetto, S. R., & Mason, C. 2024, , 535, L37, doi: 10.1093/mnrasl/slae086

Mukherjee, T., Zafar, T., Nanayakkara, T., et al. 2024, arXiv e-prints, arXiv:2410.17684, doi: 10.48550/arXiv.2410.17684

Muzahid, S., Schaye, J., Marino, R. A., et al. 2020, , 496, 1013, doi: 10.1093/mnras/staa1347

Naidu, R. P., Tacchella, S., Mason, C. A., et al. 2020, , 892, 109, doi: 10.3847/1538-4357/ab7cc9

Naidu, R. P., Matthee, J., Oesch, P. A., et al. 2022, , 510, 4582, doi: 10.1093/mnras/stab3601

Nakane, M., Ouchi, M., Nakajima, K., et al. 2024, , 967, 28, doi: 10.3847/1538-4357/ad38c2

Nelson, D., Springel, V., Pillepich, A., et al. 2019, Computational Astrophysics and Cosmology, 6, 2, doi: 10.1186/s40668-019-0028-x

Neufeld, D. A. 1990, , 350, 216, doi: 10.1086/168375

Neufeld, D. A. 1991, , 370, L85, doi: 10.1086/185983

Ning, Y., Cai, Z., Jiang, L., et al. 2022, arXiv e-prints, arXiv:2211.13620. https://arxiv.org/abs/2211.13620

Oesch, P. A., Bouwens, R. J., Illingworth, G. D., Labbe, I., & Stefanon, M. 2018, , 855, 105, doi: 10.3847/1538-4357/aab03f

Oesch, P. A., Dokkum, P. G. V., Illingworth, G. D., et al. 2015, , 804, L30, doi: 10.1088/2041-8205/804/2/L30

Oesch, P. A., Brammer, G., van Dokkum, P. G., et al. 2016, , 819, 129, doi: 10.3847/0004-637X/819/2/129

Oesch, P. A., Brammer, G., Naidu, R. P., et al. 2023, , 525, 2864, doi: 10.1093/mnras/stad2411

Osterbrock, D. E., & Ferland, G. J. 2006, Astrophysics of gaseous nebulae and active galactic nuclei

Ouchi, M., Shimasaku, K., Furusawa, H., et al. 2010, , 723, 869, doi: 10.1088/0004-637X/723/1/869

Oyarzún, G. A., Blanc, G. A., González, V., Mateo, M., & Bailey, J. I. 2017, , 843, 133, doi: 10.3847/1538-4357/aa7552

Pahl, A., Shapley, A., Steidel, C., Reddy, N., & Chen, Y. 2023, in American Astronomical Society Meeting Abstracts, Vol. 55, American Astronomical Society Meeting Abstracts, 443.02D

Paris, D., Merlin, E., Fontana, A., et al. 2023, arXiv e-prints, arXiv:2301.02179, doi: 10.48550/arXiv.2301.02179

Park, H., Jung, I., Song, H., et al. 2021, , 922, 263, doi: 10.3847/1538-4357/ac2f4b

Pentericci, L., Vanzella, E., Fontana, A., et al. 2014, , 793, 113, doi: 10.1088/0004-637X/793/2/113

Pentericci, L., Carniani, S., Castellano, M., et al. 2016, , 829, L11, doi: 10.3847/2041-8205/829/1/L11

Pentericci, L., Vanzella, E., Castellano, M., et al. 2018, Astronomy & Astrophysics, 619, A147, doi: 10.1051/0004-6361/201732465

Pettini, M., Shapley, A. E., Steidel, C. C., et al. 2001, , 554, 981, doi: 10.1086/321403

Planck Collaboration, Aghanim, N., Akrami, Y., et al. 2018, arXiv:1807.06209 [astro-ph]. https://arxiv.org/abs/1807.06209

Planck Collaboration, Aghanim, N., Akrami, Y., et al. 2020, , 641, A6, doi: 10.1051/0004-6361/201833910

Prevot, M. L., Lequeux, J., Maurice, E., Prevot, L., & Rocca-Volmerange, B. 1984, , 132, 389

Prieto-Lyon, G., Strait, V., Mason, C. A., et al. 2023a, , 672, A186, doi: 10.1051/0004-6361/202245532

Prieto-Lyon, G., Mason, C., Mascia, S., et al. 2023b, , 956, 136, doi: 10.3847/1538-4357/acf715

Qin, Y., Mesinger, A., Bosman, S. E. I., & Viel, M. 2021, , 506, 2390, doi: 10.1093/mnras/stab1833

Reddy, N. A., Steidel, C. C., Pettini, M., Bogosavljević, M., & Shapley, A. E. 2016, , 828, 108, doi: 10.3847/0004-637X/828/2/108

Richard, J., Claeyssens, A., Lagattuta, D., et al. 2021, , 646, A83, doi: 10.1051/0004-6361/202039462

Rigby, J., Perrin, M., McElwain, M., et al. 2022, arXiv e-prints, arXiv:2207.05632. https://arxiv.org/abs/2207.05632

Roberts-Borsani, G., Morishita, T., Treu, T., et al. 2022, , 938, L13, doi: 10.3847/2041-8213/ac8e6e

Roberts-Borsani, G., Bagley, M., Rojas-Ruiz, S., et al. 2024, arXiv e-prints, arXiv:2407.17551, doi: 10.48550/arXiv.2407.17551

Roberts-Borsani, G. W., Bouwens, R. J., Oesch, P. A., et al. 2016, , 823, 143, doi: 10.3847/0004-637X/823/2/143

Robertson, B. E., Ellis, R. S., Dunlop, J. S., McLure, R. J., & Stark, D. P. 2010, Nature, 468, 49, doi: 10.1038/nature09527

Rodrigo, C., & Solano, E. 2020, in XIV.0 Scientific Meeting (virtual) of the Spanish Astronomical Society, 182

Rogers, A. B., McLure, R. J., & Dunlop, J. S. 2013, , 429, 2456, doi: 10.1093/mnras/sts515

Roper, W. J., Lovell, C. C., Vijayan, A. P., et al. 2022, , 514, 1921, doi: 10.1093/mnras/stac1368

Roy, N., Henry, A., Treu, T., et al. 2023, arXiv e-prints, arXiv:2304.01437, doi: 10.48550/arXiv.2304.01437

Saldana-Lopez, A., Schaerer, D., Chisholm, J., et al. 2022, arXiv e-prints, arXiv:2211.01351. https://arxiv.org/abs/2211.01351

Sanders, R. L., Shapley, A. E., Jones, T., et al. 2021, , 914, 19, doi: 10.3847/1538-4357/abf4c1

Santini, P., Maiolino, R., Magnelli, B., et al. 2014, , 562, A30, doi: 10.1051/0004-6361/201322835

Santos, M. R. 2004, , 349, 1137, doi: 10.1111/j.1365-2966.2004.07594.x

Saxena, A., Robertson, B. E., Bunker, A. J., et al. 2023, arXiv e-prints, arXiv:2302.12805, doi: 10.48550/arXiv.2302.12805

Saxena, A., Bunker, A. J., Jones, G. C., et al. 2024, , 684, A84, doi: 10.1051/0004-6361/202347132

Schaerer, D., & de Barros, S. 2009, , 502, 423, doi: 10.1051/0004-6361/200911781

Schenker, M. A., Ellis, R. S., Konidaris, N. P., & Stark, D. P. 2014, , 795, 20, doi: 10.1088/0004-637X/795/1/20

Shapley, A. E., Steidel, C. C., Pettini, M., & Adelberger, K. L. 2003, , 588, 65, doi: 10.1086/373922

Sharma, M., Theuns, T., Frenk, C., et al. 2017, , 468, 2176, doi: 10.1093/mnras/stx578

Shibuya, T., Ouchi, M., & Harikane, Y. 2015, , 219, 15, doi: 10.1088/0067-0049/219/2/15

Shibuya, T., Ouchi, M., Nakajima, K., et al. 2014, , 788, 74, doi: 10.1088/0004-637X/788/1/74

Shim, H., Chary, R.-R., Dickinson, M., et al. 2011, , 738, 69, doi: 10.1088/0004-637X/738/1/69

Shivaei, I., Reddy, N. A., Siana, B., et al. 2018, , 855, 42, doi: 10.3847/1538-4357/aaad62

Simmonds, C., Tacchella, S., Hainline, K., et al. 2024a, , 527, 6139, doi: 10.1093/mnras/stad3605

—. 2024b, arXiv e-prints, arXiv:2409.01286, doi: 10.48550/arXiv.2409.01286

Skelton, R. E., Whitaker, K. E., Momcheva, I. G., et al. 2014, , 214, 24, doi: 10.1088/0067-0049/214/2/24

Smit, R., Bouwens, R. J., Franx, M., et al. 2015, , 801, 122, doi: 10.1088/0004-637X/801/2/122

Stanway, E. R., Eldridge, J. J., & Becker, G. D. 2016, , 456, 485, doi: 10.1093/mnras/stv2661

Stark, D. P. 2016, , 54, 761, doi: 10.1146/annurev-astro-081915-023417

Stark, D. P., Ellis, R. S., Chiu, K., Ouchi, M., & Bunker, A. 2010, , 408, 1628, doi: 10.1111/j.1365-2966.2010.17227.x

Stark, D. P., Ellis, R. S., & Ouchi, M. 2011, , 728, L2, doi: 10.1088/2041-8205/728/1/L2

Stark, D. P., Schenker, M. A., Ellis, R., et al. 2013, , 763, 129, doi: 10.1088/0004-637X/763/2/129

Stark, D. P., Walth, G., Charlot, S., et al. 2015, , 454, 1393, doi: 10.1093/mnras/stv1907

Stark, D. P., Ellis, R. S., Charlot, S., et al. 2017, , 464, 469, doi: 10.1093/mnras/stw2233

Stefanon, M., Bouwens, R. J., Illingworth, G. D., et al. 2022, , 935, 94, doi: 10.3847/1538-4357/ac7e44

Steidel, C. C., Bogosavljevic, M., Shapley, A. E., et al. 2018, , 869, 123, doi: 10.3847/1538-4357/aaed28

Steidel, C. C., Rudie, G. C., Strom, A. L., et al. 2014, , 795, 165, doi: 10.1088/0004-637X/795/2/165

Steinhardt, C. L., Jauzac, M., Acebron, A., et al. 2020, , 247, 64, doi: 10.3847/1538-4365/ab75ed

Strait, V., Bradač, M., Coe, D., et al. 2021, , 910, 135, doi: 10.3847/1538-4357/abe533

Sun, F., Egami, E., Pirzkal, N., et al. 2022, arXiv e-prints, arXiv:2209.03374. https://arxiv.org/abs/2209.03374

Tacchella, S., Eisenstein, D. J., Hainline, K., et al. 2023, , 952, 74, doi: 10.3847/1538-4357/acdbc6

Tang, M., Stark, D. P., Chevallard, J., & Charlot, S. 2019, , 489, 2572, doi: 10.1093/mnras/stz2236

Tang, M., Stark, D. P., Chevallard, J., et al. 2021, , 503, 4105, doi: 10.1093/mnras/stab705

Tang, M., Stark, D. P., Ellis, R. S., et al. 2024c, , 972, 56, doi: 10.3847/1538-4357/ad5ae0

Tang, M., Stark, D. P., Topping, M. W., Mason, C., & Ellis, R. S. 2024b, arXiv e-prints, arXiv:2408.01507, doi: 10.48550/arXiv.2408.01507

Tang, M., Stark, D. P., Chen, Z., et al. 2023, arXiv e-prints, arXiv:2301.07072, doi: 10.48550/arXiv.2301.07072

Tang, M., Stark, D. P., Ellis, R. S., et al. 2024a, arXiv e-prints, arXiv:2402.06070, doi: 10.48550/arXiv.2402.06070

Topping, M. W., Stark, D. P., Endsley, R., et al. 2022, arXiv e-prints, arXiv:2208.01610. https://arxiv.org/abs/2208.01610

Trebitsch, M., Blaizot, J., Rosdahl, J., Devriendt, J., & Slyz, A. 2017, , doi: 10.1093/mnras/stx1060

Treu, T., Trenti, M., Stiavelli, M., Auger, M. W., & Bradley, L. D. 2012, , 747, 27, doi: 10.1088/0004-637X/747/1/27

Treu, T., Roberts-Borsani, G., Bradac, M., et al. 2022, , 935, 110, doi: 10.3847/1538-4357/ac8158

Umeda, H., Ouchi, M., Nakajima, K., et al. 2024, , 971, 124, doi: 10.3847/1538-4357/ad554e

Valentino, F., Brammer, G., Gould, K. M. L., et al. 2023, , 947, 20, doi: 10.3847/1538-4357/acbefa

Vanzella, E., Nonino, M., Cupani, G., et al. 2018a, , 476, L15, doi: 10.1093/mnrasl/sly023

—. 2018b, , 476, L15, doi: 10.1093/mnrasl/sly023

Vanzella, E., Castellano, M., Bergamini, P., et al. 2022, arXiv e-prints, arXiv:2208.00520. https://arxiv.org/abs/2208.00520

Vanzella, E., Claeyssens, A., Welch, B., et al. 2023, , 945, 53, doi: 10.3847/1538-4357/acb59a

Verhamme, A., Orlitová, I., Schaerer, D., & Hayes, M. 2015, Astronomy & Astrophysics, 578, A7, doi: 10.1051/0004-6361/201423978

Verhamme, A., Schaerer, D., Atek, H., & Tapken, C. 2008, Astronomy and Astrophysics, 491, 89, doi: 10.1051/0004-6361:200809648

Verhamme, A., Schaerer, D., & Maselli, A. 2006, Astronomy & Astrophysics, 460, 397, doi: 10.1051/0004-6361:20065554

Verhamme, A., Garel, T., Ventou, E., et al. 2018, , 478, L60, doi: 10.1093/mnrasl/sly058

Wang, F., Davies, F. B., Yang, J., et al. 2020, arXiv:2004.10877 [astro-ph]. https://arxiv.org/abs/2004.10877

Whitler, L. R., Mason, C. A., Ren, K., et al. 2020, , 495, 3602, doi: 10.1093/mnras/staa1178

Williams, H., Kelly, P. L., Chen, W., et al. 2022, arXiv e-prints, arXiv:2210.15699. https://arxiv.org/abs/2210.15699

Willott, C. J., Carilli, C. L., Wagg, J., & Wang, R. 2015, , 807, 180, doi: 10.1088/0004-637X/807/2/180

Witstok, J., Smit, R., Saxena, A., et al. 2024, , 682, A40, doi: 10.1051/0004-6361/202347176

Witstok, J., Jakobsen, P., Maiolino, R., et al. 2024b, arXiv e-prints, arXiv:2408.16608, doi: 10.48550/arXiv.2408.16608

Witstok, J., Maiolino, R., Smit, R., et al. 2024c, , doi: 10.1093/mnras/stae2535

Xu, X., Heckman, T., Henry, A., et al. 2022, , 933, 222, doi: 10.3847/1538-4357/ac6d56

Yang, H., Malhotra, S., Rhoads, J. E., & Wang, J. 2017a, , 847, 38, doi: 10.3847/1538-4357/aa8809

Yang, H., Malhotra, S., Gronke, M., et al. 2017b, , 844, 171, doi: 10.3847/1538-4357/aa7d4d

Yang, L., Birrer, S., & Treu, T. 2020, arXiv:2001.07719 [astro-ph]. https://arxiv.org/abs/2001.07719

Yuan, Y., Martin-Alvarez, S., Haehnelt, M. G., et al. 2024, arXiv e-prints, arXiv:2412.07970, doi: 10.48550/arXiv.2412.07970

Zackrisson, E., Inoue, A. K., & Jensen, H. 2013, , 777, 39, doi: 10.1088/0004-637X/777/1/39

Zackrisson, E., Binggeli, C., Finlator, K., et al. 2017, , 836, 78, doi: 10.3847/1538-4357/836/1/78

Zitrin, A., Labbé, I., Belli, S., et al. 2015, , 810, L12, doi: 10.1088/2041-8205/810/1/L12